Ultra-Low Frequency Waves in the Magnetosphere

Lasse Boy Novock Clausen

Radio and Space Plasma Physics Group
Department of Physics and Astronomy
University of Leicester

A thesis submitted to the University of Leicester
for the degree of Doctor of Philosophy

July 2009

I, Lasse Boy Novock Clausen, confirm that the work presented in this thesis is my own. Where information has been derived from other sources, I confirm that this has been indicated in the thesis.

Abstract

Ultra-Low Frequency Waves in the Magnetosphere by Lasse Boy Novock Clausen

Ultra-low frequency waves, i.e. pulsations between 0.1 and 1,000 mHz, are an inherent feature of space plasmas. These plasmas are largely collisionless and hence waves play an important role as an agent to transfer energy, mass and momentum. This work explores some of the wave's features in the Earth's magnetosphere using several different measurement techniques located in different regions.

The first of the three case studies presented describes results from an experiment involving an ionospheric heating facility located on Svalbard. The SPace Exploration by Active Radar (SPEAR) facility periodically changed the ionospheric conductivities, superimposing a AC component on a background DC current. Thus the heated patch acted as a giant virtual antenna, emitting Alfvén waves which were detected by ground-based magnetometers in the vicinity of the heater.

The following two case studies investigate naturally occurring waves, using both space- and ground-based instruments. In both cases waves generated at the bow shock penetrated into the magnetospheric cavity where they interacted with the local plasma and magnetic field. Whereas in the first case the propagation path of one individual wave packet is analysed, the last data chapter discusses the generation of Alfvénic continuum by upstream generated waves.

Acknowledgements

Many people have contributed to the successful completion of this thesis. I would like to thank you all. You know who you are.

Contents

1 Introduction **1**

1.1 Space Plasma Physics 2

1.1.1 The Sun 3

1.1.2 The Solar Wind 4

1.1.3 The Bow Shock 7

1.1.4 The Earth's Magnetosphere 10

1.1.5 The Earth's Ionosphere 11

1.1.6 Ionospheric Convection 15

1.2 Magnetohydrodynamics and ULF waves 17

1.2.1 Transverse Mode 21

1.2.2 Longitudinal Waves 24

1.2.3 Mode Coupling 25

1.2.4 MHD waves in a dipole magnetic field 28

1.2.5 Field Line Resonances in the Magnetosphere 31

1.2.6 Upstream Generated Waves 38

1.2.7 Artificial Waves 43

2 Instrumentation and Data Analysis 47

2.1 Instrumentation 48

2.1.1 Fluxgate Magnetometers 48

2.1.2 SPEAR 49

2.1.3 The Svalbard Ionosonde 51

2.1.4 The Barentsburg Doppler Sounder 51

2.1.5 Cluster 52

2.1.6 Ground-Based Magnetometers 55

2.1.7 ACE 59

2.1.8 Geotail 61

2.1.9 DMSP 61

2.2 Data Analysis Techniques 62

2.2.1 The Cross-phase Technique 62

2.2.2 Mean-Field Aligned Coordinate System 64

3 Artificial ULF Waves 66

3.1 Introduction 67

3.2 Observations and Discussion 68

3.2.1 Ionospheric Conditions 70

3.2.2 Ground-Based Observations 74

3.2.3 Solar Wind Conditions 81

3.3 Conclusions 85

4 Large-Scale Pc4 86

4.1 Introduction 87

4.2 Observations . . . 88
4.2.1 Ground-Based Magnetometers . . . 88
4.2.2 Space Based Observations . . . 93
4.3 Discussion . . . 100
4.3.1 Wave Origin and Motion . . . 100
4.3.2 Harmonic Structure . . . 110
4.4 Conclusions . . . 122

5 Upstream Waves 124

5.1 Introduction . . . 125
5.2 Observations . . . 126
5.2.1 Space-Based Observations . . . 126
5.2.2 Ground Magnetometer Observations . . . 139
5.3 Discussion . . . 142
5.3.1 Field-Aligned Component . . . 142
5.3.2 Azimuthal Component . . . 146
5.3.3 Upstream Waves at Geotail . . . 151
5.4 Conclusions . . . 155

6 Summary and Conclusions 157

6.1 Summary I . . . 158
6.2 Outlook I . . . 159
6.3 Summary II . . . 159
6.4 Outlook II . . . 161
6.5 Concluding Remarks . . . 161

List of Tables

1.1 Classification of geomagnetic micropulsations 32

4.1 Phase in degree for different stations along longitudinal profiles 92

5.1 Locations, L-values and eigenfrequencies of some magnetometers . . . 150

List of Figures

1.1 Plasma parameters in the Sun's atmosphere 4

1.2 Illustration of the "frozen-in" theorem 6

1.3 Two typical bow shock crossings 8

1.4 Schematic view of the Earth's magnetic field 10

1.5 Altitude of unit optical depth 12

1.6 Typical electron densities 13

1.7 Typical convection pattern 16

1.8 Orientation of perturbations associated with different wave modes . . 23

1.9 Dipolar coordinate system 28

1.10 Orientation of perturbation fields 32

1.11 FLR latitude profiles 33

1.12 Schematic of the driving process of FLRs 35

1.13 Spectrograms of satellite magnetic field data 37

1.14 Schematic of the foreshock region. 38

1.15 Schematic of the region upstream of the bow shock 40

1.16 Magnetic field of a VLF wave generated by a HF pulse 43

1.17 Overview of heating results 45

2.1 Schematic of a fluxgate magnetometer. 49

2.2 Layout and orientation of SPEAR 50
2.3 Orbits of the Cluster spacecraft 53
2.4 IMAGE magnetometer stations 57
2.5 CARISMA magnetometer stations 57
2.6 INTERMAGNET magnetometer stations 58
2.7 MACCS magnetometer stations 59
2.8 SAMNET magnetometer stations 60
2.9 Schematic illustrating the cross-phase technique 63

3.1 Overview of magnetometers and DMSP footprints 68
3.2 Electron spectra measured by DMSP 13 and 15 69
3.3 Ionograms measured near SPEAR 72
3.4 Doppler shift and amplitude measured in Barentsburg 73
3.5 Overview of magnetometer data 75
3.6 Dynamic spectra of ground-based magnetometer data 78
3.7 Cross-phase between a sine and ground-based magnetometer data . . 79
3.8 Time series of the three GSM components of the IMF 82
3.9 Time series of Fourier power in different frequency bands 84

4.1 Filtered ground-based magnetometer data 89
4.2 Filtered ground-based magnetometer data from Alaska and Japan . . 93
4.3 Orbit overview for Cluster 3 and 4 94
4.4 Magnetic, electric field and resulting Poynting flux measured by s/c 3 96
4.5 Summary of field data from Cluster 4, same format as Fig. 4.4. 98
4.6 Equatorial crossing points 102
4.7 An illustration of "Tamao's path" 103

4.8 Standard deviation between observed and modelled lags 105
4.9 Observed and calculated lag times 108
4.10 Observed lags plotted against modelled lags. 109
4.11 Magnetic field measured by Geotail 111
4.12 Cross-phase spectra of stations belonging to the SAMNET array . . . 112
4.13 Fundamental frequency over L-value 113
4.14 Fundamental eigenfrequency against spectral power at 17.2 mHz . . . 116
4.15 Numerical solution of the wave equation on a dipolar field line 119
4.16 Node structure of a 17.2 mHz wave at L=5 R_e 121

5.1 Magnetic field measured by Geotail 127
5.2 Dynamic spectra of the Geotail magnetic field data 128
5.3 Cluster orbit overview 130
5.4 Spectra of electric and magnetic field data from s/c 1 132
5.5 Spectra of electric and magnetic field data from s/c 2 133
5.6 Spectra of electric and magnetic field data from s/c 3 135
5.7 Spectra of electric and magnetic field data from s/c 4 136
5.8 Electron spectra measured by PEACE onboard s/c 1 137
5.9 Cluster footprint overview 140
5.10 Dynamic spectra of some ground-based magnetometer stations 141
5.11 Wave power in the compressional magnetic component 144
5.12 Electron densities determined by WHISPER 148
5.13 Geometry for different IMF orientations 152
5.14 θ_{nB} and θ_{xB} over time 153

1 Introduction

> The general problem of Alfvén wave propagation in a dipole field has perplexed numerous authors and will continue to do so, since it has never been adequately solved or physically interpreted.
>
> *Henry R. Radoski (1967)*

1.1 Space Plasma Physics

Laboratory experiments cannot reproduce conditions which are found in the near-Earth environment. It hence offers a formidable opportunity to study plasma physics. For example, an "ultra high vacuum" chamber on Earth at 10^{-7} Pa still contains about 6 orders of magnitude more particles per cm^3 then are usually found at the geostationary orbit at a geocentric distance of about 6 Earth radii (R_e).

Apart from being of purely academic interest, the processes that go on in the Earth's space environment have an impact on our every day lives, nowadays more than ever. Before the age of satellites, the only manifestation of magnetospheric activity that affected human lives were the grand displays of aurora, flickering lights in the sky which are, as we now know, caused by charged particles precipitating into the upper atmosphere.

Space plasma physics has a much more direct impact on every day life in this day and age, even if unappreciated by most. Much of the global communication is achieved with the help of satellites, i.e. sensitive electronic equipment immersed in the plasma that surrounds the Earth. In order to protect these means of communication, we have to understand the processes that go on the surrounding medium.

Some parts of the universe consist of very dense plasma indeed, however most parts are filled by plasmas with very low densities. As a direct result of the low densities, collision frequencies between the constituents are also very low. As it turns out, electromagnetic waves are, in these plasmas, the prime agent that transports particles, momentum and energy through the system.

Each of Chas. 3 to 5 contains detailed analysis of wave events in the terrestrial magnetosphere, however in this chapter we will start off by laying some ground work that is needed in order to understand the results presented later.

1.1.1 The Sun

Roughly 4.5 billion years ago, the Sun was formed. At its core, temperatures are assumed to be as high as 1.5×10^7 K (e.g. Brekke, 1997). At such high temperatures protons will be fused to helium nuclei in a thermonuclear chain reaction.

Ultimately, this exothermic reaction is the source of energy for any process inside our solar system. The heat produced inside the Sun is transported outwards from the core first by radiation and then by convection. The top of the convection zone at a radius of about 7×10^8 m is often referred to as the Sun's surface (Lean, 1991). Above the convection zone the temperature of the Sun's atmosphere varies dramatically and three regions can be identified.

Layered immediately above the convection zone, stretching to an altitude of about 500 km, is the photosphere, followed by the chromosphere (500 - 2000 km) and the corona at altitudes larger than 2000 km. Temperature and mass density in the three regions are shown in Fig. 1.1.

Electromagnetic emissions of the Sun have, conveniently, a maximum in the visible wavelength range (400 nm to 780 nm). Its spectrum can be approximated by that of a black body with a temperature around 6000 K, indicating that most of the Sun's emission observed on Earth originates from the photosphere.

Spectral analysis of the radiation from the Sun shows that whereas the visible part of the spectrum is rather constant with time, emissions at smaller wavelengths in the X-ray, extreme ultra-violet (EUV) and ultra-violet (UV) regime as well as the radio emissions at wavelength greater, say, 10,000 nm are highly variable (Lean, 1991). The intensity of such emissions undergoes a roughly 11-year cycle, from solar maximum through minimum back to maximum (Hathaway et al., 1994, and references therein).

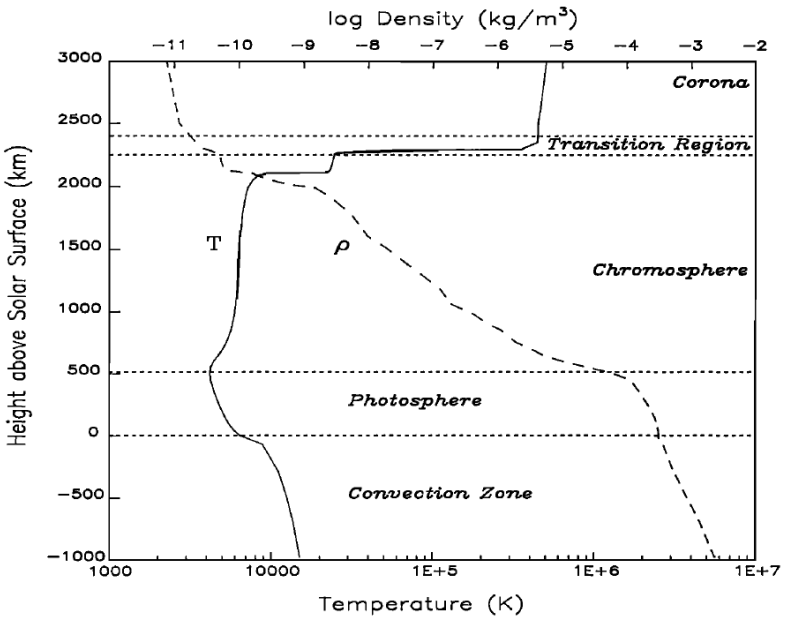

Figure 1.1: Temperature (T) and mass density (ρ) as functions of height in the Sun's magnetically unperturbed, or "quiet," atmosphere. The regions of the solar atmosphere identified in this figure correspond to inflections in the temperature profile (from Lean, 1991).

1.1.2 The Solar Wind

The solar wind is a stream of charged particles which is ejected from the upper atmosphere of the Sun. This wind is always blowing. It is not a steady wind but rather gusty with strong variations in speed and density as it arrives at the Earth, some 150 million kilometres from the Sun. Its average speed at a distance corresponding to the Earth's orbit is roughly 400 km/s, but values range from around 200 to well over 800 km/s.

The composition of the solar wind is 95% protons (H^+), 4% alpha particles (He^{2+}) and 1% minor ions, of which carbon, nitrogen, oxygen, neon, magnesium, silicon and iron are the most abundant (Ogilvie and Coplan, 1995). The source of the solar wind is the Sun's hot corona and thus the corona's composition is identical to that of the

solar wind. The temperature of the corona is high enough (10^6 K, see Fig. 1.1) for the coronal particles to escape the Sun's gravity. Although it is understood why this happens the details about how and where the coronal gases are heated to these high temperatures are not yet understood. It is currently believed that waves play a crucial role in the heating process (Del Zanna and Velli, 2002).

The solar magnetic fields embedded in the plasma are carried into space by the solar wind to form the interplanetary magnetic field (IMF) (Parker, 1958). This can be explained by the so-called "frozen-in" condition that follows from the generalised Ohm's law

$$\vec{E} + \vec{v} \times \vec{B} = \frac{\vec{j}}{\sigma} \tag{1.1}$$

which connects the electric field $\vec{E}$, the bulk flow velocity $\vec{v}$ and the magnetic field $\vec{B}$ with the current density $\vec{j}$ and conductivity σ.

The free mean path of the solar wind plasma is of the order of the distance between the Sun and the Earth, hence the solar wind plasma can be assumed collisionless. As it is also fully ionised, the conductivity σ tends to infinity, giving the "frozen-in" condition

$$\vec{E} + \vec{v} \times \vec{B} = 0. \tag{1.2}$$

The reason why this is called the "frozen-in" condition becomes apparent when (1.2) is inserted into Faraday's law and the following is obtained:

$$\frac{\partial \vec{B}}{\partial t} = \nabla \times (\vec{v} \times \vec{B}). \tag{1.3}$$

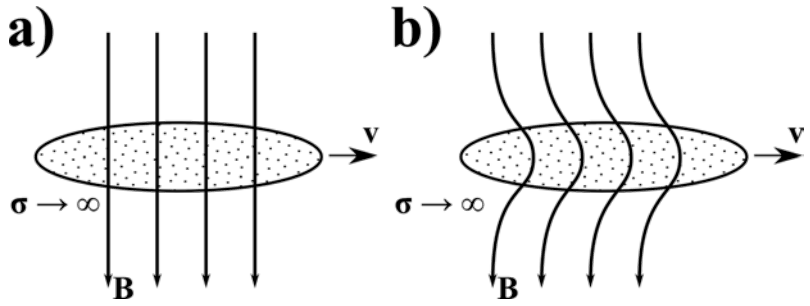

Figure 1.2: Illustration of the "frozen-in" theorem. **a)** A magnetic field penetrates a highly conducting plasma. **b)** As the plasma moves, the magnetic field is "frozen-in" and follows the motion of the plasma.

The change in magnetic flux ϕ through a surface S moving with velocity $\vec{v}$ consists of one part due to the time variation of the magnetic field $\vec{B}$ and one part due to the motion of the surface across $\vec{B}$:

$$\frac{d\phi}{dt} = \iint_S \frac{\partial \vec{B}}{\partial t} \cdot d\vec{s} + \oint_L \vec{B} \cdot (\vec{v} \times d\vec{l}) \tag{1.4}$$

L denotes a loop around the surface S. Rearranging (1.4) and using Stoke's law one obtains

$$\frac{d\phi}{dt} = \iint_S \left[\frac{\partial \vec{B}}{\partial t} - \nabla \times (\vec{v} \times \vec{B}) \right] \cdot d\vec{s} \tag{1.5}$$

where the integrand is the result obtained from the "frozen-in" condition in (1.3) and is hence zero. This means that the magnetic flux ϕ in plasmas of very high conductivity is constant. A magnetic field penetrating a highly conducting plasma will follow the plasma's motion - it is "frozen-in". Fig. 1.2 illustrates this interpretation.

As predicted by the above considerations, the solar wind carries magnetic fields away from the Sun as it streams into the interplanetary space. In this way the IMF is formed.

1.1.3 The Bow Shock

The solar wind plasma streams off the Sun at supersonic speeds, the typical speed of sound v_s being about ten times smaller than the flow speed. As the magnetic field of the Earth forms an obstacle in the solar wind stream, a shock wave is formed upstream of the Earth (Tsurutani and Stone, 1985).

The angle θ_{nB} between the local normal of the shock surface $\vec{n}$ and the upstream magnetic field is the most crucial parameter in determining the shock's local characteristics (Greenstadt, 1991). As the shock surface can be approximated by a rotational parabola around the Sun-Earth line, the angle θ_{nB} changes locally across the bow shock surface (Peredo et al., 1995). At the subsolar point on the bow shock this angle is equal to the angle between the IMF and the Sun-Earth line which is called the cone angle θ_{xB} and defined as

$$\cos\theta_{xB} = |B_x|/B_{tot}. \tag{1.6}$$

Here B_{tot} is the IMF magnitude and B_x is the X component of the IMF in GSM coordinates.

Whenever $\theta_{nB} < 45°$, the shock is called quasi-parallel, whereas for $\theta_{nB} > 45°$ the shock is called quasi-perpendicular.

Fig. 1.3 shows two example shock crossings by one of the Cluster satellites (Sec. 2.1.5). The shock crossing is in both examples outbound, i.e. from the region of subsonic flow (downstream region, magnetosheath) into the region of supersonic flow (upstream region, solar wind). From top to bottom, the ion density, the magnetic field strength, the plasma bulk speed, the sonic Mach number and the differential electron flux observed by the Cluster satellite are shown.

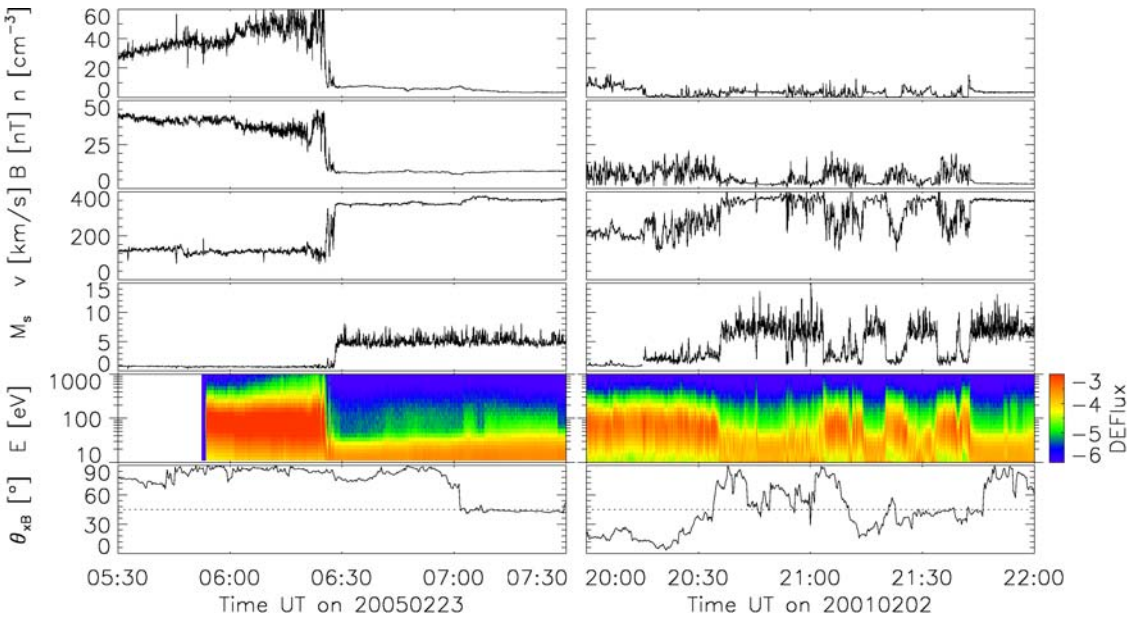

Figure 1.3: Two typical bow shock crossings. The left panels show the crossing of a quasi-perpendicular shock whereas the right panels show that of a quasi-parallel shock.

The sonic Mach number M_s is simply the ratio of the flow speed v to the speed of sound. For $M_s > 1$ the flow is supersonic, subsonic flow is characterised by $M_s < 1$. In Fig. 1.3 the speed of sound v_s was estimated from the ideal gas approximation, i.e.

$$M_s = \frac{v}{v_s} = \frac{v}{\sqrt{\gamma p/\rho}} = \frac{v}{\sqrt{\gamma k_B (T_i + T_e)/(m_i + m_e)}} \tag{1.7}$$

where $\gamma = 5/3$ is the ratio of the specific heats, p is the pressure, ρ is the mass density, k_B is the Boltzmann constant, T is the temperature and m is the mass. In (1.7) the subscripts i and e refer to ions and electrons, respectively. Here, $T_i = T_e$ has been assumed.

The bottom panels show the cone angle determined from magnetic field measurements by the ACE satellite (Sec. 2.1.7). These have been lagged by the propagation time of the solar wind from the satellite's position to the bow shock.

As can be seen from the cone angle time series in the bottom panels, the crossing shown in the left panels occurred during times when the shock was quasi-perpendicular, whereas on the right plasma parameters for a quasi-parallel shock crossing are shown. The crossing shown on the right was discussed in detail by Lucek et al. (2002).

Generally, quasi-perpendicular shocks are characterised by a sharp transition, as can be seen just before 0630 UT in the left panels of Fig. 1.3. Before the shock crossing the magnetic magnitude and ion densities were high and the flow speed v was low. This resulted in Mach numbers just below 1, i.e. subsonic flow. The differential energy flux shows an electron population with energies around 100 eV. The plasma parameters changed sharply across the quasi-perpendicular shock to values typical for the solar wind: low magnetic magnitude and density, high flow speed and an electron population centred at lower energies.

The picture is much more complex in the case of a quasi-parallel shock as shown in the right panels. The essential ingredient resulting in the observed complexity are particles reflected at the bow shock. As the bow shock is generally associated with an increase in magnetic magnitude, it acts as a magnetic mirror. During quasi-parallel conditions the reflected particles can move large distances upstream into the solar wind as they gyrate around the IMF field lines. As reflected ions move along the IMF against the solar wind flow, they can resonantly interact with naturally occurring waves into the solar wind, creating large-amplitude ULF waves. This process is described in more detail in Sec. 1.2.6.

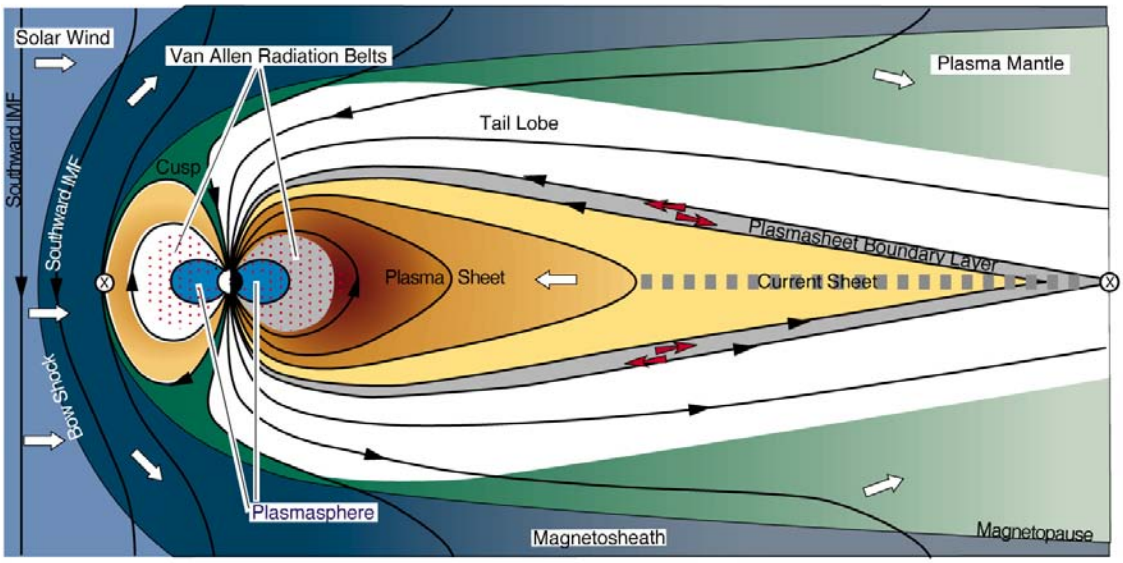

Figure 1.4: Schematic view of the Earth's magnetosphere (adapted from T. W. Hill).

1.1.4 The Earth's Magnetosphere

It has been known for several hundred years that the Earth possesses a magnetic field. However, the start of modern science of geomagnetism can probably be dated back to William Gilbert who in the year 1600 published the book "De Magnete". This book is a comprehensive review of what was known about the nature of magnetism, and Gilbert added much knowledge through his own experiments. Also in this book he stated that "Magnus magnetis ipse est globus terrestris" (The Earth itself is a great magnet).

Since satellites opened the opportunity to sample plasma and field parameters in the Earth's space environment, different regions within the cavity formed by the Earth's magnetic field in the solar wind were observed as sketched in Fig. 1.4.

As described in the previous section, the supersonic solar wind is slowed at the bow shock. Behind the bow shock follows a region called magnetosheath which is characterised by turbulent conditions (Yordanova et al., 2008) and the presence of

a variety of wave modes (Hubert, 1994). In this region the shocked solar wind is deflected around the magnetic field of the Earth.

The interface between the magnetosheath and the Earth's magnetic field is called the magnetopause. To a first approximation, it is located at the position where the solar wind dynamic pressure $p_{dyn} = \rho v^2$ matches the magnetic pressure $p_m = B^2/2\mu_0$ of the terrestrial field. It is at this interface that magnetic reconnection acts as an agent to inject energy into the magnetospheric system (Chisham et al., 2008).

Anti-parallel magnetic field lines can, when meeting, merge together and produce two topologically different field lines. This process is called magnetic reconnection. At the subsolar point the terrestrial magnetic field is orientated northwards. During periods of southward IMF, these two magnetic fields can merge by magnetic reconnection. Formerly closed magnetic field lines of the Earth are opened and convected with the solar wind into the magnetic tail.

The accumulation of flux in the tail brings the field lines inside the tail closer together until they are close enough to reconnect themselves. The newly reconnected field lines convect around the Earth's flanks back to the dayside such that the cycle can be repeated. This is called the Dungey cycle (Dungey, 1961).

1.1.5 The Earth's Ionosphere

On a clear day the spectrum of the Sun's electromagnetic radiation between 300 and 1000 nm, near the peak of the black body curve approximating the radiation curve of the Sun, reaches the Earth's surface only moderately attenuated by the atmosphere. However, atomic oxygen, molecular oxygen, molecular nitrogen and ozone (O, O^2, N^2, O^3) absorb all of the energy from the Sun at wavelengths less than 300 nm. The altitudes up to which radiation of a certain wavelength penetrates

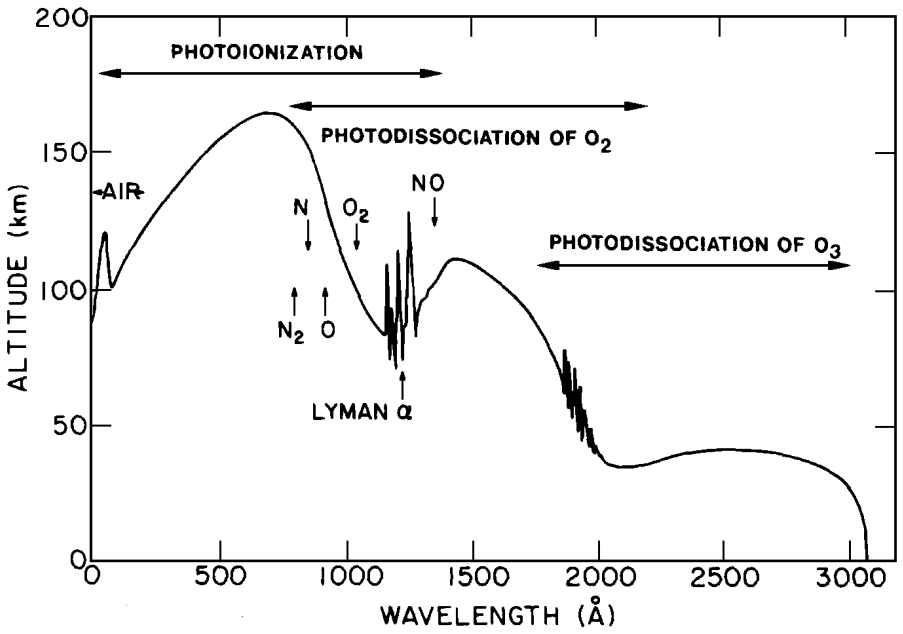

Figure 1.5: The curve shows the altitude of unit optical depth for wavelengths below 300 nm (from Giraud and Petit, 1978).

the Earth's atmosphere is shown in Fig. 1.5.

As these molecules absorb solar radiation they are ionised. This is the principal source of free charged particles in the layer above the Earth's surface called the ionosphere. As more and more of the solar radiation is absorbed, an electron density profile is formed which peaks at a certain altitude.

Typical electron density profiles for mid-latitudes during day and night as well as solar minimum and maximum are shown in Fig. 1.6. These densities have been calculated with actual solar activity input by the IRI-2007 model (Bilitza and Reinisch, 2008, and references therein). As the free charges in the ionosphere are mainly produced by photoionisation due to radiation from the Sun in the EUV and UV range, a significant impact of the solar cycle on the measured densities is observed.

As the composition of molecules is changing in the upper atmosphere, three regions in the electron density profile are formed. These are for historical reasons called the

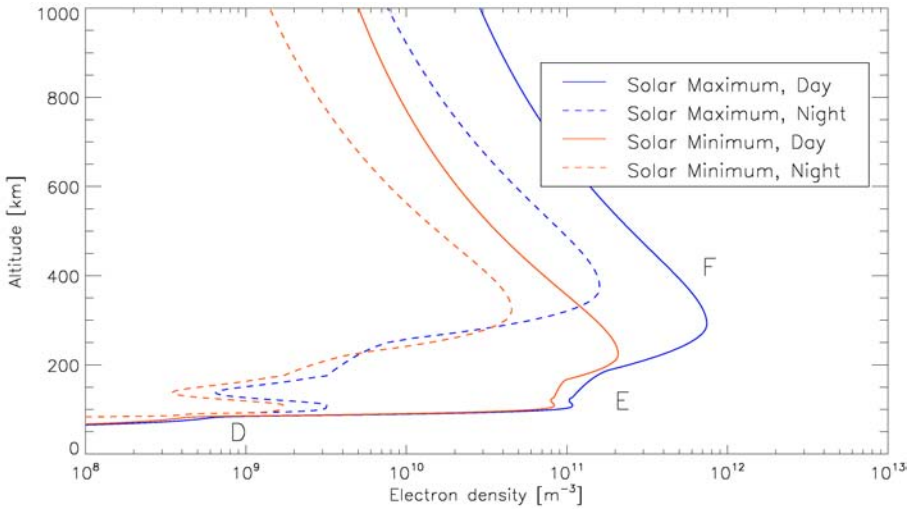

Figure 1.6: Model predictions of electron densities during daytime and nighttime, as well as solar minimum and maximum.

D-, E- and F-regions (see Fig. 1.6). Atomic oxygen O^+ dominates the F-region at altitudes greater than 200 km, whereas NO^+ and O_2^+ are more abundant in the E-region between 90 and 200 km. The D-region between 60 and 90 km altitude is characterised by a complex photochemistry and collisions are dominant.

As can be seen in Fig. 1.6, the E-region disappears during nighttime. As the solar radiation does not reach the nightside ionosphere, the change in electron density is governed by recombination processes. Brekke (1997) gives the recombination time, i.e. the time it takes for the density to decrease to $1/e$ of its initial value, in the E-region as

$$\tau = \frac{1}{2\alpha_{\text{eff}} n_e} = \frac{1}{2(\frac{1}{4}\alpha_1 + \frac{3}{4}\alpha_2) n_e}. \tag{1.8}$$

Here α_{eff} is the effective recombination coefficient which depends on the reaction

rates α_1 and α_2 of the following two processes:

$$NO^+ + e \xrightarrow{\alpha_1} N + O \tag{1.9}$$

$$O_2^+ + e \xrightarrow{\alpha_2} O + O. \tag{1.10}$$

The reaction rates α_1 and α_2 are $\alpha_1 = 2.1 \cdot 10^{-13}(T_e/300)^{-.85}$ m^3s^{-1} and $\alpha_2 = 1.9 \cdot 10^{-13}(T_e/300)^{-.5}$ m^3s^{-1}, respectively (Brekke, 1997).

The IRI-2007 model gives the electron temperature T_e in the E-region at around 500 K. Hence even at low electron densities of 10^{10} m^{-3} the recombination time is below ten minutes, allowing the E-region electron density to quickly recombine away during nighttime.

The shape of the F-region electron density peak remains essentially unchanged during the absence of solar radiation at night. In the F-region chemistry is dominated by the presence of O^+ which does not react with free electrons to create atomic oxygen. Instead, an ion-molecule reaction with a relatively long time constant has to take place before the products of that reaction can recombine with free electrons. Hence the loss process of charged particles in this region is governed by the following two ion-molecule reactions (Schunk and Nagy, 2000):

$$O^+ + N_2 \xrightarrow{k_1} NO^+ + N \tag{1.11}$$

$$O^+ + O_2 \xrightarrow{k_2} O_2^+ + O \tag{1.12}$$

The continuity equation for the O^+ density $n(O^+)$ is then

$$\frac{\partial n(O^+)}{\partial t} = -k_\beta n(O^+) \tag{1.13}$$

The reaction rate of this process k_β dependent on the densities of N_2 and O_2, the reaction rates k_1 and k_2 and is given by (Schunk and Nagy, 2000)

$$k_\beta = 1.2 \times 10^{-12} n(N_2) + 2.1 \times 10^{-11} n(O_2) \tag{1.14}$$

The MSISE-90 model (Hedin, 1991) gives the densities $n(N_2) = 1.9 \times 10^1 4\ \mathrm{m}^{-3}$ and $n(O_2) = 8.9 \times 10^1 2\ \mathrm{m}^{-3}$ such that the time constant of the exponential decay of the O^+ concentration is found to be around one hour, i.e. considerably longer than that estimated for the E-region. Hence a background ionisation exists even during night at higher altitudes.

1.1.6 Ionospheric Convection

If no electric field is present, the Lorentz force $\vec{F}_L = q\vec{v} \times \vec{B}$ causes charged particles with a velocity $\vec{v}$ and charge q to gyrate around magnetic field lines. The frequency f of this motion is given by

$$f = \frac{qB}{m}, \tag{1.15}$$

where m is the particle's mass.

Any force $\vec{F}$ capable of accelerating and decelerating charged particles superimposes an additional drift perpendicular to both the magnetic field and the force. The drift velocity $\vec{u}_d$ is then given by

$$\vec{u}_d = \frac{\vec{F} \times \vec{B}}{qB^2}. \tag{1.16}$$

Hence the force $q\vec{E}$ associated with an electric field $\vec{E}$ will cause charged particles

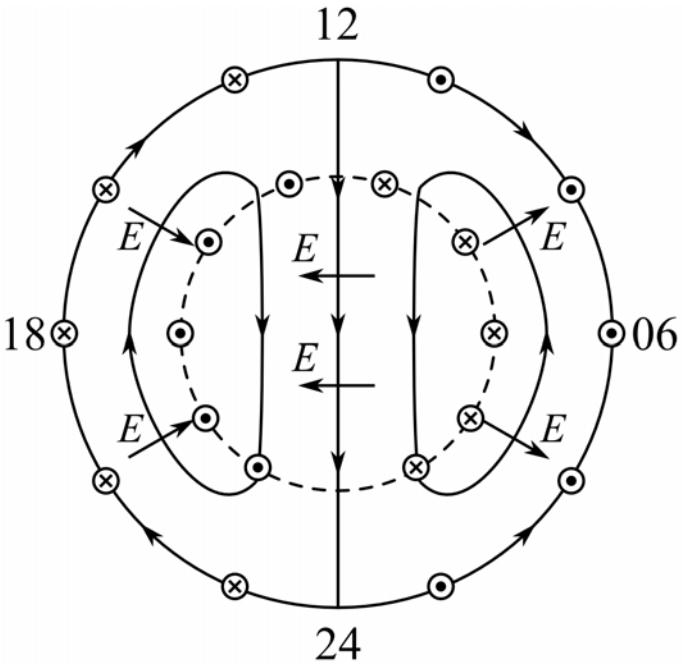

Figure 1.7: Typical twin-cell convection pattern during southward IMF in the northern hemisphere. Solid arrowed lines are the plasma streamlines, the short arrows give the direction of the electric field and the dashed line is the open-closed field line boundary. Field-aligned currents are indicated as dots (adapted from Cowley, 2000).

to drift while still gyrating around the magnetic field. This E-cross-B drift does not introduce any currents in the plasma as it is independent of both q and m.

As discussed before, Dungey (1961) proposed an open magnetosphere where, through reconnection, magnetic field lines are opened on the dayside and swept with the solar wind flow into the tail. There they reconnect and convect toward the dayside to complete the cycle.

The solar wind caries an electric field of size $\vec{v}_{SW} \times \vec{B}_{IMF}$. The conductivity along magnetic field lines is high such that they can be assumed to be equipotentials of this electric field. Hence the solar wind flow introduces a large scale electric field into the upper ionosphere.

With decreasing altitude in the ionosphere the neutral density increases, which

also increases the frequency ν of collisions of charged particles with neutrals. It can be shown that if the gyrofrequency f is much higher than ν, which is the case in the upper ionosphere above 150 km, particles will E-cross-B drift. This E-cross-B drift causes a large scale ionospheric twin cell convection as shown in Fig. 1.7.

Below 150 km, however, the ion-neutral collision frequency is of the order of their gyrofrequency which causes the E-cross-B drift of ions to break down. Instead, the ions are accelerated in the direction of the electric field. Hence the large scale convection electric field gives rise to large scale current systems in the lower ionosphere (Cowley, 2000).

1.2 Magnetohydrodynamics and ULF waves

The magnetospheric cavity is filled with plasma, i.e. partly ionised gas, which is threaded by the magnetic field of the Earth.

To investigate the possibility of waves occurring in such a medium, an infinite homogeneous plasma in equilibrium (i.e. $\vec{v}_0 = 0$) with uniform mass density ρ_0 and pressure p_0 is considered. It is permeated by a uniform magnetic field $\vec{B}_0$. This situation is described by the following set of equations (compare Chapter 2.8 in Brekke, 1997):

- Continuity equation

$$\frac{\partial \rho}{\partial t} + \nabla \cdot (\rho \vec{v}) = 0 \tag{1.17}$$

- Equation of motion

$$\rho \left[\frac{\partial \vec{v}}{\partial t} + (\vec{v} \cdot \nabla)\vec{v} \right] = -\nabla p - \vec{B} \times \vec{j} \tag{1.18}$$

- Faraday's law

$$\frac{\partial \vec{B}}{\partial t} = -\nabla \times \vec{E} \tag{1.19}$$

- Ampère's law

$$\frac{1}{\mu_0}\nabla \times \vec{B} = \vec{j} \tag{1.20}$$

- "Frozen-in" condition

$$\vec{E} + \vec{v} \times \vec{B} = 0 \tag{1.21}$$

Note that the second term on the right hand side of Ampère's law $\epsilon_0 \partial \vec{E}/\partial t$ can be neglected in the magnetohydrodynamics (MHD) approximation. In this highly subrelativistic situation characteristic velocities U are much smaller than the speed of light c, hence

$$U = \frac{L}{T} \ll c \tag{1.22}$$

where L denotes characteristic length scales and T characteristic time scales.

Replacing time and space derivatives by T^{-1} and L^{-1} and physical quantities Q by their magnitude $[Q]$, one finds resulting from Faraday's law (1.19) that

$$\frac{[\vec{E}]}{L} \approx \frac{[\vec{B}]}{T}. \tag{1.23}$$

The displacement current term $\epsilon_0 \partial \vec{E}/\partial t$ is then seen to be of order $U^2/c^2 \ll 1$

relative to $1/\mu_0 \nabla \times B$:

$$\frac{\left|\epsilon_0 \partial \vec{E}/\partial t\right|}{|1/\mu_0 \nabla \times B|} \approx \frac{\epsilon_0 [\vec{E}]/T}{[\vec{B}]/\mu_0 L} = \mu_0 \epsilon_0 \frac{L^2 [\vec{E}]/L}{T^2 [\vec{B}]/T} \approx \frac{1}{c^2} U^2. \tag{1.24}$$

Therefore the displacement current in Ampère's law can be neglected.

(1.17), (1.18), (1.19), (1.20) and (1.21) can be linearised by introducing small perturbations like

$$\vec{v} = \vec{v}_1 \tag{1.25}$$

$$\rho = \rho_0 + \rho_1 \tag{1.26}$$

$$p = p_0 + p_1 \tag{1.27}$$

$$\vec{B} = \vec{B}_0 + \vec{b}_1 \tag{1.28}$$

$$\vec{E} = \vec{e}_1 \tag{1.29}$$

and neglecting terms of second order perturbations. Substituting $\vec{E}$ from (1.21) in (1.19) and $\vec{j}$ from (1.20) in (1.18) one obtains

$$\frac{\partial \rho_1}{\partial t} + \rho_0 \nabla \cdot \vec{v}_1 = 0, \tag{1.30}$$

$$\rho_0 \frac{\partial \vec{v}_1}{\partial t} = -\nabla \left[p_1 + \frac{\vec{B}_0 \cdot \vec{b}_1}{\mu_0} \right] + \left(\frac{\vec{B}_0}{\mu_0} \cdot \nabla \right) \vec{b}_1, \tag{1.31}$$

$$\frac{\partial \vec{b}_1}{\partial t} = \nabla \times (\vec{v}_1 \times \vec{B}_0) = (\vec{B}_0 \cdot \nabla)\vec{v}_1 - (\nabla \cdot \vec{v}_1)\vec{B}_0. \tag{1.32}$$

This is a set of three coupled partial differential equations for four unknowns (the perturbations). Closure of this set is reached by using the adiabatic equation of

state ($\hat{S}$ and γ denote the entropy and the adiabatic constant, respectively)

$$p\,\rho^{-\gamma} = \hat{S}. \tag{1.33}$$

From the linearised adiabatic equation (1.33) and the continuity equation (1.17) it follows that

$$\frac{\partial p_1}{\partial t} = -\gamma p_0 \nabla \cdot \vec{v}_1. \tag{1.34}$$

Differentiating (1.31) with respect to time and inserting (1.30), (1.32) and (1.34) one obtains the following differential equation of second order

$$\begin{aligned}\rho_0 \frac{\partial^2 \vec{v}_1}{\partial t^2} &= \nabla\left[\left(\gamma p_0 + \frac{B^2}{\mu_0}\right)(\nabla\cdot\vec{v}_1)\right] - \nabla\left[\frac{\vec{B}_0}{\mu_0}\cdot(\vec{B}_0\cdot\nabla)\vec{v}_1\right] \\ &\quad - \frac{1}{\mu_0}(\vec{B}_0\cdot\nabla)\left[\vec{B}_0(\nabla\cdot\vec{v}_1) - (\vec{B}_0\cdot\nabla)\vec{v}_1\right]\end{aligned} \tag{1.35}$$

Under the assumption that the perturbations are plane waves, i.e. proportional to $\exp[i(\vec{k}\cdot\vec{r}-\omega t)]$ one can substitute $\partial/\partial t \to -i\omega$ and $\nabla \to i\vec{k}$. One then obtains under the assumption that the background magnetic field is uniform

$$\begin{aligned}\omega^2\vec{v}_1 - \left(v_s^2 + v_A^2\right)\left(\vec{k}\cdot\vec{v}_1\right)\vec{k} - \\ \left(\vec{v}_A\cdot\vec{k}\right)\left[\left(\vec{v}_A\cdot\vec{k}\right)\vec{v}_1 - \left(\vec{v}_A\cdot\vec{v}_1\right)\vec{k} - \left(\vec{k}\cdot\vec{v}_1\right)\vec{v}_A\right] = 0,\end{aligned} \tag{1.36}$$

where the Alfvén velocity

$$\vec{v}_A = \frac{\vec{B}_0}{\sqrt{\mu_0\rho_0}} \tag{1.37}$$

and the speed of sound

$$v_s = \sqrt{\gamma \frac{p_0}{\rho_0}} \tag{1.38}$$

have been introduced.

By multiplying (1.36) by $\vec{k}$ and $\vec{v}_A$ one obtains

$$\left[\omega^2 - \left(v_s^2 + v_A^2\right) k^2\right] \left(\vec{k} \cdot \vec{v}_1\right) + \left(\vec{v}_A \cdot \vec{k}\right) \left(\vec{v}_A \cdot \vec{v}_1\right) k^2 = 0 \tag{1.39}$$

and

$$\omega^2 \left(\vec{v}_A \cdot \vec{v}_1\right) - v_s^2 \left(\vec{k} \cdot \vec{v}_1\right) \left(\vec{v}_A \cdot \vec{k}\right) = 0 \tag{1.40}$$

It is instructive to continue the discussion of the above dispersion relation into that of the transverse ($\vec{k} \cdot \vec{v}_1 = 0$) and the longitudinal ($\vec{k} \cdot \vec{v}_1 \neq 0$) wave mode.

1.2.1 Transverse Mode

This wave mode is characterised by the fact that the wave vector is perpendicular to the velocity perturbation, i.e.

$$\vec{k} \cdot \vec{v}_1 = 0. \tag{1.41}$$

This condition is equivalent to $\nabla \cdot \vec{v}_1 = 0$, i.e. assuming that the fluid is incompressible.

From (1.40) it then follows that $\vec{v}_A \cdot \vec{v}_1 = 0$, i.e. that the perturbations in the velocity $\vec{v}_1$ are perpendicular to the Alfvén velocity and hence the background mag-

netic field $\vec{B}_0$. From Faraday's law, the "frozen-in" condition and the plane wave approach it follows

$$\omega\vec{b_1} = \vec{k} \times (\vec{v_1} \times \vec{B_0}) = (\vec{B_0} \cdot \vec{k})\vec{v_1} - (\vec{k} \cdot \vec{v_1})\vec{B_0} = (\vec{B_0} \cdot \vec{k})\vec{v_1} \tag{1.42}$$

where the second term on the right side is zero because of the transversal wave approach. From (1.42) follows that the magnetic perturbations $\vec{b_1}$ are parallel to $\vec{v_1}$ and therefore perpendicular to $\vec{k}$.

From Faraday's law one can deduce that

$$\vec{b_1} = \frac{1}{\omega}\vec{k} \times \vec{e_1}, \tag{1.43}$$

i.e. $\vec{b_1}$ is perpendicular to $\vec{e_1}$.

Using the above mentioned conditions, i.e. $\vec{k} \cdot \vec{v_1} = 0$ and $\vec{v_A} \cdot \vec{v_1} = 0$, (1.36) simplifies to

$$\omega^2\vec{v_1} - \left(\vec{v_A} \cdot \vec{k}\right)^2 \vec{v_1} = 0. \tag{1.44}$$

The dispersion relation for the transverse mode is then found to be

$$\omega^2 = \left(\vec{v_A} \cdot \vec{k}\right)^2 = v_A^2 \; k^2 \; \cos^2\theta \tag{1.45}$$

where θ is the angle between the background magnetic field $\vec{B}_0$ and the wave vector $\vec{k}$. The transverse wave mode is sometimes called shear Alfvén or simply Alfvén mode.

From the dispersion relation it is clear that transverse waves cannot propagate perpendicular to the background magnetic field, a property which is of great impor-

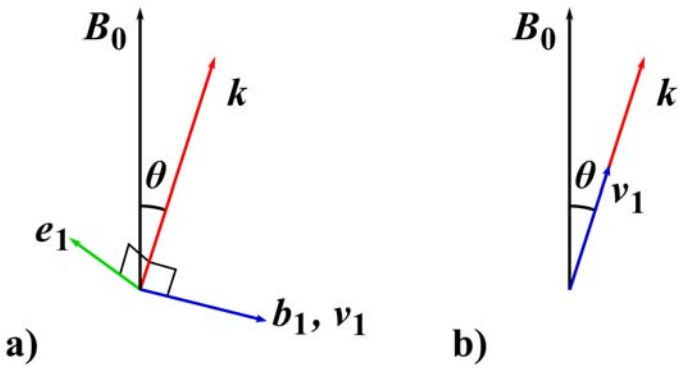

Figure 1.8: Orientation of various perturbations associated with the transverse a) and longitudinal b) wave mode.

tance in the magnetospheric context.

The group velocity $\vec{v}_g$ is found to be the Alfvén velocity:

$$\vec{v}_g = \frac{\partial \omega}{\partial \vec{k}} = \vec{v}_A. \tag{1.46}$$

According to (1.37) the Alfvén velocity is in direction of the background magnetic field and we can hence deduce that the energy of transverse waves always travels along $\vec{B}_0$ with Alfvénic speed. The transverse mode is illustrated in Fig. 1.8 a).

From the continuity equation (1.17) it follows that the transverse wave is also not associated with density perturbations. This indicates that this wave mode can travel long distances without being damped.

$$\frac{\partial \rho_1}{\partial t} = -\rho_0 \nabla \cdot \vec{v}_1 \rightarrow -i\omega\rho_1 = -\rho_0 \vec{k} \cdot \vec{v}_1 = 0 \tag{1.47}$$

1.2.2 Longitudinal Waves

Inserting (1.39) into (1.40) we find

$$\left[\omega^2 - \left(v_s^2 + v_A^2\right) k^2 + \frac{k^2 v_s^2}{\omega^2}\left(\vec{v}_A \cdot \vec{k}\right)^2\right]\left(\vec{k} \cdot \vec{v}_1\right) = 0. \tag{1.48}$$

Since in the longitudinal case $\vec{k} \cdot \vec{v}_1 \neq 0$, we find the dispersion relation as

$$\omega^4 - \omega^2 k^2 \left(v_s^2 + v_A^2\right) + v_s^2 k^2 \left(\vec{v}_A \cdot \vec{k}\right)^2 = 0 \tag{1.49}$$

which has the following solutions

$$\omega = \left\{\frac{1}{2}k^2\left[v_s^2 + v_A^2 \pm \sqrt{\left(v_s^2 + v_A^2\right)^2 - 4\frac{v_s^2}{k^2}\left(\vec{v}_A \cdot \vec{k}\right)^2}\right]\right\}^{1/2}. \tag{1.50}$$

The two solutions are sometimes called the fast and slow mode. It can be easily shown that the group velocity and hence the direction of energy propagation is in the direction of the propagation of the wave, i.e. $\partial\omega/\partial\vec{k} \parallel \vec{k}$.

It is instructive to discuss some special cases of (1.50). In the case of wave propagation parallel to the field direction ($\vec{k} \parallel \vec{B}_0$), two solutions are possible:

$$\text{A: } \omega = k v_A \tag{1.51}$$

$$\text{B: } \omega = k v_s. \tag{1.52}$$

In the case of field perpendicular propagation ($\vec{k} \perp \vec{B}_0$), the above dispersion relation has one solution, namely

$$\omega = k\sqrt{v_A^2 + v_s^2}. \tag{1.53}$$

In a cold plasma limit the velocity of sound v_s is much smaller than v_A. It is then easily followed from 1.53 that the dispersion relation for field perpendicular propagation of the fast mode is similar to that of the transverse mode. This wave mode is often called the compressional Alfvén wave or simply the compressional mode:

$$\omega = kv_A \tag{1.54}$$

However the key difference between the shear Alfvén mode and the compressional mode is that (1.54) does not involve the dot product of vectors and the energy travels in the direction of the k-vector. Hence the fast mode is capable of transporting energy across magnetic field lines, an ability that the Alfvén mode does not possess.

1.2.3 Mode Coupling

As was seen in the previous section, the two wave modes (transverse and longitudinal) are uncoupled in the case of homogeneous plasma density and magnetic field. In a more general case where the magnetic field is still homogeneous but the plasma density is dependent on position, the wave equations for the compressional and Alfvén mode are coupled in the cold plasma limit ($v_s \rightarrow 0$). It is hence conceivable that an energy exchange between the two modes can take place.

Southwood (1974) treated this simplified case of a plasma with varying mass density $\rho(x)$ permeated by a uniform magnetic field in the z-direction $B_0\vec{\hat{z}}$. The electric and magnetic field are then given by

$$\vec{E} = \vec{e}_1 = \begin{pmatrix} e_x \\ e_y \\ 0 \end{pmatrix} e^{i\xi y}\, e^{ikz}\, e^{-i\omega t} \tag{1.55}$$

and

$$\vec{B} = \vec{B}_0 + \vec{b}_1 = \begin{pmatrix} 0 \\ 0 \\ B_0 \end{pmatrix} + \begin{pmatrix} b_x \\ b_y \\ b_z \end{pmatrix} e^{i\xi y}\, e^{ikz}\, e^{-i\omega t} \tag{1.56}$$

Again, the basic MHD equations (1.18), (1.21) and (1.20) are linearised and combined in a similar fashion as shown in the Sec. 1.2, this time however not eliminating the electric field.

As in the scenario before, two wave modes exist, the fast and the shear Alfvén mode. However, the equations for both electric field amplitudes e_x and e_y are now coupled. Assuming dependencies as given by (1.55) and (1.56) the resulting differential equation takes the form

$$i\omega\rho\vec{e}_1 = \left(\frac{1}{\mu_0}\left(\nabla \times \vec{b}_1\right) \times \vec{B}_0\right) \times \vec{B}_0. \tag{1.57}$$

Working out the differentiations the two components of $\vec{e}_1$ take the form

$$i\omega\rho\mu_0 e_x = B_0^2\left(ikb_x - i\xi b_z\right) \tag{1.58}$$

and

$$i\omega\rho\mu_0 e_y = B_0^2\left(\frac{db_z}{dx} - ikb_x\right) \tag{1.59}$$

Introducing the Alfvén speed as $v_A^2 = B_0^2/\mu_0\rho$ and using Faraday's law (1.19) to eliminate the magnetic field perturbations one obtains

$$\left(\frac{\omega^2}{v_A^2} - k^2\right) e_x = i\xi \left(\frac{de_y}{dx} - i\xi e_x\right) \tag{1.60}$$

and

$$\left(\frac{\omega^2}{v_A^2} - k^2\right) e_y = -\frac{d}{dx}\left(\frac{de_y}{dx} - i\xi e_x\right) \tag{1.61}$$

Introducing $K^2 = \omega^2/v_A^2$, the amplitude of the fast mode (e_y) is then found to be

$$(K^2 - k^2)e_y = \frac{d}{dx}\left(\frac{K^2 - k^2}{K^2 - k^2 - \xi^2}\frac{de_y}{dx}\right) \tag{1.62}$$

or

$$\frac{d^2e_y}{dx^2} - \xi^2\frac{dK^2}{dx}\frac{1}{(K^2 - k^2)(K^2 - k^2 - \xi^2)}\frac{de_y}{dx} + (K^2 - k^2 - \xi^2)e_y = 0. \tag{1.63}$$

Notice that (1.63) is of the same form as the differential equation describing a simple, damped harmonic oscillator.

Clearly, (1.63) has two singular points: one where $K^2 - k^2 - \xi^2 = 0$ at $x = x_1$ and the second where $K^2 - k^2 = 0$ at $x = x_0$. The first one $x = x_1$ is interpreted as a turning point, where the nature of the fast wave changes from oscillatory to exponentially growing or decaying over distance. $x = x_0$ is interpreted as the position where the transverse mode is in resonance with the shear Alfvén mode.

The problem that the solutions of (1.63) tend to infinity at both singular points is dealt with by introducing a small but finite damping term into the equations.

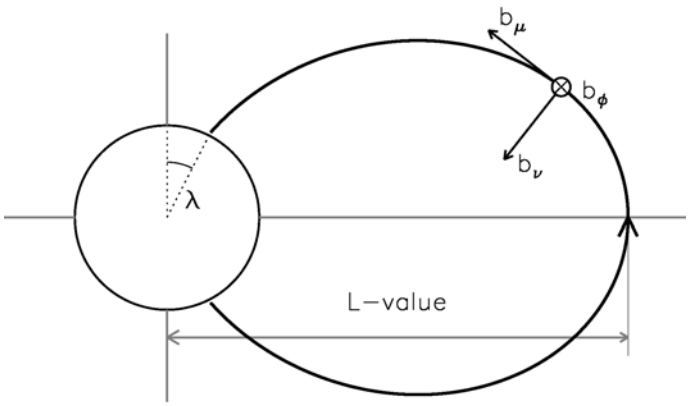

Figure 1.9: Orientation of the dipolar coordinate system.

Southwood (1974) is also able to show from energy considerations that if energy is available, that there is always a finite flux of energy into the region of the resonance.

1.2.4 MHD waves in a dipole magnetic field

The same principal picture of mode coupling between the compressional and shear Alfvén wave also applies to more complex geometries. However, in the dipole geometry another wave mode is introduced due to the field line curvature.

To discuss waves in a dipolar magnetic field it is convenient to use a orthogonal curvilinear coordinate system with $\vec{\hat{\mu}}$ in the magnetic field direction, $\vec{\hat{\phi}}$ in the eastward azimuthal direction and $\vec{\hat{\nu}}$ inwards towards the centre of curvature. The coordinate system is sketched in Fig. 1.9.

Linearising the equation of motion, Faraday's law and the "frozen-in" condition

then yields in the cold plasma limit $v_s \to 0$

$$\rho_0 \frac{\partial \vec{v}_1}{\partial t} = \frac{1}{\mu_0}(\nabla \times \vec{b}_1) \times \vec{B}_0 \tag{1.64}$$

$$\frac{\partial \vec{b}_1}{\partial t} = -\nabla \times \vec{e}_1 \tag{1.65}$$

$$\vec{e}_{1\perp} = -\vec{v}_{1\perp} \times \vec{B}_0 \quad \text{and} \quad e_{1\parallel} = 0 \tag{1.66}$$

Scaled variables $\vec{\mathcal{B}}$ and $\vec{\mathcal{E}}$ are introduced by

$$\mathcal{B}_\mu = h_\mu b_{1\mu} \quad \mathcal{B}_\nu = h_\nu b_{1\nu} \quad \mathcal{B}_\phi = h_\phi b_{1\phi} \tag{1.67}$$

$$\mathcal{E}_\nu = h_\nu e_{1\nu} \quad \mathcal{E}_\phi = h_\phi e_{1\phi}. \tag{1.68}$$

The scaling factors are dependent on standard polar spherical coordinates (r, λ, ϕ) and given by

$$h_\mu = \frac{R_e \cos^6 \lambda}{\nu^3 \sqrt{4 - 3\cos^2 \lambda}} \tag{1.69}$$

$$h_\nu = \frac{R_e \cos^3 \lambda}{\nu^2 \sqrt{4 - 3\cos^2 \lambda}} \tag{1.70}$$

$$h_\phi = \frac{R_e \cos^3 \lambda}{\nu} \tag{1.71}$$

One can then write out the components of (1.64) and (1.65) for plane waves varying with time as $e^{-i\omega t}$, in the curvilinear system. Because of the azimuthal symmetry of the dipole system the dependence on ϕ can be assumed to be $e^{im\phi}$

where m is the azimuthal wave number. One obtains

$$i\omega\mathcal{E}_\nu = \frac{h_\nu}{h_\phi h_\mu} v_A^2 \left[\frac{\partial \mathcal{B}_\phi}{\partial \mu} - im\mathcal{B}_\mu\right] \tag{1.72}$$

$$i\omega\mathcal{E}_\phi = -\frac{h_\phi}{h_\mu h_\nu} v_A^2 \left[\frac{\partial \mathcal{B}_\nu}{\partial \mu} - \frac{\partial \mathcal{B}_\mu}{\partial \nu}\right] \tag{1.73}$$

$$i\omega\mathcal{B}_\mu = \frac{h_\mu}{h_\nu h_\phi} \left[\frac{\partial \mathcal{E}_\phi}{\partial \nu} - im\mathcal{E}_\nu\right] \tag{1.74}$$

$$i\omega\mathcal{B}_\nu = -\frac{h_\nu}{h_\phi h_\mu} \frac{\partial \mathcal{E}_\phi}{\partial \mu} \tag{1.75}$$

$$i\omega\mathcal{B}_\phi = \frac{h_\phi}{h_\mu h_\nu} \frac{\partial \mathcal{E}_\nu}{\partial \mu}. \tag{1.76}$$

Generally, these equations are coupled and qualitatively the same conclusions about mode coupling as discussed in the previous section apply in the dipolar geometry (Chen and Hasegawa, 1974). However, for two special cases the equations decouple into two sets of equations. For $m = 0$, i.e. a wave with no phase variation with longitude, the first set of equations describes pulsations where the motion is entirely azimuthal, consisting of a perturbation in $e_{1\nu}$ and $b_{1\phi}$. This mode is called the toroidal mode. The perturbations in the other three components describe the compressional or fast mode ($b_{1\mu} \neq 0$).

Alternatively, the above set of equations decouples for the case $m \to \infty$, which describes a wave with an azimuthal wavelength that is much smaller then all other length scales. For this case, (1.72) and (1.74) can only be fulfilled if $\mathcal{B}_\mu = 0$ and $\mathcal{E}_\nu = 0$. It then follows that the perturbation associated with that wave mode is confined to $b_{1\nu}$ and $e_{1\phi}$. This wave mode is called the poloidal mode.

Both the toroidal and poloidal oscillations are decoupled and localised to a particular L-shell, i.e. to field lines all having the same L-value. The L-value of a magnetic field line is the geocentric distance where the field line crosses the magnetic equator

(see Fig. 1.9). Both solutions of the decoupled wave equations are standing waves on magnetic field lines, much like waves on a guitar string. As the ionosphere, which forms the boundary on both sides of any closed magnetic field line, can be approximated by a perfect conductor, the electric field has to assume nodes at the ends of the pulsating field line. This fact qualitatively determines the node structure for pulsations standing on magnetic field lines.

The orientations of the perturbation fields associated with the two fundamental transverse Alfvénic wave modes on a dipole field line are sketched in Fig. 1.10. When the variation of the magnetic field is indicated, the field line is coloured blue, for the electric field it is coloured orange. In a) the magnetic and electric field perturbations of the fundamental poloidal mode are shown. The electric field varies in the azimuthal direction whereas the magnetic field perturbation is confined within the meridional plane of the field line concerned. This situation is reversed for the toroidal wave mode delineated in part b) of Fig. 1.10.

1.2.5 Field Line Resonances in the Magnetosphere

All theoretical work presented in the previous sections was motivated by observations of pulsations in data from ground-based magnetometers and high-frequency (HF) radars. Such geomagnetic pulsations in the ultra-low frequency (ULF) wave band have frequencies between 1 Hz and 1 mHz, i.e. their frequencies range from the local ion gyrofrequency to the lowest frequency the magnetospheric cavity can support.

A popular scheme by Jacobs et al. (1964) categorises micropulsations according to their frequency and form (continuous or irregular). This scheme is reproduced in Tab. 1.1. From the zoo of waves occurring in the Earth's magnetosphere one special type of pulsation attracted much attention - it is called the Field Line Resonance or

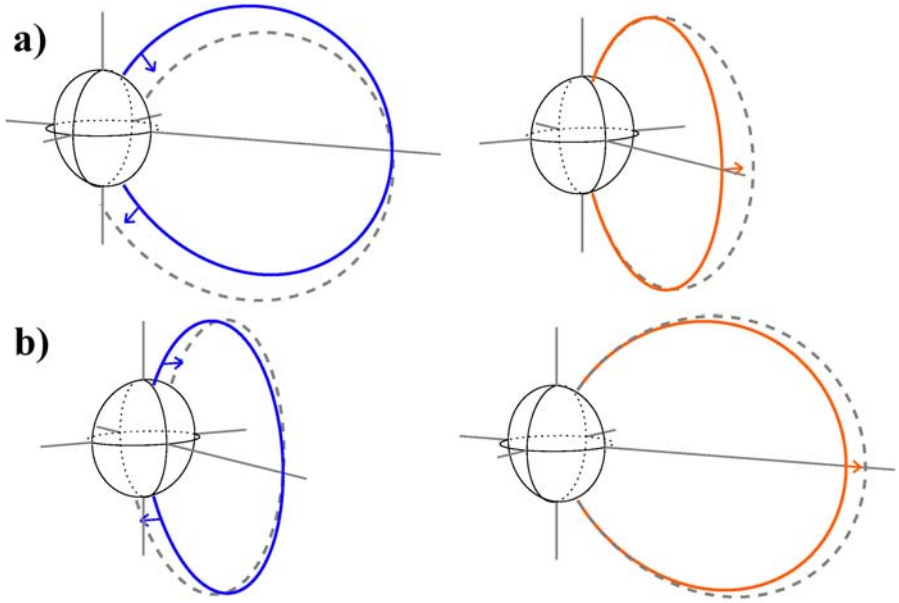

Figure 1.10: Orientation of the magnetic and electric perturbation fields associated with the fundamental poloidal and toroidal oscillations shown in panels a) and b), respectively.

	continuous					irregular	
	Pc1	Pc2	Pc3	Pc4	Pc5	Pi1	Pi2
T [s]	0.2-5	5-10	10-45	45-150	150-600	1-40	40-150
f [mHz]	200-5000	100-200	22-100	7-22	2-7	25-1000	2-25

Table 1.1: Classification of geomagnetic micropulsations according to Jacobs et al. (1964).

FLR for short which at high latitudes usually occurs in the Pc5 frequency range.

This pulsation type is characterised by the fact that it is observed with the same frequency on field lines covering a wide range of L-values. Intuitively, the frequency at which a field line supports eigenoscillations, i.e. standing waves on that field line, is somehow related to the field line length. For a dipole field, the equation describing a field line depending on the L-value L and the co-latitude λ (see Fig. 1.9) is given by

$$r(\lambda) = L \sin^2 \lambda, \quad 0 \leq \lambda \leq \pi \tag{1.77}$$

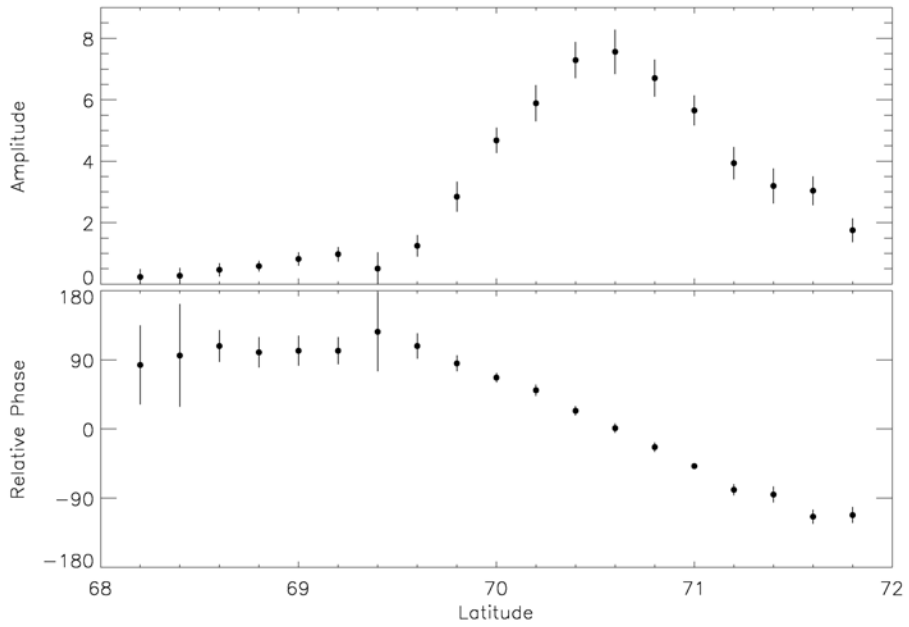

Figure 1.11: Typical latitude profiles of the power and phase at the centre frequency of the FLR (adapted from Walker et al., 1979).

The field line length $\mathcal{L}$ depending on the co-latitudes where it crosses the Earth's surface in the southern and northern hemisphere λ_S and λ_N is then given by

$$\mathcal{L} = \int_{\lambda_S}^{\lambda_N} \sqrt{r^2 + \left(\frac{\partial r}{\partial \lambda}\right)^2}\, d\lambda = L \int_{\lambda_S}^{\lambda_N} \sin\lambda \sqrt{1 + 3\cos^2\lambda}\; d\lambda \approx 2.45L \tag{1.78}$$

Over a range of 2° from 29° to 31° co-latitude, $\mathcal{L}$ varies by about 10%.

The central characteristics of a FLR is shown in Fig. 1.11. The figure was compiled from Fourier spectra of time series measured at different latitudes by a coherent scatter HF radar presented in Walker et al. (1979). It shows latitude profiles of the Fourier power and phase on day 303 of 1977. The power and phase profile were obtained at a frequency of 3.906 mHz, which was the centre frequency of the observed pulsation.

The power profile shows a clear peak at one latitude along with a 180° phase

shift across that latitude. Both features were predicted for a standing wave on geomagnetic field lines (Southwood, 1974; Chen and Hasegawa, 1974). The latitude at which the maximum power is reached is that at which the frequency of the driver matches the field line eigenfrequency. According to standard resonance theory the phase of the pulsation changes by 180° across the resonant latitude as shown in the bottom panel of Fig. 1.11.

Although the power profile shows that FLRs are usually localised at a particular L-shell, the Full-Width-Half-Maximum of the peak in Fig. 1.11 is about 1° wide. This indicates that L-shell cannot resonate entirely independently as predicted by the wave equation presented in Sec. 1.2.4.

The direction in which FLRs produce the strongest signature indicates that they are usually of the toroidal wave mode, the electric and magnetic field perturbations orientated as shown in the bottom panels of Fig. 1.10.

The essential ingredients leading to the formation of resonances in the terrestrial magnetosphere are delineated in Fig. 1.12. The Kelvin-Helmholtz instabilities (KHI) on both flanks of the magnetosphere were identified as possible sources for compressional waves travelling across closed magnetic field lines into the inner magnetosphere. As the Alfvén velocity inside the magnetosphere changes the compressional wave eventually reaches its turning point, as described by one of the singularities of (1.63). The contour of the turning point is shown as the solid line in Fig. 1.12.

Further inside from the turning point, the compressional wave continues evanescently. If it encounters a magnetic field line whose eigenfrequency matches that of the compressional waves, energy is exchanged from the first to the latter and a standing Alfvénic wave is formed at the resonance position as given by the second singular point in (1.63).

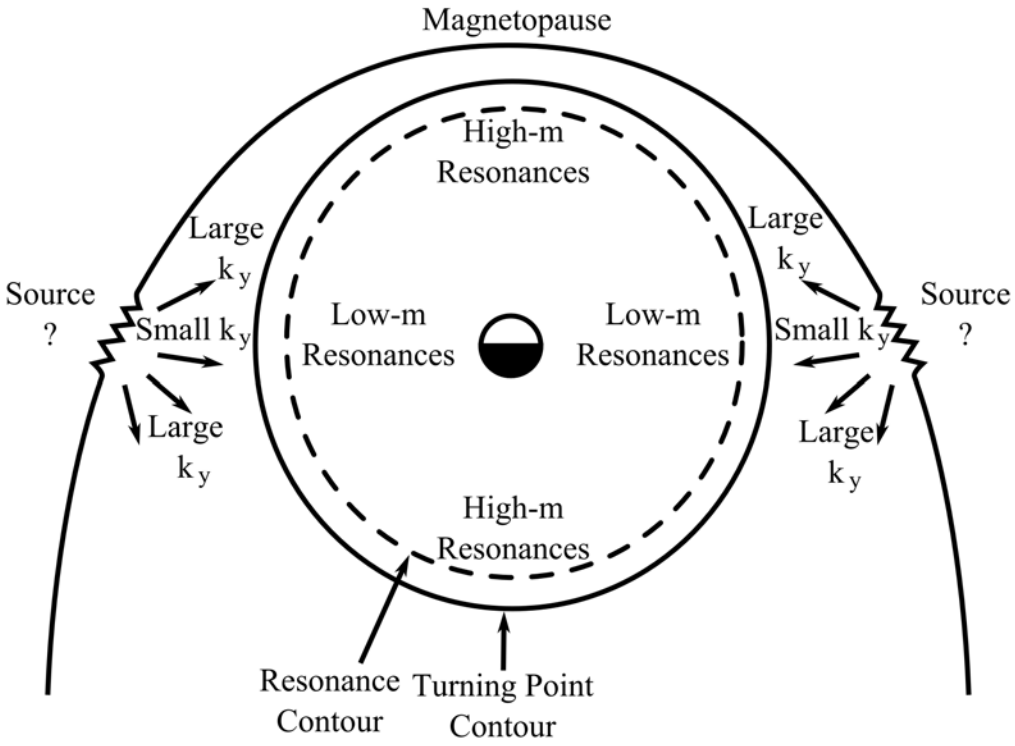

Figure 1.12: Schematic of the driving process of FLRs (adapted from Fenrich et al., 1995).

Before the concept of FLRs was established, Samson and Rostoker (1972) conducted a statistical study of such pulsation events observed in ground-based magnetometer data spread over Canada. They found certain polarisation characteristics dependent on local time which could be explained by the theories presented in Southwood (1974) and Chen and Hasegawa (1974).

Fenrich et al. (1995) elaborated the picture from Southwood (1974) and Chen and Hasegawa (1974) by deducing from their observational evidence, that FLRs with low azimuthal wave numbers m are more likely to be found around dusk and dawn, i.e. generated by fast modes originating from the KHI with small azimuthal wave vectors k_y.

The KHI is not the only source for fast waves driving FLRs. It is known that discontinuities in the solar wind, such as sudden increases in dynamic pressure, can excite FLRs in the magnetosphere (Rostoker and Sullivan, 1987). Mann and Wright (1999) explore the observational differences of FLRs driven by the two mechanisms. They suggest that morningside FLRs are predominantly driven by solar wind velocity shear whereas solar wind impulses are responsible for most of the eveningside FLRs.

Whereas pulsations measured on the ground are often highly monochromatic and last for up to several hours while having the same frequency over a range of L-values and local time, observations in space are quite different. Spectrograms of magnetic field data obtained by the AMPTE/CCE satellite were presented by Engebretson et al. (1986) and are reproduced in Fig. 1.13.

The AMPTE/CCE satellite orbited Earth on a highly elliptic orbit with a perigee of 800 km and an apogee of 8.8 R_e close to the equatorial plane. In Fig. 1.13 spectrograms of the three magnetic field components equivalent to b_ν, b_ϕ and b_μ are

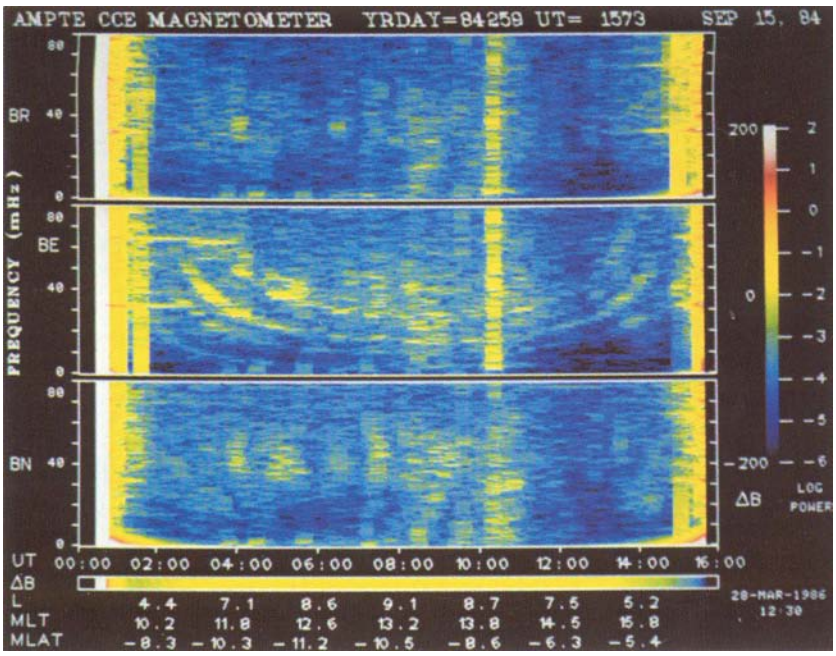

Figure 1.13: Figure taken from Engebretson et al. (1986). It shows the three component dynamic power spectra of magnetic field data for a full orbit from 0025 to 1604 UT on 15 September 1984. Apogee is at the centre of the figure.

shown for a full orbit on 15 September 1986. The spectrograms start at perigee, apogee is in the centre of the figure.

As the satellite moved across field lines, the power in the component associated with toroidal pulsations (middle panel, b_ϕ) was organised in harmonically related bands, the frequency of maximum power varying smoothly with L-value. As the L-value increases (towards the centre of Fig. 1.13), the frequencies at which power was observed decreased, as intuitively expected as the field line length increased. The results of Fig. 1.13 are very similar to what will be presented in Cha. 5.

Numerical studies of mode coupling in a dipolar geometry were presented in Lee and Lysak (1989) and Lee and Lysak (1991). These studies reproduced the predictions by Southwood (1974) and Chen and Hasegawa (1974) which were outlined in Sec. 1.2.3, i.e. that mode coupling between compressional and shear Alfvén waves

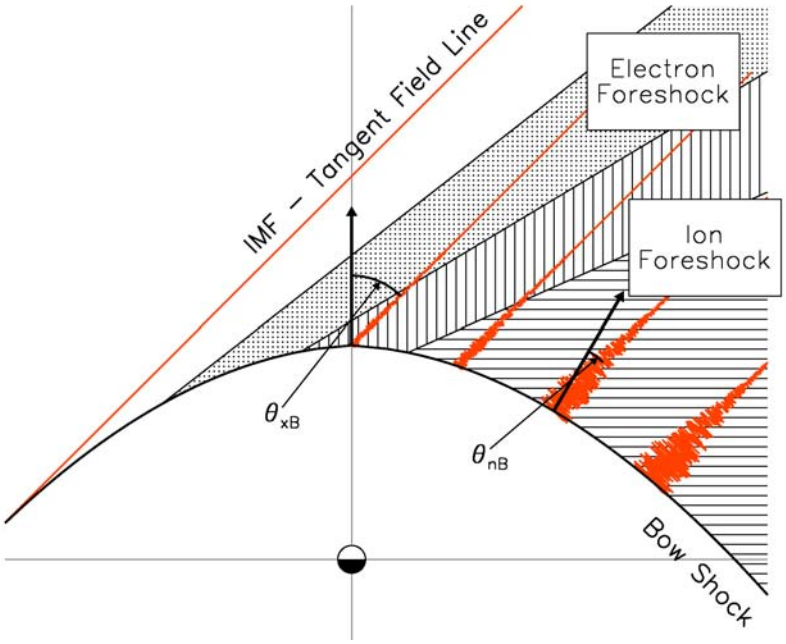

Figure 1.14: Schematic of the foreshock region.

can take place and that a sharp resonance region is formed. They were also able to show that broad band compressional power will lead to the generation of Alfvénic continuum as presented in Fig. 1.13.

1.2.6 Upstream Generated Waves

The region upstream of the bow shock is called the foreshock and is usually very dynamic. As outlined in Sec. 1.1.3 the physical processes at work depend heavily on the foreshock geometry, i.e. mainly on the angle between the IMF and the local shock normal θ_{nB}.

As the bow shock is associated with an increase in magnetic field strength, it acts as a magnetic mirror and charged particles can be reflected. Since they are gyrating around the local magnetic field, they can travel against the solar wind stream only if θ_{nB} is small, otherwise they are lost in the shock.

The IMF is "frozen-in" the solar wind plasma and hence the IMF forms a Archimedes spiral as one moves further away from the Sun. Due to this garden hose effect, the cone angle at the Earth's distance from the Sun is usually around 45°, as indicated by the red solid lines in Fig. 1.14. This means that in the Earth's orbital plane the shock on the dusk side of Earth is usually quasi-parallel whereas it is quasi-perpendicular on the dawn side.

Field lines further downstream than the tangent field line are connected to the shock where θ_{nB} is increasingly less than 90°. In principle one should find reflected particles in the entire region downstream of the tangent field lines. However, one tends to find that electrons appear first. The region where reflected electrons but no ions are observed is called the electron foreshock as indicated by the shaded area in Fig. 1.14.

Following even further downstream is a region where ions travelling against the solar wind stream are observed, the so-called ion foreshock. Here $\theta_{nB} < 70°$ and about 2% of the solar wind ions are reflected.

This region can be subdivided into two regions with distinctly different ion populations (Gosling et al., 1978). The first region in the ion foreshock is filled by vertical lines in Fig. 1.14. It is characterised by an ion population which has a narrow peak in velocity phase space. This population was termed "reflected" ions. The further downstream one measures the ion distribution functions, the more diffuse the ions become in velocity space - hence this population has been termed "diffuse" ions. The area where diffuse ion populations are found is filled with horizontal lines in Fig. 1.14. The transition between the two regions is not as sharp as it might be suggested by Fig. 1.14. Instead, the transition is gradual and an "intermediate" population with a kidney-shaped velocity distribution follows the peaked populations.

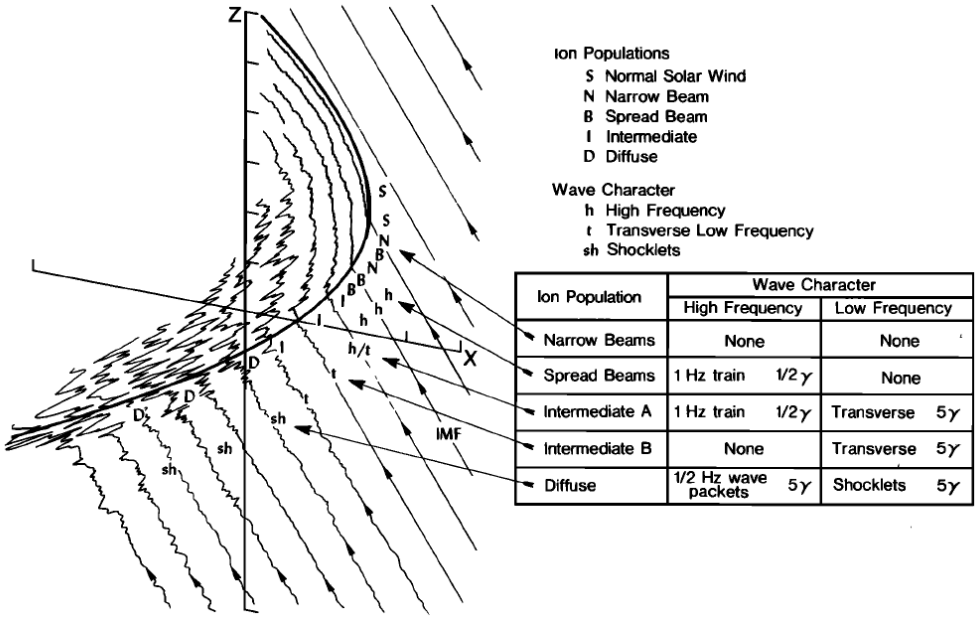

Ion Population	Wave Character	
	High Frequency	Low Frequency
Narrow Beams	None	None
Spread Beams	1 Hz train 1/2γ	None
Intermediate A	1 Hz train 1/2γ	Transverse 5γ
Intermediate B	None	Transverse 5γ
Diffuse	1/2 Hz wave packets 5γ	Shocklets 5γ

Figure 1.15: Schematic of the region upstream of the terrestrial bow shock. Indicated are the ion populations and the various hydromagnetic waves as inferred by Hoppe et al. (1981).

Paschmann et al. (1979) found a close connection between the diffuse ions and the occurrence of hydromagnetic wave activity in the foreshock region. There appear to be no hydromagnetic waves when reflected ions are observed. This observation has been indicated by the wavy patterns on the IMF field lines in red in Fig. 1.14. A summary of the observed hydromagnetic waves and ion populations observed is given in Fig. 1.15.

Paschmann et al. (1979) presented the first in-situ evidence for the generation of ULF waves by particles reflected at the bow shock, however the control of ULF waves by the IMF had been studied before. Troitskaya et al. (1971) realised that whenever the cone angle θ_{xB} of the IMF dropped below a certain threshold enhanced ULF power was observed in the dayside magnetosphere by ground-based magnetometers.

Troitskaya et al. (1971) explained this observation by attributing the wave gen-

eration process to populations of backstreaming ions at the bow shock which are most likely to occur during times of low cone angles. These backstreaming ions resonantly interact with naturally occurring waves in the solar wind, amplifying them (Sentman et al., 1981). Since the propagation speed for ULF waves in the solar wind is significantly lower than the solar wind flow speed, these ULF waves are convected downstream towards Earth. The compressional waves then cross the bow shock, magnetosheath and magnetopause without significant changes to their spectrum (Krauss-Varban, 1994).

Whereas the direction of the IMF controls whether waves are generated at the bow shock or not, the strength of the IMF controls the peak frequency at which waves are generated. Takahashi et al. (1984) used ATS 6 magnetic field data to find that the peak frequency of waves observed inside the dayside magnetosphere f was dependent on the IMF strength B_{tot} and the cone angle θ_{xB} as

$$f[\text{mHz}] = 7.6\ B_{tot}\ \cos^2\theta_{xB}. \tag{1.79}$$

Observational evidence supporting this mechanism is available in abundance. It has been studied in detail using satellites in the solar wind (e.g. Le and Russell, 1992a,b), in the dayside magnetosphere (e.g. Arthur and McPherron, 1977) and ground-based magnetometers (e.g. Webb and Orr, 1976). Comprehensive reviews of the research done on upstream generated waves and their interaction with the dayside magnetosphere in the 1970's and 1980's can be found in Odera (1986) and Greenstadt et al. (1981).

Using magnetic field data from the ISEE 1 and 2 satellites the morphology of upstream waves within the solar wind medium is well documented by Le and Russell (1992a) and Le and Russell (1992b). They found that the ULF foreshock, i.e. the

boundary that separates the disturbed and undisturbed upstream magnetic field, begins at an angle of 50° between the IMF and the bow shock normal. The entire region connected to the bow shock with smaller angles is filled by waves.

During an inbound pass of the ISEE spacecraft, Le and Russell (1992b) observed waves up to 5 R_e upstream of the Earth bow shock. The upstream waves became stronger, more compressional and more linearly polarised the closer they were observed to the bow shock. They also found that the spectral peak of the generated waves became broader the closer they were observed at the bow shock whereas the peak frequency stayed constant as long as the IMF strength did not change. Directly behind the bow shock the peak spanned frequencies from about 10 to 100 mHz.

Once the upstream generated waves enter the dayside magnetosphere they can couple to shear Alfvén waves where the frequency of the incoming compressional wave matches one of the eigenfrequencies of a field line. The resulting Alfvénic continuum has been observed by Engebretson et al. (1986). As the upstream generation process for the compressional waves is broad band compared to the spectrum of eigenfrequencies of field lines in the dayside magnetosphere, a multi-harmonic Alfvénic continuum is often observed.

Chi and Russell (1998) used electric and magnetic field data from the ISEE 1 spacecraft to determine energy propagation directions from the Poynting fluxes of waves in the dayside magnetosphere. They found that at higher frequencies (7-100 mHz) only few waves are standing while most are travelling. They also found a tendency for waves to travel anti-sunward, clearly indicating an upstream source.

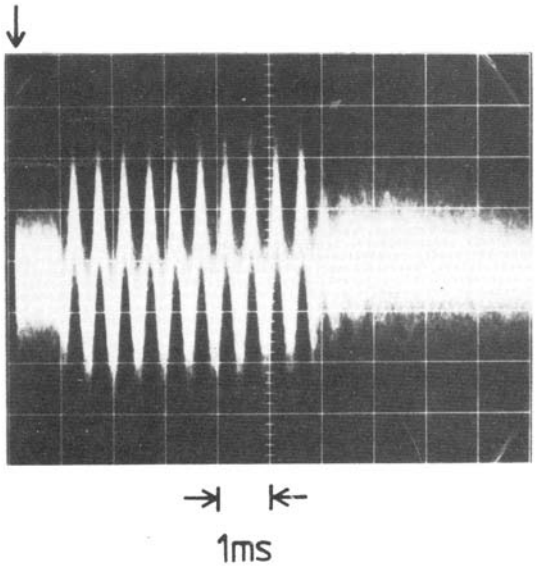

Figure 1.16: Magnetic field of a VLF wave generated by a HF pulse of 5 ms duration, amplitude modulated at 2 kHz. The start time of the HF pulse is indicated by the arrow. The picture represents a photographic average over a few hundred pulses (from Stubbe et al., 1982).

1.2.7 Artificial Waves

It is well known that powerful High Frequency (HF) radio waves, transmitted from the ground, can efficiently increase the electron temperature T_e in the ionospheric D- and E-regions (e.g. Meltz et al., 1974). Such artificial temperature changes occur with a very short time constant, typically 1 ms (at 90 km altitude) after the heater is switched on and subsequently increase the Pedersen conductivity σ_P locally.

With a longer time constant of several seconds (at 90 km altitude) the electron density is increased due to the impact of HF heating on recombination rates (Stubbe et al., 1982). The variations in the local electron temperature and density subsequently change the local Pedersen and Hall conductivity, σ_P and σ_H.

If the HF power is applied with a modulation frequency f, the conductivities will also be modulated with a frequency f. In the presence of a natural ionospheric DC

current, an AC component will thus be superimposed and the heated patch will act as a giant antenna, emitting hydromagnetic waves at the modulation frequency. A comprehensive theoretical framework of modulated heating based on earlier work by Stubbe and Kopka (1977) is given in Borisov and Stubbe (1997).

If f is in the ELF/VLF range, the modulation is too fast to significantly affect the electron density with its large time constant. However, still a significant effect on the local electron temperature is achieved. In this case, only the comparatively small Pedersen conductivity σ_P is affected and the modulated current will radiate ELF/VLF waves with frequency f.

In Stubbe et al. (1982) the results of an experiment using the ionospheric heater near Tromsø is described. The heater emitted a HF pulse of 5 ms duration with an amplitude modulated at 2 kHz into the ionosphere. The averaged magnetic signal resulting from a few hundred pulses is shown in Fig. 1.16. The arrow marks the beginning of each pulse.

The 1 ms delay between the HF pulse and the onset of magnetic pulsations is clearly visible. During the pulse the magnetic field oscillates as predicted at the modulation frequency. Additionally it can be seen from Fig. 1.16 that the pulsations continued for about 2 cycles after the heater has been turned off.

If f is small enough to allow for changes in the local electron density (ULF range) both σ_P and σ_H are affected. Again, if a natural DC current is present, an AC component will be superimposed. Although in this case the effective radiated power of the virtual antenna is small, the amplitude of the local magnetic disturbance is large.

A number of heating experiments at ELF/VLF (e.g. Stubbe et al., 1982) and ULF (e.g. Stubbe and Kopka, 1981; Kornienko et al., 2003) frequencies have been

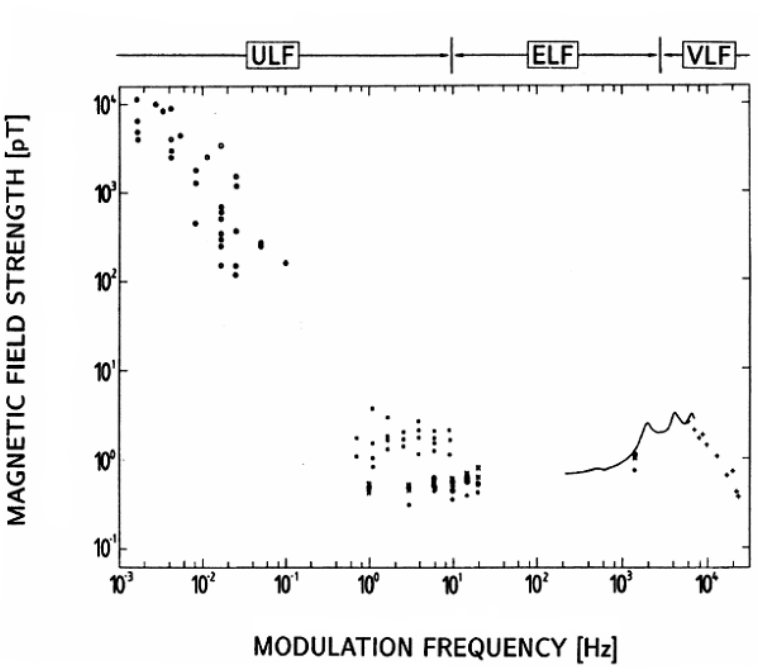

Figure 1.17: Results from several years of ionospheric heating experiments gathered by Stubbe (1996).

conducted since the 1970s. An overview of heating experiments done with the heater facility located near Tromsø, Norway, at various modulation frequencies can be found in Stubbe (1996).

Stubbe (1996) compiled a figure of the amplitude achieved by heating experiments over modulation frequency which is reproduced in Fig. 1.17. It clearly shows the increase in magnetic response at lower modulation frequencies.

Theoretical considerations show that the modulated current will launch fast and Alfvén waves into the magnetosphere (Fejer and Krenzien, 1982; Borisov and Stubbe, 1997). The Alfvén mode is, regarding the small dimensions of the source and the wave's propagation along the magnetic field lines, far more important then the fast mode. Robinson et al. (2000) provided strong evidence that artificially generated Alfvén waves at 3 Hz were registered by satellite borne magnetic instruments above

the heating facility at Tromsø, Norway.

Heating experiments on closed field lines can be expected to show a larger response if the modulation frequency is chosen such that it matches the local eigenfrequency of the field line. Determining the local eigenfrequency is not a trivial task, as it changes due to time of day, solar activity and other parameters such as mass loading along the field line.

On open field lines however, when one end of the field line is essentially unbound, modulated heating at virtually any frequency will produce wave activity given the right ionospheric conditions.

When trying to induce ULF wave activity using modulated heating, the principal and unavoidable problem of presenting proof for having successfully altered the ionospheric conditions by analysing ground-based magnetic field data is that the oscillations observed could have had a natural origin. Careful analysis of prevailing solar wind conditions and ground-based magnetic measurements in the vicinity of the heating facility is imperative to eliminate this problem as much as possible.

2 Instrumentation and Data Analysis Techniques

The first part of this chapter introduces the instruments which provided the data analysed in this thesis. Data analysis techniques which were used heavily in this work are presented in the second part.

2.1 Instrumentation

2.1.1 Fluxgate Magnetometers

A fluxgate magnetometer is a device to measure magnetic fields. It consists of three essential parts: a core made from a highly magnetically permeable alloy, a driving (primary) coil and a sensing (secondary) coil. Fig. 2.1 shows a schematic of a fluxgate magnetometer.

In modern designs the ferromagnetic core is usually a ring around which the driving coil is wound. An alternating current through the primary coil drives the core into magnetic saturation. In the case of no background magnetic field, the two half cores (shown in blue and green in Fig. 2.1) go into and come out of saturation at exactly the same time. Hence no voltage is induced in the secondary winding.

If, however, a background magnetic field with a component in the direction of the magnetisation within the core exists as depicted by the light blue arrow in Fig. 2.1, one half core will reach saturation earlier than the other during the first half of the driving cycle. This asymmetry causes a voltage to be induced into the sensing coil, the amplitude of which is proportional to the background magnetic field.

Using three cores in a triaxial setup, all three components of the magnetic background field can be measured.

Fluxgate magnetometers are one of the preferred designs for measuring magnetic fields in space plasma physics as they show no drift with time, are relatively cheap,

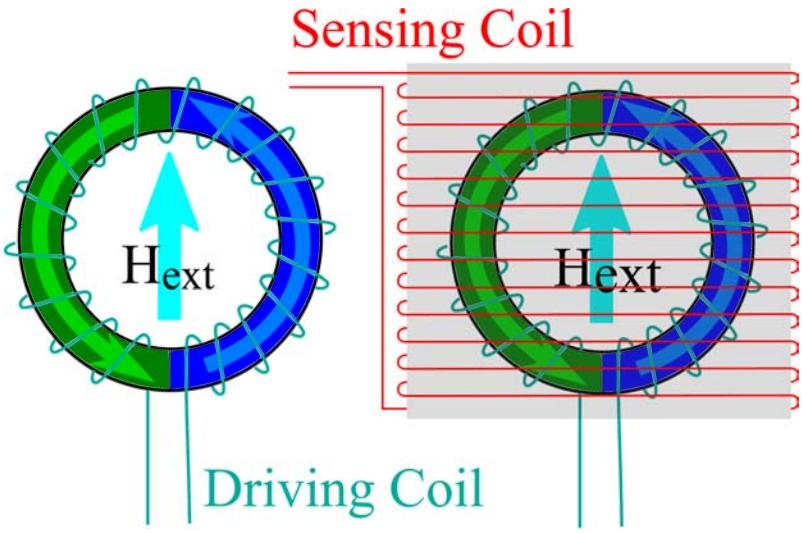

Figure 2.1: Schematic of a fluxgate magnetometer.

operate on low powers and are light-weight.

2.1.2 The Space Exploration by Active Radar Facility

The Space Plasma Exploration by Active Radar (SPEAR) has been operational since late 2004. It was designed and built at the Radio and Plasma Physics Group of Leicester University and is described in Wright et al. (2000) and Robinson et al. (2006). It was erected near Longyearbyen, Svalbard (78°9′N 16°4′E) and consists of currently 24 broadened crossed dipole antennas which are grouped to form a 6×4 array. The layout and orientation of the antennas is shown in Fig. 2.2.

SPEAR can be operated in four very different modes:

1. Generation of field-aligned irregularities
2. Field guided ELF wave injection
3. Stimulation of ULF waves
4. ”All-Sky” radar capabilities

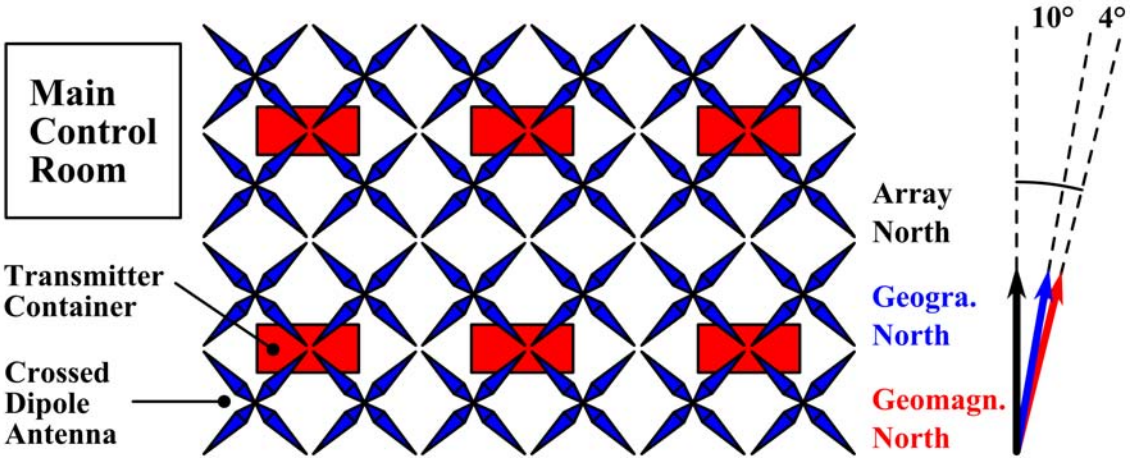

Figure 2.2: Layout and orientation of SPEAR (adapted from Robinson et al. (2006)).

So far, results using the first and second mode have been published (Robinson et al., 2006; Scoffield et al., 2006) while operation in the fourth mode is ongoing. In Cha. 3 we present first results of operations in the third mode.

The first three objectives are achieved by pumping electromagnetic waves into the ionosphere. SPEAR generates waves at frequencies between 4 and 6 MHz and has an effective radiated power of 28 MW. By adjusting the phase difference of the signal to the two antennas of each crossed dipole, the emitted wave can be circularly polarised (X mode) or linearly polarised (O mode). Whereas O mode polarisation is used to generate field aligned density irregularities off which the signals of coherent radars scatter (Robinson et al., 2006), the X mode polarisation is used for the stimulation of ELF und ULF waves. The details of this mechanism are described in Sec. 1.2.7.

The SPEAR system is currently the only ionospheric heating facility which is routinely located inside the northern polar cap and thus frequently operates on open field lines.

2.1.3 The Svalbard Ionosonde

To monitor ionospheric conditions in the vicinity, an ionosonde is co-located with the SPEAR facility. It emits electromagnetic pulses sweeping through 100 logarithmically spaced frequencies between 1.4 and 14 MHz. For each frequency it then records the amplitude of the returned signal and the associated lag time from emission. The amplitude during one lag time when no echo of the emitted pulse can be expected is used as the background noise level.

The ionospheric reflection process is strongly dispersive due to the strong variation of the electron density with altitude (see Sec. 1.1.5). Hence an ionogram, i.e. a plot of the reflected signal's amplitude for each emitted frequency against lag time provides information about the ionospheric electron density distribution.

The conversion from lag time to actual reflection altitude is not trivial. In this study the actual reflection height is not of importance and all data are plotted against the so-called "virtual height". This altitude is simply calculated by multiplying half the lag time with the speed of light.

2.1.4 The Barentsburg Doppler Sounder

Variations of the ionospheric refractive index μ_R occur on a wide range of time scales, from several seconds due to hydromagnetic waves down to several hours caused by tidal effects. If a high-frequency (HF) signal with a frequency f traverses a region of changing μ_R, the phase path P of that signal is changed. This, in turn, imposes a frequency shift Δf

$$\Delta f = -\frac{1}{\lambda}\frac{dP}{dt} \tag{2.1}$$

where λ is the wavelength of the HF signal (Wright, 1996). The Doppler sounding technique measures this frequency shift Δf.

The heart of a Doppler sounder is a highly stable frequency generator. The output signal of the generator is split, one part is emitted, usually vertically, into the ionosphere whereas the second part is kept for reference. The reference continuous wave signal is then mixed with the signal reflected off the ionosphere, the so-called sky wave. To find a value for the Doppler shift of the sky wave, a dynamic spectrum of the mixed signal is produced by applying a FFT and subsequent normalisation. Successful Doppler sounding of the ionosphere was first reported by Watts and Davies (1960).

A Doppler sounder is located in Barentsburg, some 50 km west of SPEAR. The data from that sounder presented in Cha. 3 was obtained using a slightly different setup than that described above. Instead of emitting its own signal, the sounder in Barentsburg was tuned to the SPEAR pump frequency and receiving only. The presented Doppler shift is hence that of the signal emitted by SPEAR and received in Barentsburg.

2.1.5 The Cluster Mission

The Cluster mission (Escoubet et al., 2001) consists of four spacecraft carrying identical scientific payloads. They orbit the Earth in a polar elliptical fashion with an apogee of about 20 R_e and a perigee of about 4 R_e. The orbital period is 57 hours and each spacecraft fulfils one spin in approximately 4 s.

As the orbit is fixed in inertial space, the orbital plane rotates with respect to the Sun-Earth line and hence different regions of the magnetosphere are observed during different seasons. Fig. 2.3 illustrates this feature of the orbital motion.

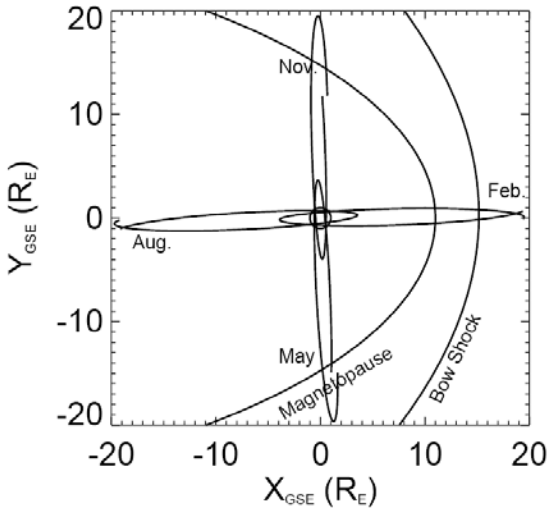

Figure 2.3: Orbits of the Cluster spacecraft projected onto the equatorial plane. The orbits are shown at three-month intervals, starting with the 2nd launch in August 2000 (taken from Escoubet et al., 2001).

Measurements from four identical spacecraft offer, for the first time, the opportunity to study plasma structures in three dimensions. That is true for spatial changes that are larger than the average separation between the spacecraft. In order to sample different plasma regimes, the separation of the four spacecraft has been changed over the course of the mission from just a few 100 km to well over 10,000 km.

The Cluster mission allows the computation of 3D parameters which are not available to missions with fewer spacecraft, like the curl of the magnetic field (Dunlop et al., 2002) or all three components of a wave vector (Glassmeier et al., 2001). Such calculations yield best results whenever the constellation of the spacecraft is closest to tetrahedral. The orbit of the Cluster mission is such that the spacecraft generally form a tetrahedron at apogee. Due to orbital dynamics the formation is more like pearls on a string at perigee.

The Fluxgate Magnetometer

The FGM onboard the Cluster mission is described in detail in Balogh et al. (2001). The primary sensor is located on a 5 m long boom stretching from the spacecraft body. The background magnetic field is sampled at approximately 202 vectors/s, however in all studies here which include FGM measurements, the data have been downsampled to spin resolution, i.e. one vector every 4 s.

The Electric Fields and Waves Experiment

The EFW experiment consists of four spheres on the ends of 50 m long booms in the spin plane of the spacecraft (Gustafsson et al., 2001). The potential difference between two probes on opposite sides of the spacecraft provides the average electric field in the direction of the boom. Two orthogonal booms with two probes each allow for the measurement of the quasi-static electric field vector in the spin plane of the spacecraft which is essentially aligned with the X-Y GSE plane. With the help of magnetic field data provided by the FGM, the third component of the electric field along the spin axis can be calculated from the frozen flux assumption (1.21). It then follows that the electric and magnetic field ought to be orthogonal, i.e. $\vec{E} \cdot \vec{B} = 0$ which yields

$$E_z = -(E_x B_x + E_y B_y)/B_z. \tag{2.2}$$

(2.2) will not produce sensible results whenever the magnetic field vector is close to the spacecraft spin plane, i.e. $B_z \to 0$. Electric field values were therefore treated as missing data whenever the angle between the magnetic field and the spin plane was smaller than 5°.

If data from the EFW is presented in a mean-field aligned coordinate system (see Sec. 2.2.2), the electric field in the field-aligned direction is identical zero. This follows directly from the condition $\vec{E} \cdot \vec{B} = 0$ used to complete the 3D electric field.

In normal telemetry mode the EFW is capable of providing 25 vectors/s of the electric field in the spin plane low-pass filtered at 10 Hz. Here only data downsampled to spin resolution are used.

The Wave of High Frequency and Sounder for Probing of Electron Density by Relaxation Experiment

The WHISPER experiment onboard Cluster has an active and a passive mode of operation. In the passive mode the naturally occurring plasma emissions between 2 and 80 kHz are recorded. In the active mode a short sinusoidal wave train with a central frequency stepping through the frequency range of 4 to 80 Hz is emitted by the instrument. The echo of the surrounding medium is then recorded as well as a background signal shortly before the transmission of each pulse.

A model plasma frequency can be fitted to every such obtained spectrum observed by the WHISPER experiment, hence allowing the determination of the electron density (Trotignon et al., 2001). Electron densities provided by the WHISPER instrument are linked to a quality flag. This flag is set to a value between 0 and 100 according to the confidence of fit of the model plasma frequency to the measured spectrum.

2.1.6 Ground-Based Magnetometer Chains

All ground-based magnetometer data presented in this work are from one of the chains introduced in the following sections. All magnetometers are fluxgate con-

structions with an accuracy of 0.1 nT but significantly different sampling intervals. The three fluxgate sensors are orientated in such a way that the magnetic field is measured in a (X,Y,Z) coordinate system where X is in geographic North-South direction (positive North), Y in East-West direction (positive East) and Z up-down (positive down).

IMAGE

The International Monitor for Auroral Geomagnetic Effects (IMAGE) array consists of 31 fluxgate magnetometers scattered over Northern Europe, Scandinavia, Russia and Svalbard (Lühr, 1994). These stations span magnetic latitudes from 50° to 75° at magnetic longitudes between 70° and 120°. Fig. 2.4 shows the location of the subset of stations used in this work. The sampling interval for IMAGE magnetometers is 10 s.

CARISMA

As of January 2008 the Canadian Array for Realtime Investigations of Magnetic Activity (CARISMA) array is made up out of 15 fluxgate magnetometers located in Canada (see Fig. 2.5). The CARISMA array spans magnetic latitudes from 60° to 80° and magnetic longitudes from 270° to 330°. Of special importance for pulsation studies is the so-called Churchill-line, a set of seven magnetometers located at essentially one magnetic longitude but covering magnetic latitudes between 78° and 60°. The sampling interval was 5 s before March 2005 and 1 s thereafter.

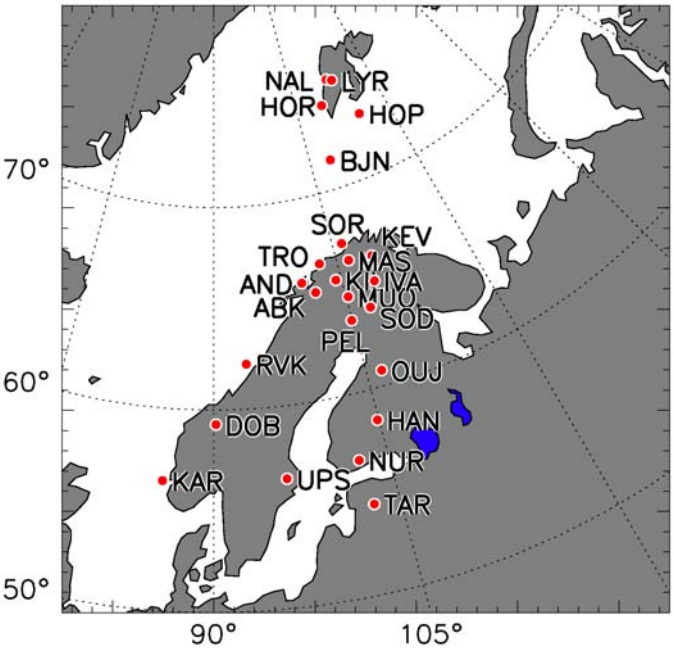

Figure 2.4: Locations of some ground-based magnetometers belonging to the IMAGE chain in geomagnetic coordinates.

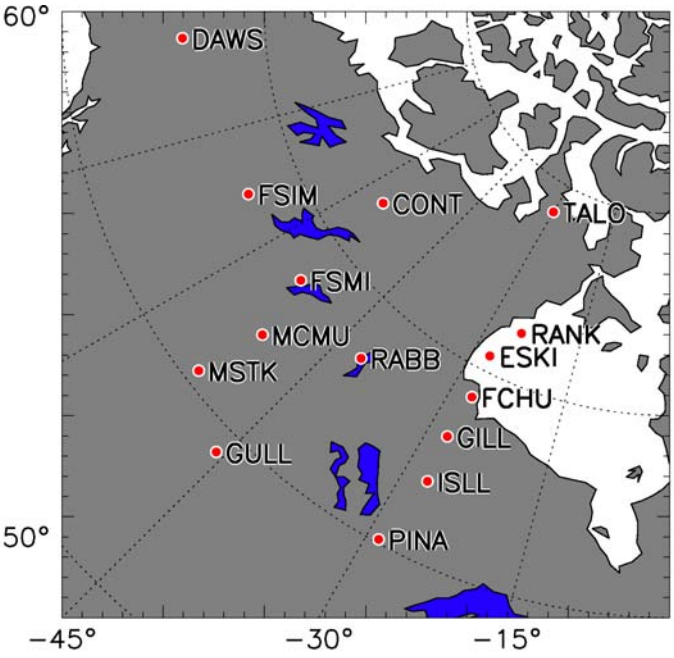

Figure 2.5: Locations of ground-based magnetometers belonging to the CARISMA chain in geomagnetic coordinates.

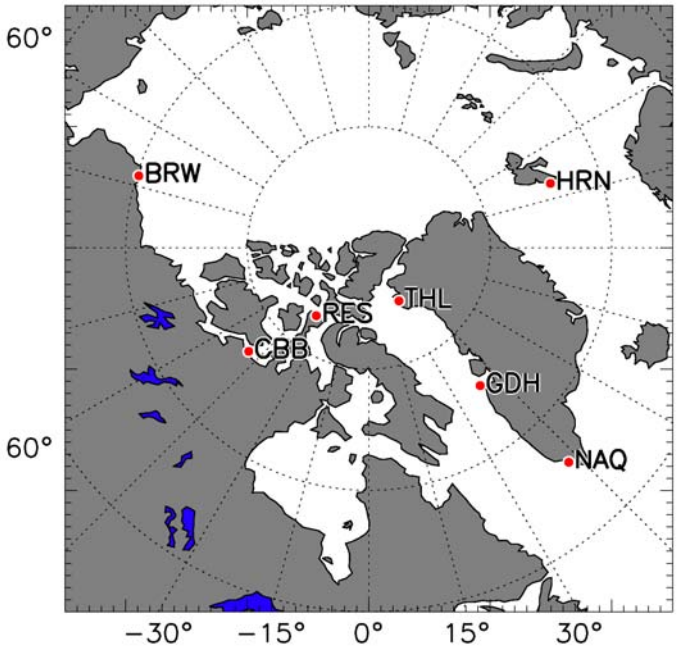

Figure 2.6: Locations of some ground-based magnetometers belonging to the INTERMAGNET chain in geomagnetic coordinates.

INTERMAGNET

Over 90 magnetometer stations spread over all continents form the International Real-time Magnetic Observatory Network (INTERMAGNET). Of these stations only a small subset was used in this study as shown in Fig. 2.6. Due to bandwidth limitations the sampling period is one minute.

MACCS

The Augsburg College operates 13 magnetometers in cooperation with Boston University and the Geomagnetism Unit of the Geological Survey of Canada called the Magnetometer Array for Cusp and Cleft Studies (MACCS) which is described in detail in Engebretson et al. (1995). The stations are located in North-East America and Canada (see Fig. 2.7). The sampling time of the data used in this work is 5

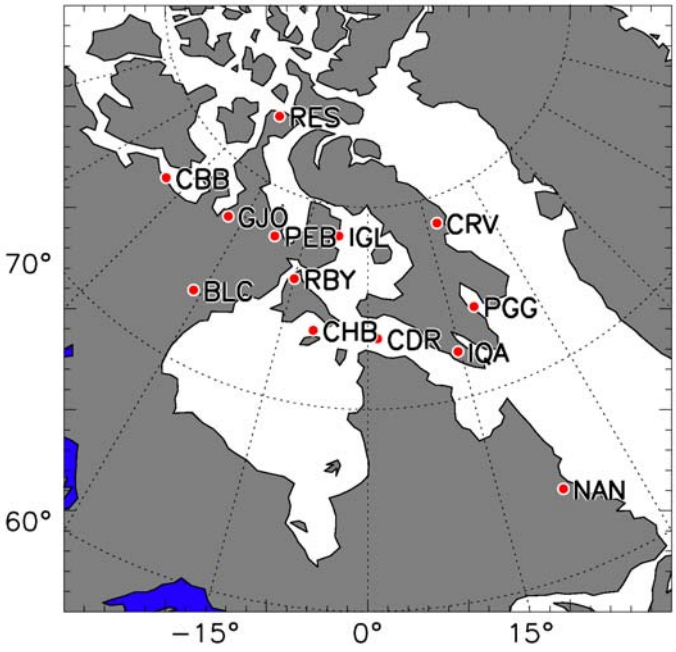

Figure 2.7: Locations of ground-based magnetometers belonging to the MACCS chain in geomagnetic coordinates.

seconds.

SAMNET

The SAMNET magnetometer array consists of 5 magnetometers operated by the University of Lancaster, five stations belonging to the IMAGE array and three stations operated by the British Geological Survey. All magnetometers are operated with a sampling period of 1 s. The locations of the 13 stations are shown in Fig. 2.8.

2.1.7 The ACE Satellite

Located in a halo orbit around the so-called L1 point, the Advanced Composition Explorer (ACE) has now been measuring essential plasma parameters inside the

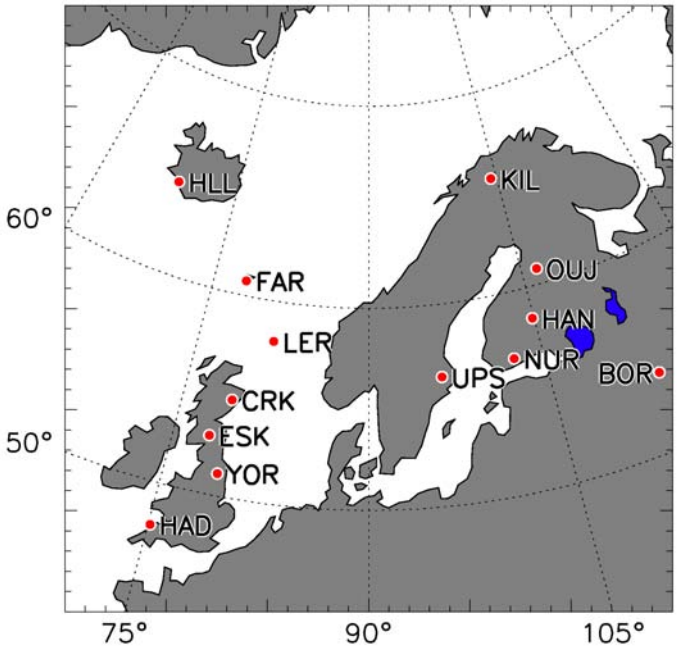

Figure 2.8: Locations of ground-based magnetometers belonging to the SAMNET chain in geomagnetic coordinates.

solar wind for over ten years (Stone et al., 1998).

From the nine instruments that are mounted onboard ACE only two will be of interest here. Firstly, the Solar Wind Electron, Proton, and Alpha Monitor (SWEPAM) that is designed to measure the three-dimensional characteristics of solar wind and suprathermal electrons from about 1 to 900 eV and ions from 0.26 to 35 keV (McComas et al., 1998). It provides critical parameters of the solar wind such as the solar wind velocity and the ion density at a sampling period of 64 s.

Secondly, the magnetometer (MAG) is a twin triaxial fluxgate magnetometer that measures the direction and magnitude of the IMF (Smith et al., 1998). MAG is a flight spare of the magnetometer instrument flown on Wind and has a time resolution of 1 vector every 16 seconds.

2.1.8 The Geotail Satellite

The Geotail satellite is a joint programme of the Institute of Space and Astronautical Science (ISAS) of Japan and NASA of U.S.A. It was launched in July 1992 and is described in Nishida (1994). After an initial orbit phase it is now in an elliptical orbit around the Earth with a perigee of about 10 R_e and an apogee of about 30 R_e. Because of this configuration it spends the apogee for half a year in the Earth's magnetic tail while the other half year is spent in the solar wind.

The magnetic field instrument (MGF) is mounted on two booms each with a length of 6 m (Kokubun et al., 1994). It provides all three components of the background magnetic field at a resolution of 1 vector every 3 seconds.

2.1.9 The DMSP Satellites

The Defense Meteorological Satellite Program (DMSP) has provided the US Department of Defense with data for use in weather forecasting since first DMSP spacecraft was launched in January 1965. The spacecraft are in near-polar and circular orbits at an altitude of 835 to 850 km. In addition later spacecraft began to include particle and fields detectors which provide data about the space environment.

The particle sensor mounted on DMSP 13 and 15 used here is the monitor of precipitating ions and electrons with energies between 30 eV and 30 keV, built by USAF Research Lab, Space Vehicles Directorate.

2.2 Data Analysis Techniques

2.2.1 The Cross-phase Technique

As described in Sec. 1.2, standing waves do form on terrestrial magnetic field lines. The fundamental eigenfrequency of a certain field line is dependent on its length but also on how the mass is distributed along the field line. The mass distribution changes with geomagnetic activity and L-value, the length of a field line can only be obtained by models, hence an accurate estimate of the fundamental eigenfrequency of field lines based on these parameters is difficult.

However, using data from ground-based magnetometer data, one can estimate the eigenfrequencies of a field line (Kurchashov et al., 1987; Waters et al., 1991). For this method the cross-phase of the data from two adjacent magnetometer stations at similar longitudes but different latitudes is calculated. Two assumptions have to be made to allow for an accurate estimation. Firstly it is assumed that quasi-random variations at eigenfrequencies of the field line are always present in the data. Secondly, the natural frequency of the poleward station is, mainly due to the longer field line, slightly lower than that of the equatorward station.

Fig. 2.9 delineates this situation for the southern hemisphere. The amplitude over pulsation frequency is shown in the top panel. The equatorward magnetometer is located on a shorter field line and has therefore the slightly higher eigenfrequency ω_N than that of the poleward station ω_S. The phase shift across the amplitude peak as predicted by theory is shown in the second panel (compare also Fig. 1.11).

An earlier estimation of the eigenfrequency Ω of the field line located half way between those connected to the magnetometer stations is based on the amplitude difference of the two spectra as shown in the third panel of Fig. 2.9 (Baransky et al.,

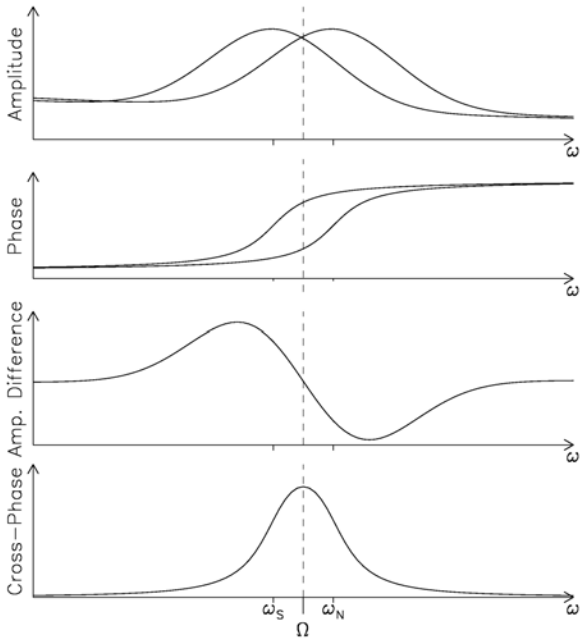

Figure 2.9: Schematic illustrating the cross-phase technique (adapted from Waters et al., 1991).

1985). Ω is found by estimating the frequency at which the sign of the amplitude difference changes.

Although the method based on amplitude differences works in theory, application of that algorithm to real data proved difficult and yielded ambiguous results. Waters et al. (1991) found that an estimation is much more reliable when basing it on the cross-phase of the two signals. The eigenfrequency Ω is then that frequency, at which the cross-phase spectrum reaches its maximum as shown in the bottom panel of Fig. 2.9. Frequency estimation based on cross-phase calculations yields clearer results in contrast to the method described in Baransky et al. (1985).

The cross-phase technique does not depend on large-amplitude FLR signatures in the analysed ground-based magnetometer data. Rather, the phase relation between small-amplitude pulsations which are assumed to occur at the natural eigenfrequency is used for the frequency estimation.

2.2.2 Mean-Field Aligned Coordinate System

The mean-field aligned (MFA) coordinate system is somewhat similar to the dipole coordinate system presented in Sec. 1.2.4. However, as actual magnetic field measurements are used to establish the directions of the MFA coordinate system, a more realistic representation of the background magnetic field is obtained.

There are two aims when transforming magnetic field data from satellites into the MFA coordinate system. The first is to separate perturbations from the background field and the second is to obtain information about the polarisation of any observed perturbation.

In the MFA coordinate system the magnitude B_0 and direction of the background field $\vec{\hat{\mu}}$ is calculated by averaging over a certain number of magnetic field measurements.

The positive direction of the $\vec{\hat{\mu}}$ component in the MFA system is parallel to the background magnetic field. The vector product of the satellite's geocentric position $\vec{r}$ and the field-aligned direction gives the azimuthal direction as $\vec{\hat{\phi}} = \vec{\hat{\mu}} \times \vec{r}$. The azimuthal axis points eastward. The radial component $\vec{\hat{\nu}}$ then completes this right handed coordinate system as $\vec{\hat{\nu}} = \vec{\hat{\mu}} \times \vec{\hat{\phi}}$. The radial axis points towards the centre of curvature.

After the data have been transformed into the MFA system, the average field magnitude B_0 determined to find the background field direction $\vec{\hat{\mu}}$ is subtracted from the field aligned component. This acts as a high-pass filter, such that the number of points over which the average is calculated has to be chosen according to the frequency range of the perturbations one wishes to study.

The advantage of the MFA coordinate system is that the component in which an oscillation is observed will identify its wave mode. Compressional modes are

observed in the field-aligned magnetic field as described in Sec. 1.2.2. Oscillations in the azimuthal magnetic and radial electric component are toroidal Alfvénic modes whereas poloidal Alfvénic modes are observed in the radial magnetic and azimuthal electric field (see Sec. 1.2.4).

3 Artificially Generated ULF Waves

published as

First results of a ULF wave injected on open field lines by SPEAR, *JGR,* 113, 1305-1315, **2008**

3.1 Introduction

This thesis is concerned with ultra-low frequency (ULF) waves in the Earth's magnetosphere. In the following three chapters only a few aspects of this vast area of ongoing research are highlighted. First, an episode during which ULF waves were artificially generated by ionospheric heating is described in detail. The following two chapters are somewhat more related, as they both deal with the interaction of the magnetospheric plasma and the Earth's magnetic field with waves generated outside of the magnetospheric cavity.

In this chapter we present strong evidence that on 23 February 2007 between 2230 and 2330 UT the SPEAR system (see Sec. 2.1.2) successfully modified the ionospheric electron density inside the northern polar cap. The modulated modification led to the generation of a small scale ULF wave on open field lines which was detected by ground-based magnetometers in the vicinity of the radar. It was not registered by magnetometer stations located elsewhere inside the northern polar cap or at lower latitudes. The solar wind conditions are investigated and although wave activity at the modulation frequency is present, it is shown that the local ULF wave is unlikely to originate from that activity.

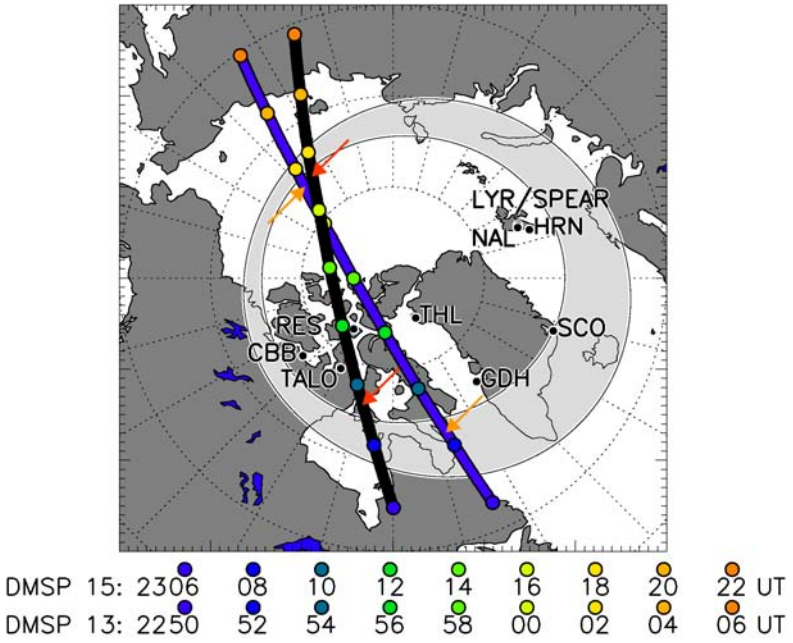

Figure 3.1: Positions of magnetometer stations in the northern hemisphere on 23 February 2007, in geomagnetic latitude and longitude coordinates. The auroral oval is indicated for $Kp = 1$ in grey. The black and blue traces follow the footprint of the DMSP 13 and 15 satellite, respectively. See text for further details.

3.2 Observations and Discussion

Between 2230 and 2330 UT on 23 February 2007 the SPEAR system was operated at 4.45 MHz with a superimposed 1 Hz modulation in X mode polarisation. Additionally, the heater was operated in a five minute on, five minute off cycle, which corresponds to a modulation frequency $f = 1.67$ mHz. The X mode polarisation was used to generate local enhancements in the electron temperature T_e in the lower ionosphere above the heating facility as described in Sec. 1.2.7 and 2.1.2.

The higher frequency modulation at 1 Hz was employed simultaneously in order to stimulate the Ionospheric Alfvénic Resonator (IAR), results of which will not be discussed here. Theory of this resonant interaction and some results can be found in Scoffield et al. (2006, and references therein). Instead, the results of the 1.67 mHz

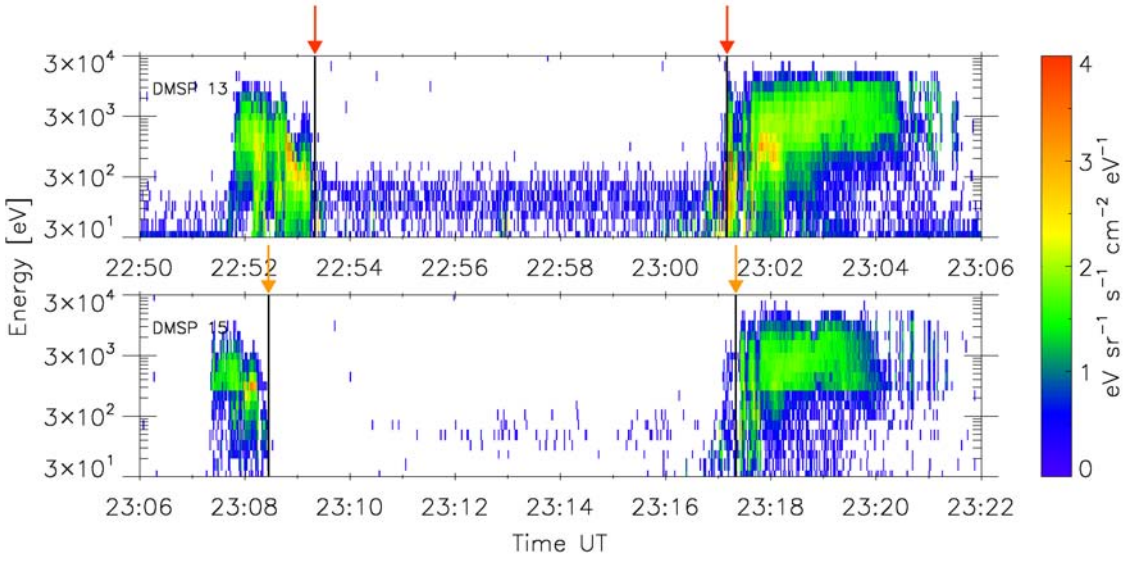

Figure 3.2: The top and bottom panel show the electron spectra measured by the DMSP 13 and 15 satellite, respectively. The footprints of the satellites are shown in Fig. 3.1. Arrows above the spectra mark the crossing of the poleward OCB boundary as determined by eye.

modulation will be reported. The period of the lower frequency on/off cycle was long enough to allow for changes in the recombination rate to occur and thus an affect on the local electron density was expected.

Fig. 3.1 gives an overview of the positions of ground-based magnetometers and the SPEAR facility in geomagnetic coordinates. Also plotted is the position of the auroral oval according to the model by Holzworth and Meng (1975) at 2300 UT. The model input parameter is $Kp = 1$ which is the value extracted from The International Service of Geomagnetic Indices (ISGI) at `http://isgi.cetp.ipsl.fr/` for 23 February 2007.

The poleward boundary of the auroral oval can be used as a proxy for the Open/Closed Field Line Boundary (OCB). Hence Fig. 3.1 shows that SPEAR and all magnetometers located on the Svalbard archipelago (NAL, LYR and HRN) were most likely located on open field lines.

To further support the position of the OCB, Fig. 3.2 shows the electron spectra from the DMSP 13 and 15 satellites in the top and bottom panel, respectively. The footprint of the DMSP 13 and 15 satellites are shown as black and blue traces in Fig. 3.1.

The crossing of the poleward OCB during quiet geomagnetic times is characterised by a sharp drop in the particle flux of electrons with energies between 100 eV and 10 keV. In Fig. 3.2 the two crossings of the poleward OCB by each satellites have been determined by eye and marked by vertical black lines as well as by red and orange arrows. The times of the OCB crossings have also been marked by arrows in the footprint panels in Fig. 3.1 to give an indication for the position of the crossings with respect to the model prediction of the auroral oval for $Kp = 1$.

Although the DMSP satellites do not pass over the Svalbard archipelago, the close agreement between the DMSP observations of the OCB crossings and the model prediction of the poleward boundary of the auroral oval give credence to the latter and hence it can be assumed with confidence that the magnetometers in Ny Ålesund (NAL), Longyearbyen (LYR) and Hornsund (HRN) as well as the SPEAR facility were located on open field lines during the interval discussed.

3.2.1 Ionospheric Conditions

To monitor ionospheric conditions, an ionosonde is situated next to the SPEAR facility which records an ionogram every four minutes. Fig. 3.3 shows the recorded ionograms before, during and after the time of the experiment. Since SPEAR operation saturates the ionosonde receiver, only ionograms whenever SPEAR was off are shown.

The ionosonde observations can be divided in three sections. The first was char-

acterised by a small but visible E-region and reflected powers above 10 dB, lasting until about 2210 UT. The second interval between 2210 and 2310 UT shows lower reflected powers around 4 dB. During this time the F-region trace also widened, indicating multiple off-zenith reflections of the ionosonde signal. The E-region disappeared during this time. Finally, after 2310 UT the F-region was widening further in frequency and reflected powers increased significantly.

Low reflected powers during the second interval indicate significant absorption of the ionosonde signal in the lower ionosphere, as required for electrojet modification experiments. The value of foF2 was below the SPEAR pump frequency as indicated by the vertical dashed line, thus the signal at least partially penetrated the ionosphere.

In Fig. 3.4 data from a Doppler sounder located in Barentsburg some 50 km away from the SPEAR facility are shown (see Sec. 2.1.4). The top panel shows the Doppler shift of the received signal and their associated power. Only those parts of the spectrum whose amplitudes were greater than half the maximum power in each normalised spectrum are plotted. The amplitude of the received signal is shown in the bottom panel. Grey rectangles mark "SPEAR-on" times.

After 2305 UT the interpretation of the data is straight forward. Clearly, the signal arriving at the sounder in Barentsburg was reflected off the ionosphere, as can be seen from the large Doppler shift imposed on the signal. The signal amplitudes as shown in the bottom panel increased with time, indicating less absorption of the SPEAR pump wave in the ionosphere.

Furthermore, a periodic variation of the Doppler shift with a similar frequency as the modulation frequency is visible. The Doppler shift periodically reaches a minimum during the last two "SPEAR-on" cycles. Such periodicity suggests that

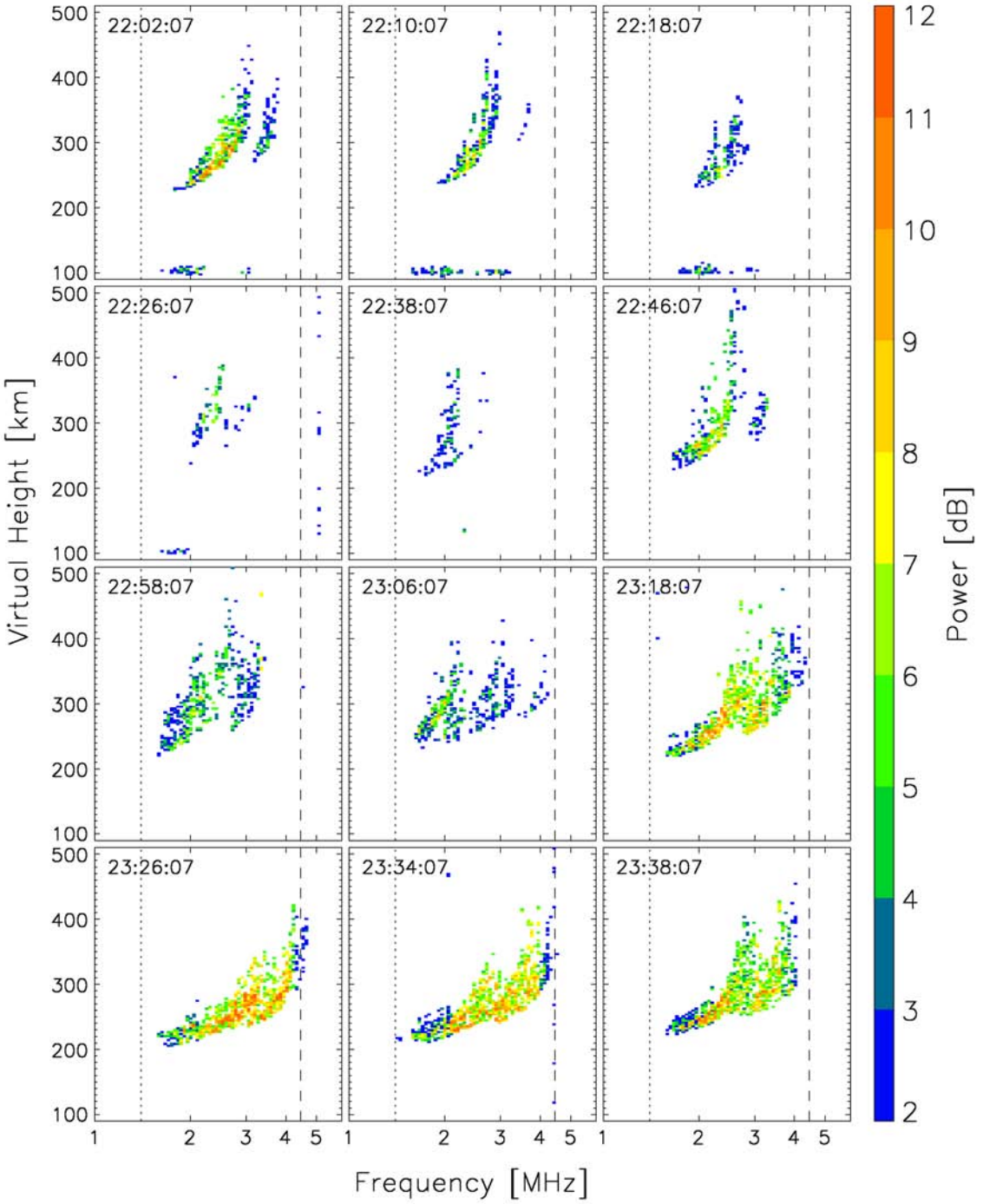

Figure 3.3: Ionograms measured by the ionosonde next to the SPEAR facility. The right vertical dashed line at 4.45 MHz indicates the SPEAR pump frequency, the left line indicates the lowest sampling frequency of the ionosonde. The time of measurement in UT is given in the top left corner of each plot.

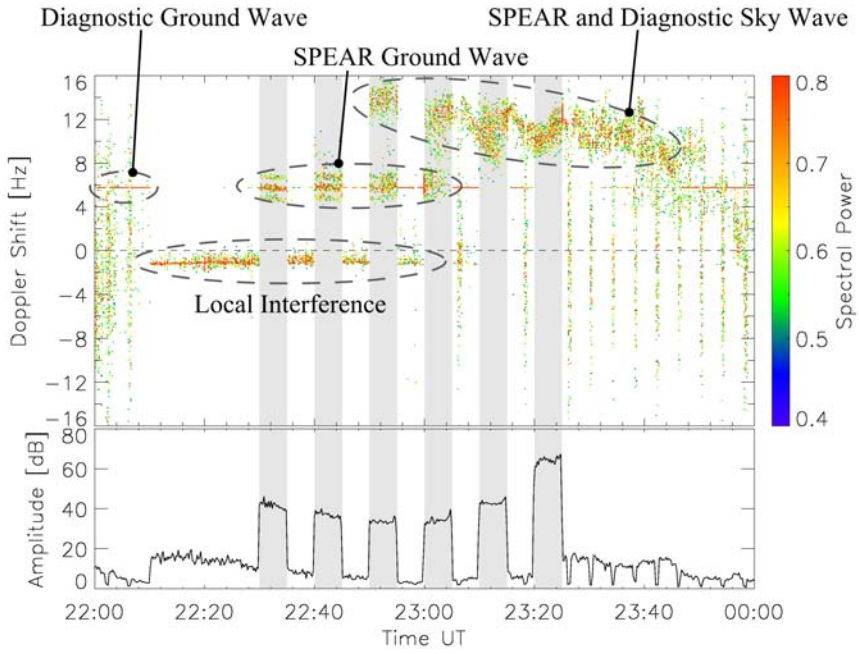

Figure 3.4: The top and bottom panel show the Doppler shift and the amplitude of the signal-to-noise ratio measured by a Doppler sounder located in Barentsburg, some 50 km from the SPEAR facility.

these variations are due to wave activity stimulated by the modulated ionospheric heating.

The fact that a signal was received during "SPEAR-off" times was due to a low power diagnostic located in the vicinity of SPEAR, also operating at 4.45 MHz. Its signal contributed two features to the Doppler spectrum. Firstly, during "SPEAR-off" times its signal was Doppler shifted to values above 8 Hz, indicating the same reflected propagation path as that of the SPEAR pump wave. Secondly, power from the diagnostic was received in Barentsburg via the ground path, resulting in a steady line just below 6 Hz. Due to the relative nature of the spectral powers and dynamic range adjustments of the receiver its signal is sometimes obscured by higher powers at other Doppler shifts.

After 2300 UT short intervals of noisy spectra can be seen every four minutes

which correspond to times when the diagnostic was turned off to allow for undisturbed measurements by the ionosonde.

During the first two heating cycles, only the SPEAR ground wave contributed to the spectrum shown in Fig. 3.4. This is indicated by the fact that the Doppler shift was the same as the ground wave of the low power diagnostic. Additionally, side bands can be seen, shifted by 1 Hz, the modulation which was added on the SPEAR signal to excite the IAR as mentioned before. The fact that no signal was received via an ionospheric path was either due to high absorption or unsuitable ionospheric conditions. The small reflected powers received by the ionosonde (comp. Fig. 3.3) make the high absorption scenario seem somewhat more plausible.

The rather constant signal around -2 Hz was due to local interference. As SPEAR was off during this time, it could only have been due to the low power diagnostic. However, this device is scheduled automatically to turn off every 4 minutes to allow for undisturbed measurements by the ionosonde. This pattern is clearly visible after 2330 UT. However between 2210 and 2300 UT there are no clear dips in the received amplitude, indicating that this signal power is due to a transmitter that was continuously on.

3.2.2 Ground-Based Observations

Fig. 3.5 provides strong evidence that the heating experiment modified the ionospheric conductivities and subsequently induced magnetic variations.

In all panels in the left columns of Fig. 3.5, times during which the background is shaded grey are those when the ionospheric heater was on, a white background indicates the heater was off.

The top left panel again shows the SPEAR reflected power at 4.45 MHz measured

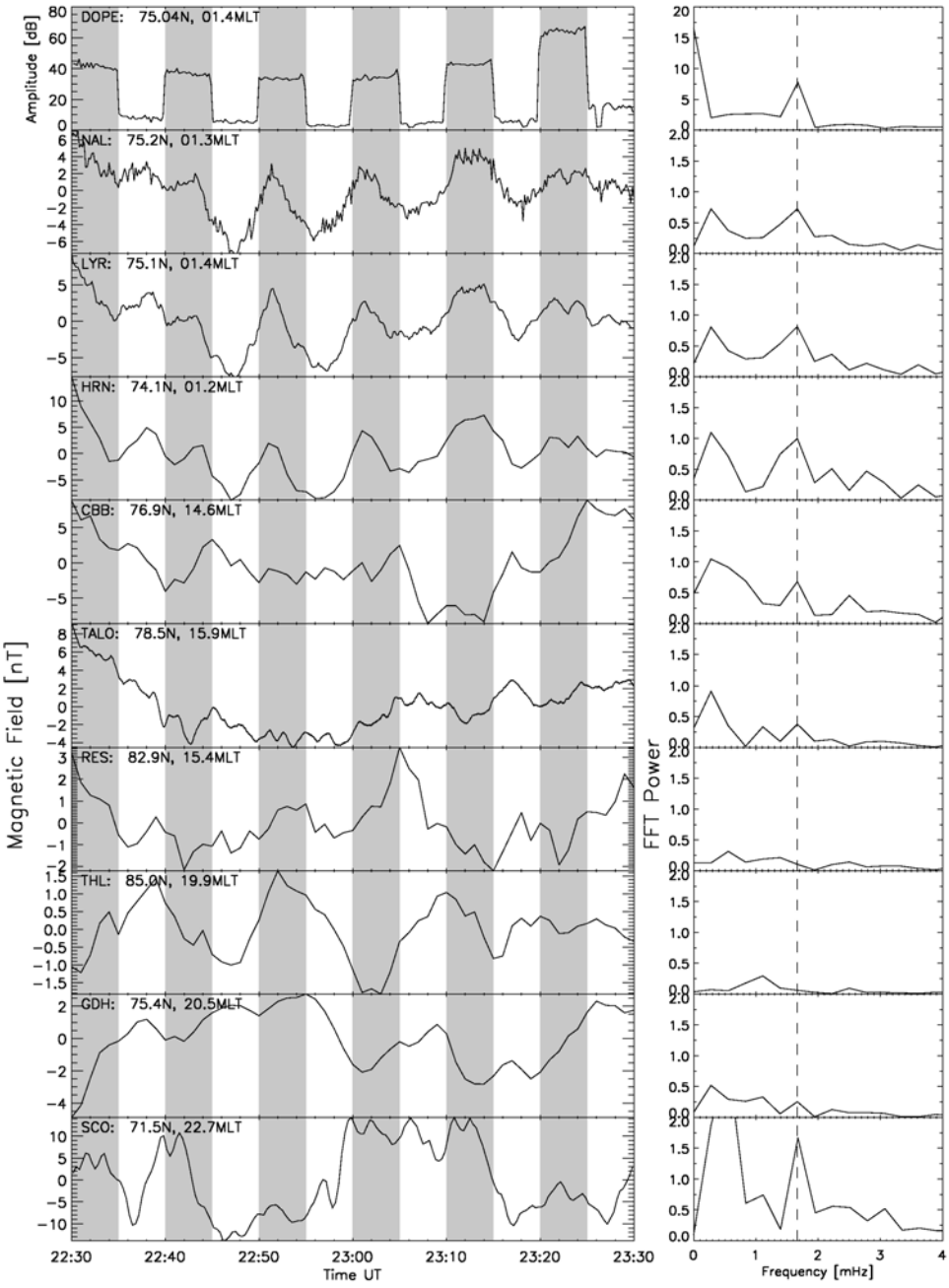

Figure 3.5: The top panels show the SPEAR reflected power measured by a Doppler sounder located in Barentsburg and its Fourier spectrum. The other panels show ground-based magnetometer data and FFTs of stations located in the northern polar cap.

by the Doppler sounder located in Barentsburg for reference. The top right panel shows the Fourier coefficients of the time series on the left. It shows, not surprisingly, a strong peak at the modulation frequency of 1.67 mHz.

The other panels in the left column in Fig. 3.5 show data from several ground-based magnetometer stations also located within the northern polar cap (see Fig. 3.1). The magnitude of the horizontal magnetic field H is shown, calculated via

$$H^2 = B_x^2 + B_y^2, \tag{3.1}$$

where B_x and B_y represent the local geographic North-South and East-West component of the magnetic field, respectively. The sampling period was 10 s for NAL and LYR, 60 s for HRN, CBB, RES, THL, GDH, 20 s for SCO and 1 s for TALO.

A linear trend has been subtracted from the data, no further filtering was applied to the time series displayed in Fig. 3.5. In the right column the Fourier spectra are plotted. All time series have been downsampled such that the sampling period was 60 s prior to applying the FFT. The spectral power values were then divided by the peak power of the HRN spectrum at 1.67 mHz.

Between 2244 and 2330 a clear signal with the same frequency as the modulation was observed in data from stations located in the close vicinity of SPEAR (NAL, LYR and HRN). The main contribution to this signal is made by measurements in the B_x component. This observation is supported by a strong peak at 1.67 mHz in the Fourier spectra of these stations.

There are similar peaks in the Fourier spectra of other stations, most notably CBB, TALO, GDH and SCO. However, the respective time series showed no obvious sign of a wave form similar to that observed by the three magnetometers located on Svalbard. Only the FFT power at 1.67 mHz of SCO reaches higher values than

NAL, LYR and HRN, indicating some background wave activity during the time of the event at this station.

Dynamic Fourier power spectra in the frequency range $1.0 < f < 3.0$ mHz are shown in Fig. 3.6. Each spectrum was calculated from a moving time series of length 4000 s. The vertical black lines indicate the start and end time of the modulation experiment, the horizontal black line indicates the modulation frequency. All data have been handled as described in the discussion of Fig. 3.5.

In data from the three magnetometers located near the SPEAR system there was a clear peak in the dynamic power coincident with the time of the heating experiment. Fig. 3.6 shows that wave activity in the according frequency range was enhanced only during the time of heating.

Dynamic spectra from all other stations show no peak during the time of the experiment. The spectral power at 1.67 mHz for these stations was overall low, only in data from SCO there was enhanced power during the experiment when compared to the HRN spectra.

When taking into account the data from all stations we conclude that the natural wave activity at the modulation frequency in the polar cap during the heating experiment was low. This strengthens the interpretation of the observed wave activity at the Svalbard stations was indeed artificially induced by SPEAR.

To investigate the phase relationship between the heating cycle and oscillations seen in ground-based magnetometer data the cross-phase technique was used. Each datum in Fig. 3.7 represents the cross-phase between a moving 1000 s interval of the ground magnetometer data (as shown in Fig. 3.5) and a moving 1000 s interval of a 10 min period sine wave with zero phase. The points are spaced by 60 s. The legend indicates which line styles represent which station. The vertical dashed lines

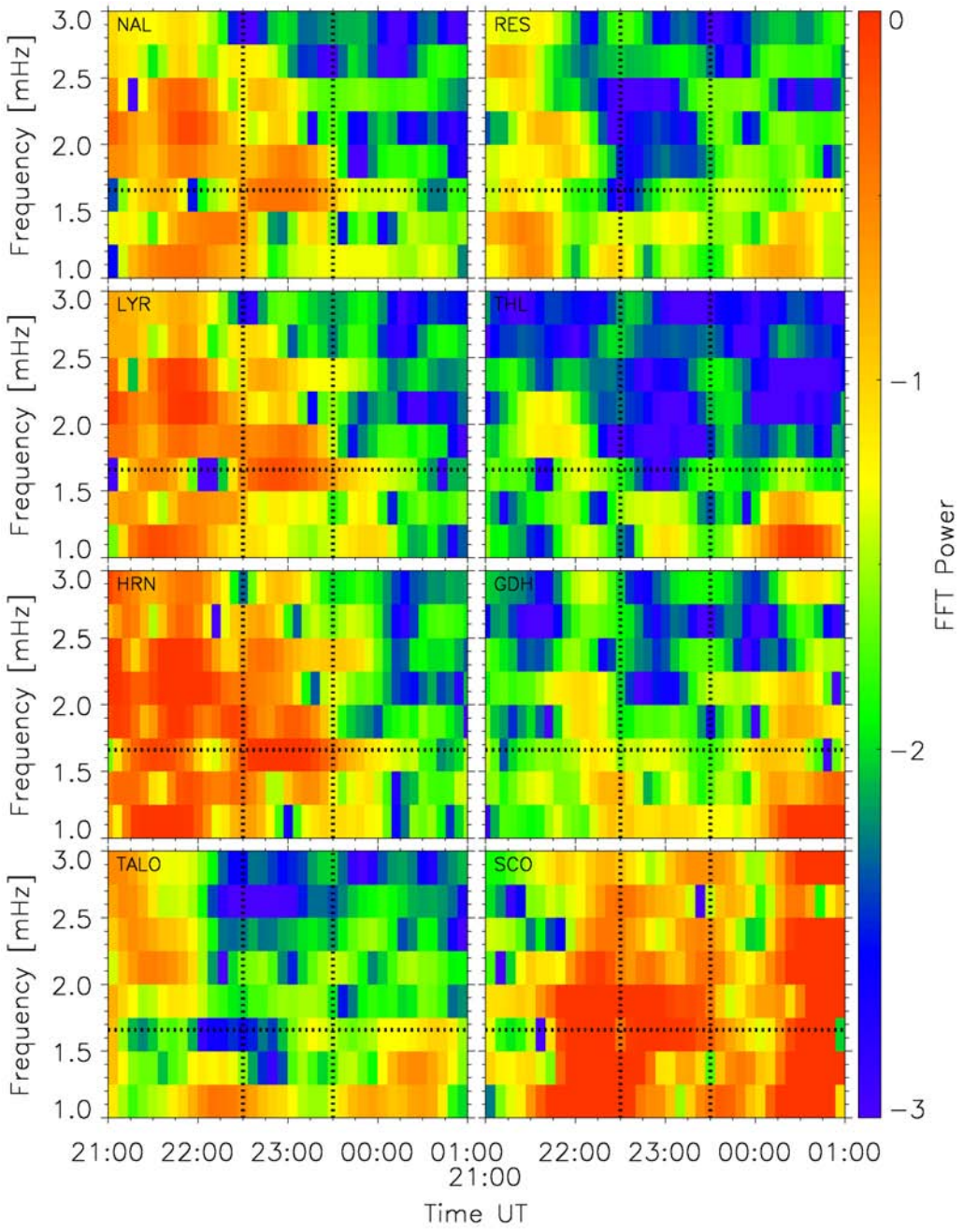

Figure 3.6: Dynamic spectra of ground-based magnetometer data.

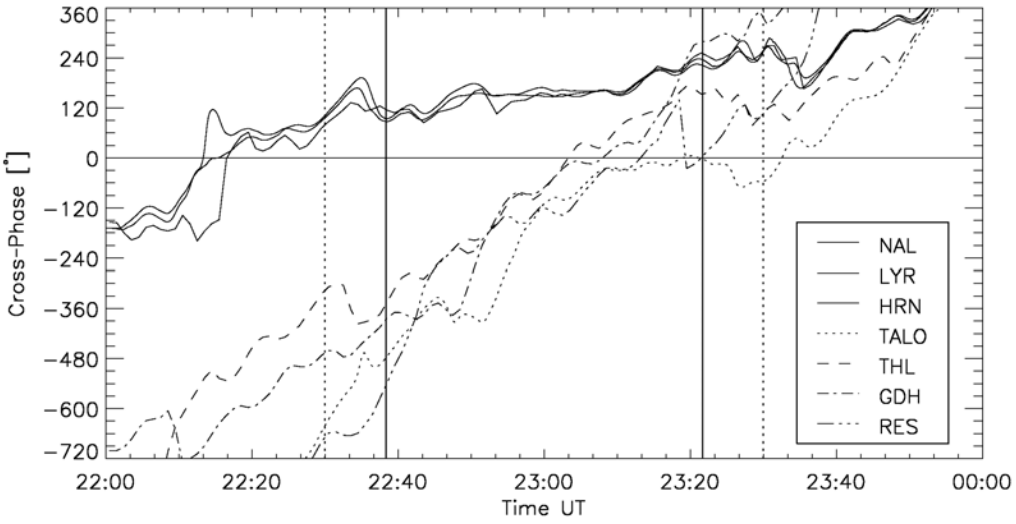

Figure 3.7: Cross-phase between a sine with a 10 min period and data from several ground-based magnetometers.

enclose the time of the modulation experiment.

Maps of the convection pattern in the northern hemisphere indicate eastward flow, i.e. westward conventional current over Svalbard during the time of the experiment. Modulating both conductivities then causes a modulation mainly in the local North-South magnetic field (B_x component), as was indeed observed.

During times of heating the electron density increases on time scales of several seconds, as mentioned in Sec. 1.2.7. Subsequently the conductivities and the westward current increase and accordingly the southward field increases. The oscillations in electron density, conductivities, current and magnetic field are all expected to be in phase. Hence any phase shift detected by the cross-phase technique between the observed magnetic field and the heating cycle highlights the time scales on which heating affects the electron densities.

If there were no delay in the dependence of the magnetic field on the heating cycle, the southward magnetic field would increase as soon as the heater is switch

on. This corresponds to a decrease in the B_x component since in the local geographic coordinate system North is positive. Hence, for the cross-phase calculation the sine wave representing the heating cycle was taken to be negative values during periods of "heater on".

Since a moving time series of the ground data was employed, only cross-phases in the interval

$$[\text{StartTime}+\text{MovingIntervalLength}/2,\ \text{EndTime}-\text{MovingIntervalLength}/2] \quad (3.2)$$

are calculated from data recorded entirely during the modulation experiment. The borders of this interval have been marked with vertical solid lines in Fig. 3.7. Hence cross-phases outside this interval have to be treated carefully since their calculation includes measurements of time before and after the heating experiment.

Fig. 3.7 shows that the phase relationship between data from the three magnetometers located on Svalbard and the sinusoidal driver remained fairly constant during the entire modulation experiment. There was no such constant phase relationship before and after the experiment. Due to the way the cross-phase was calculated, a positive value corresponds to the driver leading in phase.

The calculated cross-phase of 160° translates to a lag of the magnetometer signal by several minutes. This seems reasonable when considering the time constants of ionospheric density changes due to the heating's impact on recombination rates. However, no experimental or modelled data is available which would allow us to compare our result.

Additionally, there was no constant phase relationship between the assumed driver and data from any other station located inside the northern polar cap, as Fig. 3.7 clearly shows.

This provides strong evidence that the heating experiment modified the ionospheric conductivities and subsequently generated a local ULF pulsation on open field lines in the vicinity of the SPEAR facility.

3.2.3 Solar Wind Conditions

As mentioned in Sec. 1.2.7, the principal problem of showing that magnetic variations are due to heating experiments is the occurrence of abundant natural oscillations in similar frequency ranges. Since SPEAR was inside the polar cap during the time of the event (see Fig. 3.1), the adjacent terrestrial magnetic field was connected to and thus coupled with the IMF. Hence solar wind conditions were studied in order to exclude as far as possible the chance of the observed oscillations being of natural origin.

The IMF was measured by the MAG instrument onboard the ACE satellite which was located $\approx 150 \cdot 10^6$ km upstream of the Earth in the solar wind. The solar wind conditions were quiet during the time of the event. The solar wind speed in the X GSM direction was around 280 km/s. During the event the four Cluster satellites were located above the southern polar cap on open field lines at $\approx (0, 0, -5)$ R_e in GSM coordinates. Based on a comparison of similar distinct features in the solar wind, the lag time between measurements at the ACE and the Cluster position can be determined to be around 100 minutes.

Fig. 3.8 shows the X, Y and Z GSM component of the IMF (left column). The time window has been chosen so that it accounts for the lag time of the solar wind. In the raw data, vertical dashed lines have been plotted every ten minutes as a guide for the eye. The raw data show some indication of wave activity at the modulation frequency, but no obvious sign of a pulsation with a ten minute period was observed.

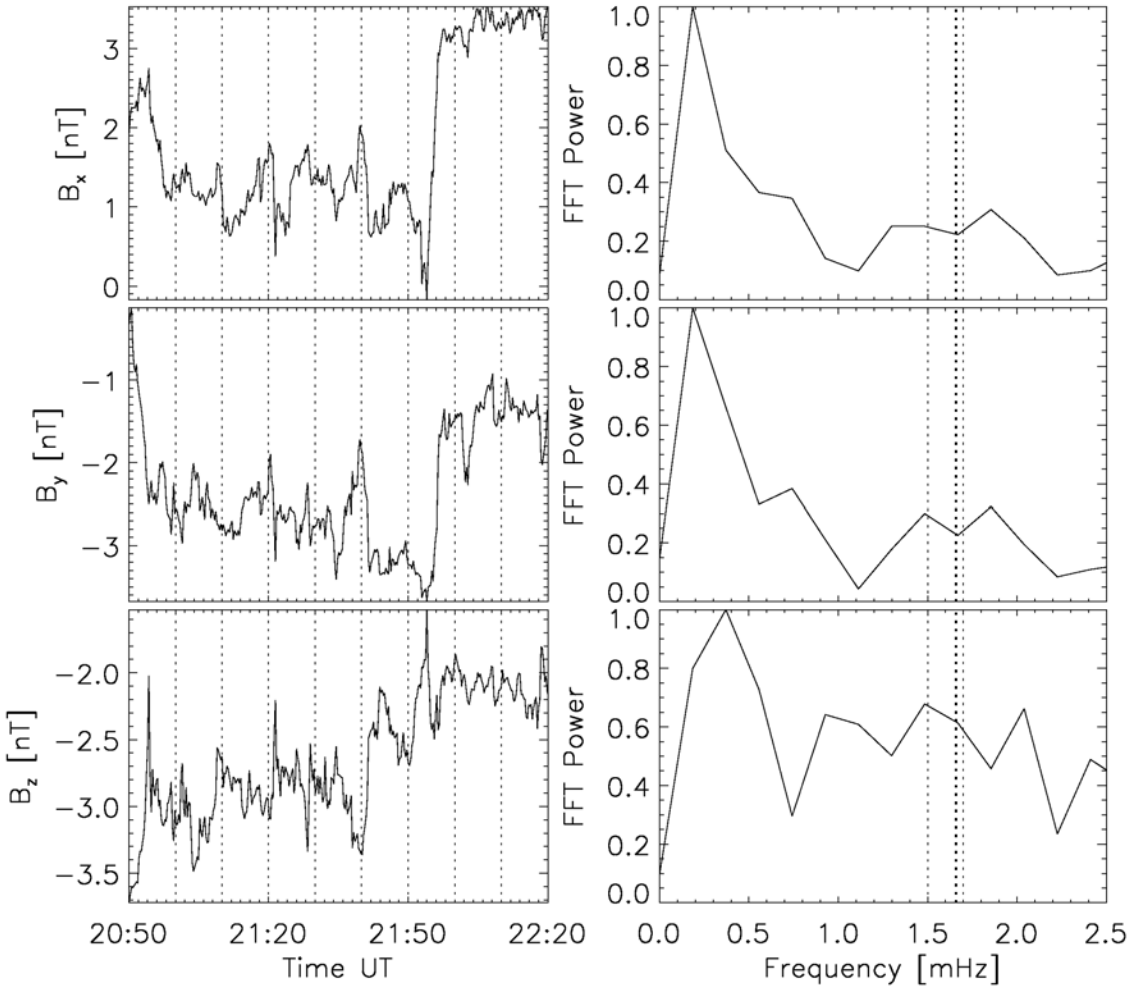

Figure 3.8: Time series of the three GSM components of the IMF. Fourier spectra are shown in the right column.

The right column in Fig. 3.8 shows the Fourier spectrum of the time series on the left. The bold vertical line marks the modulation frequency at 1.67 mHz. The lines to the right and left mark the frequency window for which the dynamic spectrum in Fig. 3.9 was calculated, as discussed later. The Fourier spectra of all IMF components show a broad peak around the modulation frequency. Hence some power at the modulation frequency might have been expected in the ground-based magnetometer sites inside the polar cap around the time of the experiment due to the wave activity in the IMF. However, the raw time series did not show any obvious sign of wave activity in the frequency window concerned.

Fig. 3.9 shows the temporal development of the Fourier power in three frequency ranges for the X, Y and Z GSM component. The power was calculated from a moving time series with a length of 5000 s which leads to a frequency resolution of 0.20 mHz. The legend in the top right corner lists the frequency ranges. The vertical dashed lines mark the beginning and end of the modulation, lagged by the propagation time of the solar wind plasma. The power for all three components in the 1.50 to 1.70 mHz range (solid line) and the adjacent higher frequency band (dashed line) significantly increased during the event. The biggest increase was observed in the X GSM component. The same is not true for the adjacent lower frequency band.

The occurrence of wave activity in the frequency range around the modulation frequency in the IMF could have led to a small enhancement of power in all magnetometer stations in the northern polar cap (compare with the Fourier spectra in Fig. 3.5). But only the data of the Svalbard stations show a large peak due to the activity induced by the modulated heating.

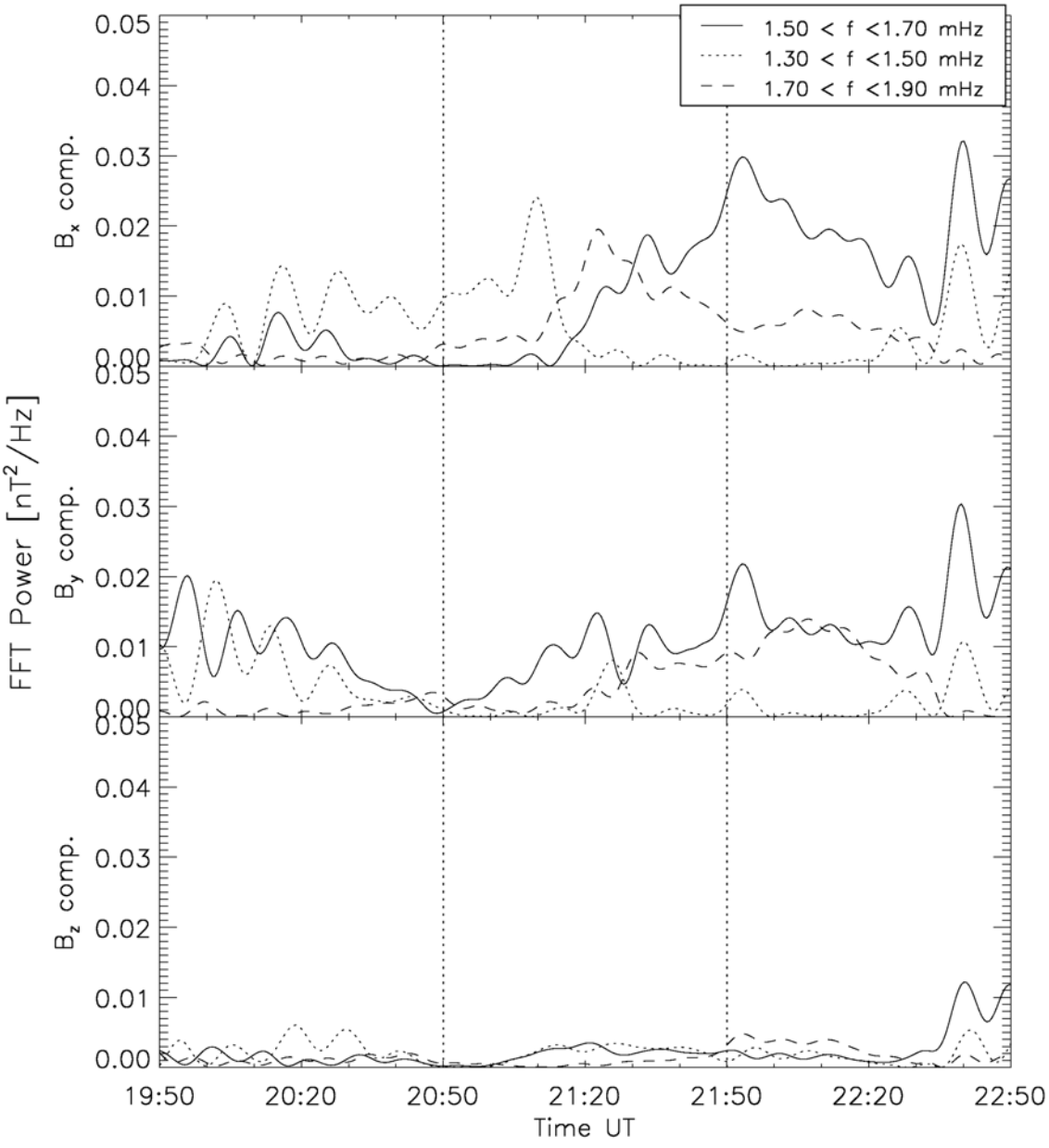

Figure 3.9: Time series of Fourier power in different frequency bands for the three GSM components of the IMF. The vertical dashed lines mark the beginning and end of the modulation event, lagged by 100 minutes propagation time.

3.3 Conclusions

We present strong evidence that a ULF wave registered by three magnetometers on the Svalbard archipelago was stimulated by modulated heating of the ionosphere by the SPEAR system.

During the heating experiment a clear signature of a ULF wave with the same frequency as the modulation was observed in data from magnetometers around SPEAR. The occurrence of this wave activity at stations near SPEAR only during the modulated heating is confirmed by analyzing the development of the corresponding Fourier coefficient over time. Further indications are the constant phase shift between the driver and the observed oscillation and between the observed pulsations themselves.

Signs of wave activity in the frequency range of the modification experiment in other stations located within the northern polar cap were only apparent at a weak level in their Fourier spectra and not in the unfiltered time series. This activity was most likely due to weak activity at this frequency in the IMF.

The data presented here shows that, for the first time, the SPEAR ionospheric heating facility successfully injected ULF waves on open field lines.

4 Large-Scale Pc4 Pulsations

published as

Multi-instrument observations of a large scale Pc4 pulsation,

Annales Geophysicae, 26, 185-199, **2008**

4.1 Introduction

As opposed to the previous chapter, this and the next will be concerned with the observation and analysis of naturally occurring waves in the dayside terrestrial magnetosphere. Both chapters describe waves in the Pc4 frequency range which were observed by a variety of ground- and space-based instruments. In both cases backstreaming ions from the Earth's bow shock will be identified as the source of the observed pulsations.

On 07 November 2005 various ground- and spaced-based instruments registered five wave packets with frequencies in the Pc4 range. The most prominent of the five wave packets was observed in ground-based magnetometer data spanning almost all latitudes on the dayside magnetosphere. The propagation from the dayside into the tail is deduced from Poynting flux calculations of Cluster data and an onset time analysis of the ground-based magnetometer data. This suggests an upstream source. ULF wave activity created by resonant interaction of ions backstreaming from the bow shock is identified to be the most probable source mechanism for this event. Due to the fortunate configuration of the Cluster satellites, the harmonic structure of the wave is analysed and compared with cross-phase spectra from ground data. We present evidence that the driving wave resonantly interacted with geomagnetic field lines. The data suggests that resonant driving occurred at stations where the driving frequency was harmonically related to the local fundamental frequency, creating Field Line Resonance-like signatures.

4.2 Observations

On 07 November 2005 between 1310 and 1410 UT over two dozen ground-based magnetometers around the world registered five wave packets in the upper end of the Pc4 range. During this time, the magnetic footprints of s/c 3 and 4 of the four Cluster satellites were, according to the Tsyganenko 96 (T96) model (Tsyganenko, 1995), conjugate with magnetometers belonging to the CARISMA array (see Sec. 2.1.6). For the time discussed here, this translated to MLTs between 0400 and 0900, i.e. on the dawn flank of the magnetosphere. At the same time and nearly symmetric to the morning side stations, magnetometers belonging to the SAMNET and IMAGE arrays (see Sec. 2.1.6 and 2.1.6) on the evening side between 1400 and 1700 MLT registered the same oscillations.

4.2.1 Ground-Based Magnetometers

Fig. 4.1 shows the X (North-South) component of the magnetic field as measured by magnetometers along three latitude profiles at different MLTs in the left panels. The data have been bandpass filtered between 20 and 80 s. The magnetic latitude of each station and its MLT are given next to its abbreviation in the top left hand corner of each panel. The right hand side panels show the Fourier spectra of the filtered time series, each individually normalised. The spectra have been smoothed using a five point wide boxcar average to eliminate spikes.

As indicated by the vertical dashed lines in Fig. 4.1, five separate ULF wave packets can be identified at all stations. The first between 1312 and 1321 UT, the second between 1323 and 1327 UT, the third between 1330 and 1342 UT, the fourth between 1343 and 1348 UT and the fifth between 1348 and 1353 UT. The occurrence of each packet has been marked by vertical dashed line in Fig. 4.1. The focus of this

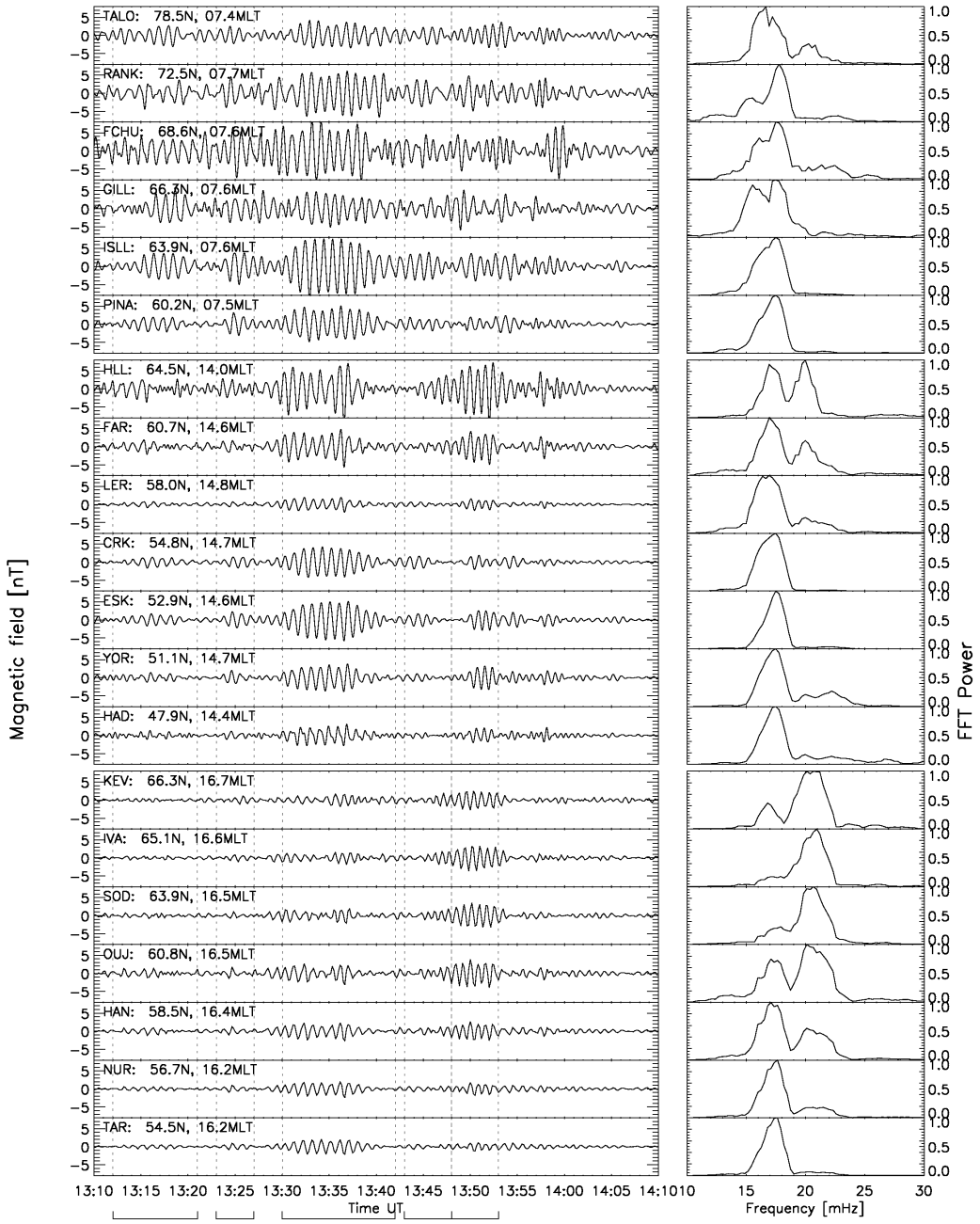

Figure 4.1: Bandpass filtered (20 to 80 s) ground-based magnetometer data from three latitudinal profiles using CARISMA, SAMNET and IMAGE stations on the left. The panels on the right show the normalised smoothed Fourier spectra.

study lies on the wave packet which occurred between 1330 and 1342 UT. It was the most prominent of the five, already well defined in unfiltered data.

Basic Fourier analysis of the interval between 1310 and 1410 UT shows that the frequency of the first four pulsations was 17.2±1.0 mHz whereas the last oscillated at 20.2±1.0 mHz (see right panels in Fig. 4.1). The errors have been estimated from the Full-Width-Half-Maximum of the spectral peaks in Fig. 4.1.

The power at 20.2 mHz dominates the spectra of the northern IMAGE stations SOD, IVA, KEV, whereas in all other spectra the 17.2 mHz peak is dominant. The frequency of each wave packet was constant over all latitudes.

The bandwidth of the filter in Fig. 4.1 was chosen such that any power at double the dominant frequency, i.e. at 34 mHz, is not filtered. There was, however, no signature present at this frequency.

The top six panels of Fig. 4.1 show the data of a line of magnetometers belonging to the CARISMA array in Canada spanning about 20° in magnetic latitude, located around 0700 MLT. The amplitude distribution of the third wave packet over latitude has two maxima, at ISLL and FCHU. Both phase and onset time vary with latitude, however the frequency does not. There is a distinct 180° phase shift between the time series of GILL and FCHU but only a very small shift across the latitude of ISLL. Therefore the amplitude and phase profile over FCHU are indicative of the fact that the observed pulsation is, at these stations, a FLR.

When studied in detail the pulsation between 1330 and 1342 UT consisted of two overlapping yet separate wave packets. SAMNET and IMAGE data (bottom panels in Fig. 4.1) show this more clearly than data from CARISMA stations. The further north the station, the further apart the two wave packets appeared. Since the pulsation occurred simultaneously at all stations, this indicates that it was a

spatial feature rather than a temporal one.

The second batch of seven panels in Fig. 4.1 show data from a latitude profile of magnetometer stations belonging to the SAMNET chain. The profile is located along 78° magnetic longitude (1430 MLT). A wave packet with the same frequency was observed between 1330 and 1342 UT, albeit with a smaller amplitude. Studying latitude profiles of spectral power for these stations at the observed frequency show two maxima in amplitude, one at HLL and the other at ESK. When only considering stations up to LER (58°N), latitude profiles of phase and power show FLR-like behaviour.

At higher latitudes, the oscillation consisted of two packets, as seen in data from CARISMA stations. However, since SAMNET stations reach to lower latitudes, the merge was completed below 54° (CRK) such that the oscillation then seemed to consist of only one wave packet.

Data of a latitude profile of stations belonging to the IMAGE chain are shown in the seven bottom panels of Fig. 4.1. These stations stretch along a line at 105° magnetic longitude (1600 MLT). Again, the same pulsations as in the two other chains were observed with even lower amplitudes. No signs indicating a FLR were observed in the spectral power and phase profiles. The splitting of one wave packet at lower latitudes into two at higher latitudes was again observed.

To determine the azimuthal wave number m of the observed pulsation, phase shifts at stations along longitudinal profiles both on the dusk and dawn side have been analysed. The phase of the 17.2 mHz component was obtained from Fourier analysis of the unfiltered signal. A summary is given in Tab. 4.1. The m number is then obtained by dividing the observed phase shift by the longitudinal separation. By convention the eastward direction is associated with positive m numbers.

Dawn			Dusk		
Name	Longitude [°]	Phase [°]	Name	Longitude [°]	Phase [°]
DAWS‡	273	-59			
FSIM‡	294	-37	DOB⋆	090	-40
FSMI‡	306	-24	HAN⋆	104	-47
RABB‡	318	-04	MEK⋆	108	-53
Difference	45	55	Difference	18	-13
m	-1.2			0.7	

Table 4.1: Phase in degree at 17.2 mHz for different stations along longitudinal profiles determined by Fourier analysis.
‡CARISMA stations
⋆IMAGE stations

With increasing longitude the phase increases on the morning side, corresponding to a negative m number and westward propagation. On the evening side, the phase decreases with increasing longitude resulting in a positive m number, equivalent to eastward propagation. This corresponds in both cases to a propagation of the wave in an anti-sunward direction. The absolute value is in both cases around one, confirming that this wave was a large-scale phenomenon.

Although it is not shown, it is worth noting that pulsation signatures identical to those described above were observed on the dayside by magnetometers located on Greenland, South America and Antarctica. These wave packets were clearly a global magnetospheric phenomenon with the exact same frequency at all stations. From these additional sources only the Antarctic stations yielded a large enough amplitude for analysis. However due to the low power construction of these magnetometers, the time stamp associated with each measurement is uncertain by up to two minutes, thus rendering these data useless for timing analysis.

Weak but coherent signals of the pulsation described here were also recorded at stations located on the nightside. Data from Japanese magnetometers at magnetic latitudes between 20° and 40° and 2300 MLT show pulsations at 17.2 mHz with

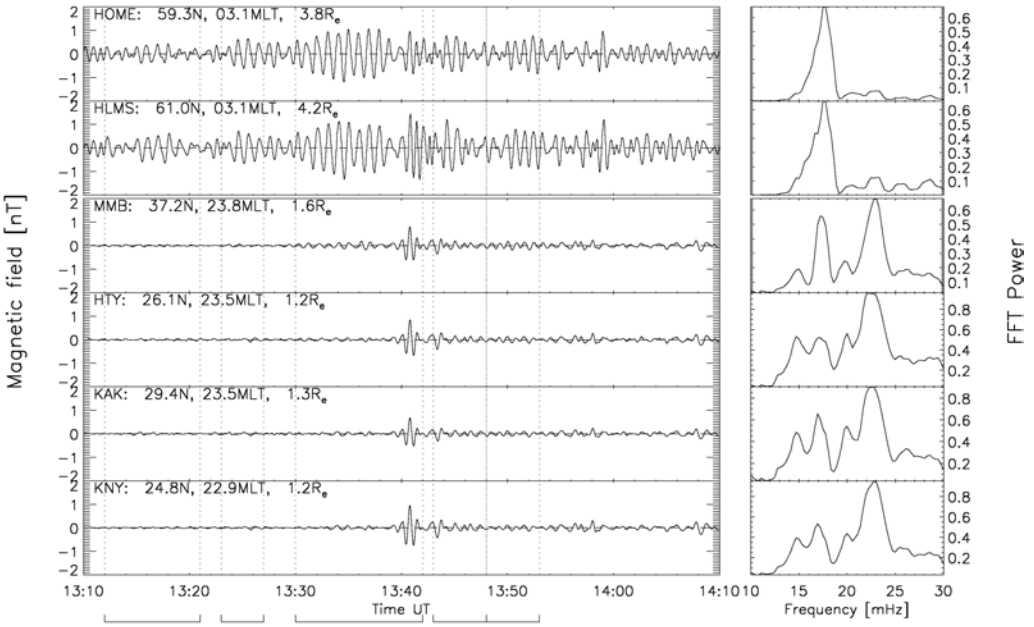

Figure 4.2: Magnetic field data in the X direction from Alaska (top two panels) and Japan (bottom four panels).

amplitudes around 0.2 nT. Magnetometers in Alaska (60° magnetic latitude, 0300 MLT) recorded the pulsation with an amplitude of 1 nT. The filtered data for a selection of stations is shown in Fig. 4.2.

4.2.2 Space Based Observations

During the interval under study, the Cluster spacecraft were relatively close to perigee. Thus the formation of the Cluster satellites during the event was rather like pearls on a string. Cluster 2 was leading, followed by Cluster 1, 3 and 4, each separated by about 2 R_e (see Sec. 2.1.5). Their orbit took them from the southern hemisphere through perigee at about 5 R_e over the northern hemisphere to apogee into the tail. Due to this orbital configuration, Cluster 3 and 4 sampled the magnetic and electric field variations along essentially the same bundle of field lines (see Fig. 4.3). At the time of the wave event Cluster 1 and 2 had already passed the inner

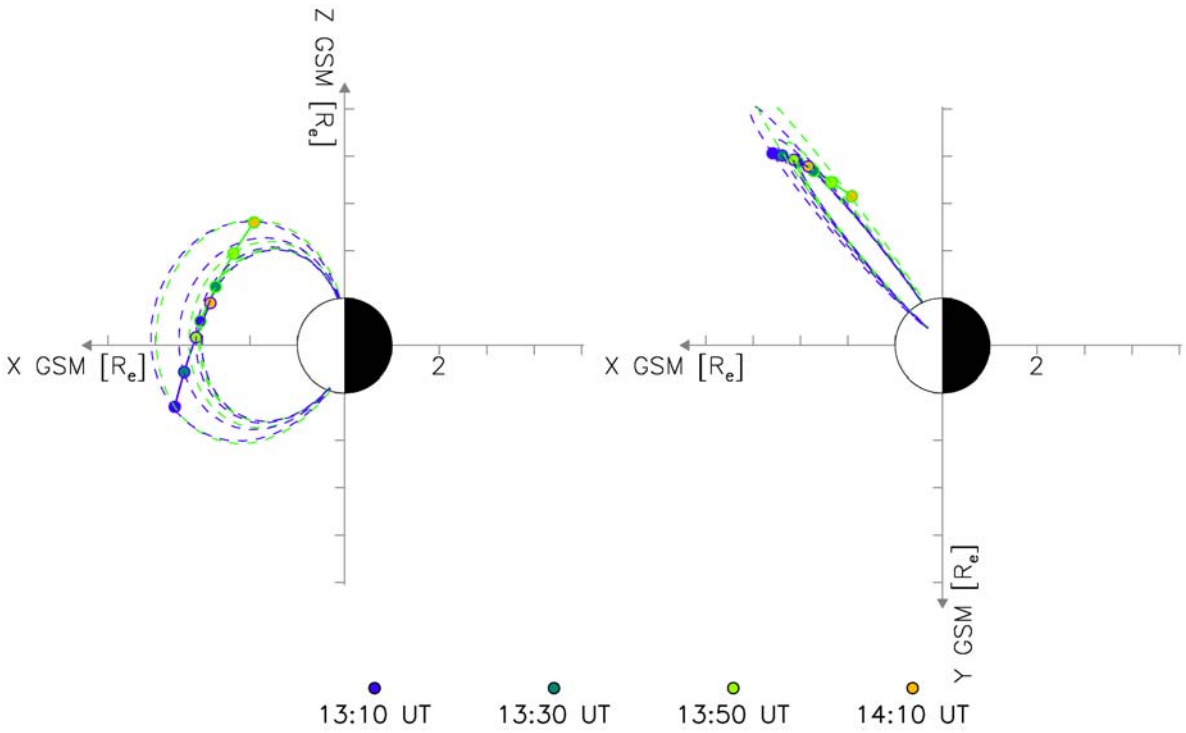

Figure 4.3: Cluster s/c 3 (green) and s/c 4 (blue) orbit between 1310 UT and 1410 UT on 07 November 2005. Also shown is the T96 model geomagnetic field with input parameters $p_{dyn} = 1.5$ nPa, $Dst = -15.0$, $B_y = -1.5$ nT, $B_z = -0.5$ nT.

magnetosphere and were on open field lines connected to the northern polar cap. Hence only Cluster 3 and 4 data will be discussed in this study.

The magnetic field was measured by the FGM instrument (see Sec. 2.1.5) onboard the Cluster satellites. It is available in GSE coordinates at spin resolution (4 s). The electric field data was gathered by the EFW instrument (see Sec. 2.1.5). The original electric field data were provided by the Cluster Active Archive and consist of two components in the X-Y GSE plane, also at spin resolution.

After the E_z component has been calculated from the raw magnetic and electric field data following (2.2), all components have been bandpass filtered to allow periods between 20 and 80 s and then transformed into the mean-field aligned coordinate system (see Sec. 2.1.5). The magnetic field data were averaged over 150 points (10

min) to obtain the mean-field direction.

Since the electric field was constructed under the assumption that it is perpendicular to the magnetic field, the field-aligned component of the electric field in the MFA system will be identical zero. Hence only the azimuthal and the radial component of the electric field are displayed in the following discussions.

The right panels in Figs. 4.4 and 4.5 show the Fourier spectra for the filtered time series. The spectral powers have been smoothed using a five point wide boxcar average to eliminate spikes. Then the spectra were normalised by the maximum value of each component for each quantity individually. Please note that the range of the y axis is not the same for all spectra.

The left panels show time series of the magnetic and electric field and the oscillatory Poynting flux. All quantities are plotted versus UT, L-value, MLT and magnetic latitude of the spacecraft. The dipole tilt angle respective to the Z-GSM axis during the event was about -9°.

The top three left panels in Figs. 4.4 and 4.5 show the filtered components of the magnetic field for Cluster 3 and 4 in the MFA coordinate system, respectively. All five wave packets are clearly visible in the data and the polarisation of the wave is revealed. The magnetic perturbation at 17.2 and 20.2 mHz was confined to the field-aligned and azimuthal direction, showing that the wave consisted of a superposition of a transverse toroidal and a compressional mode. This is true for data from both s/c 3 and 4.

The existence of a significant compressional component of the wave is confirmed when looking at the fourth panels in Figs. 4.4 and 4.5. The left panels show the unfiltered time series of the magnetic magnitude after a 6^{th} order polynomial fit has been subtracted to enhance small amplitude variations Kivelson et al. (1997).

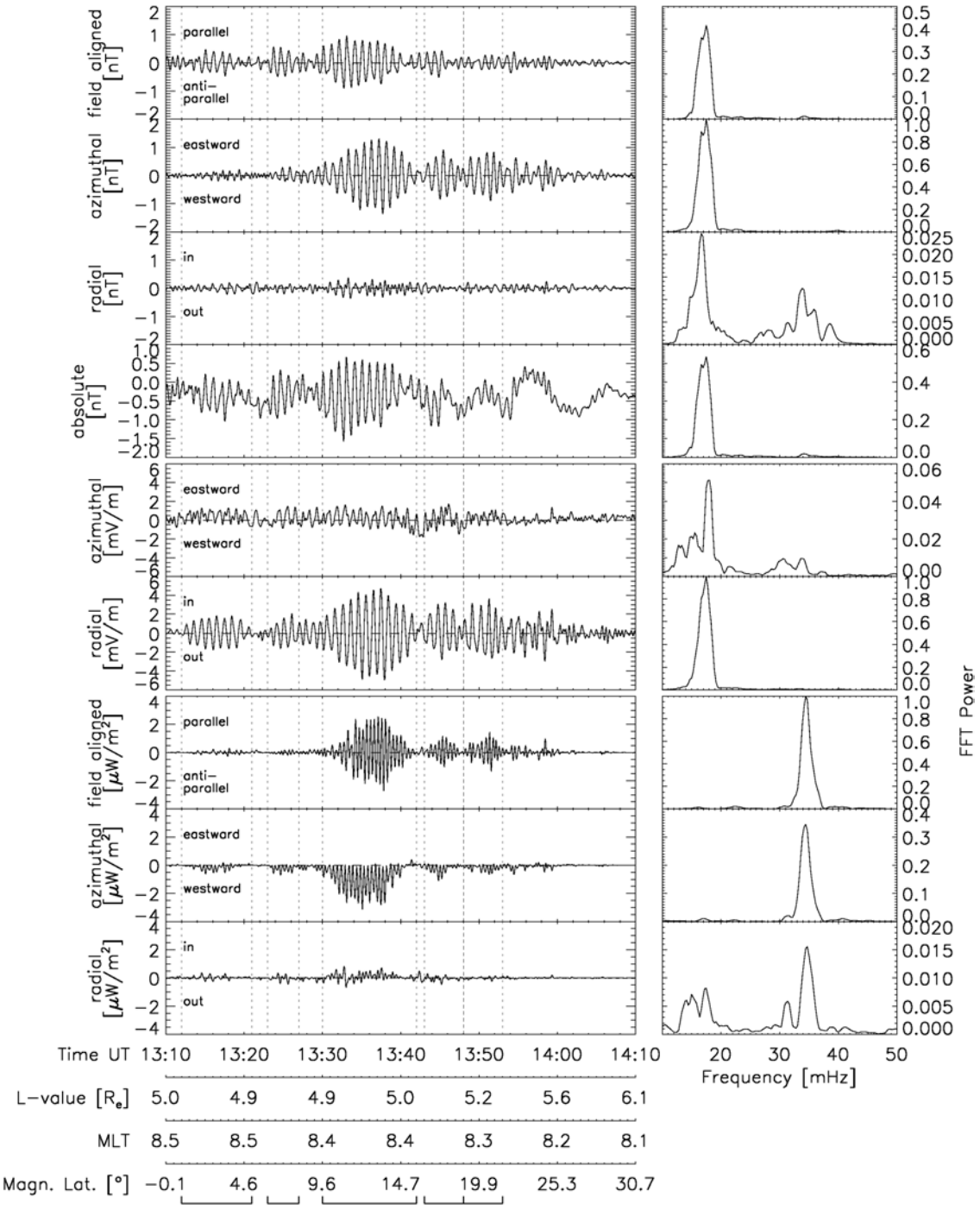

Figure 4.4: Summary of field data in MFA coordinates from s/c 3. The top four panels show the magnetic field, followed by the electric field and the oscillatory Poynting flux. The right hand side panels show the respective smoothed Fourier spectra.

Certainly the largest of the wave packets between 1330 and 1342 can be clearly observed. Additionally, the associated Fourier spectra of both spacecraft data reveal clear peaks at 17.2 mHz, indicating a wave associated with a perturbation in the magnetic field strength, as is expected for a compressional pulsation (see Sec. 1.2.2).

The Fourier spectra show that the compressional and poloidal component of Cluster 3 magnetic field as well as the toroidal electric field contained a weak signal at double the main frequency, i.e. at 34 mHz. The same is true for the Cluster 4 data.

The envelopes of the main pulsation seen by the FGM onboard Cluster 3 and 4 in the field-aligned components show under close inspection two maxima, whereas the azimuthal components show only one.

The amplitude of the pulsation as seen by Cluster 3 was about twice that seen by Cluster 4. Whereas the signal in the field-aligned direction had no phase shift between the two spacecraft the oscillation in the azimuthal direction was 180° out of phase.

The electric field shown in panels five and six in Figs. 4.4 and 4.5 also shows a clear polarization in the MFA coordinate system. The bulk of the power was concentrated in the radial direction with all five wave packets clearly visible. During the time of the largest wave packet (1330 until 1342 UT), a weak pulsation is observed in the azimuthal component. The signals from both satellites in the radial direction were in phase. A considerable difference in the packet's envelope was observed.

From the three perturbation components of the electric field $\vec{e_1}$ - one of which is identical zero - and the magnetic field $\vec{b_1}$ the three components of the perturbation Poynting vector $\vec{s_1}$ have been calculated via

$$\vec{s_1} = \frac{1}{\mu_0}(\vec{e_1} \times \vec{b_1}). \tag{4.1}$$

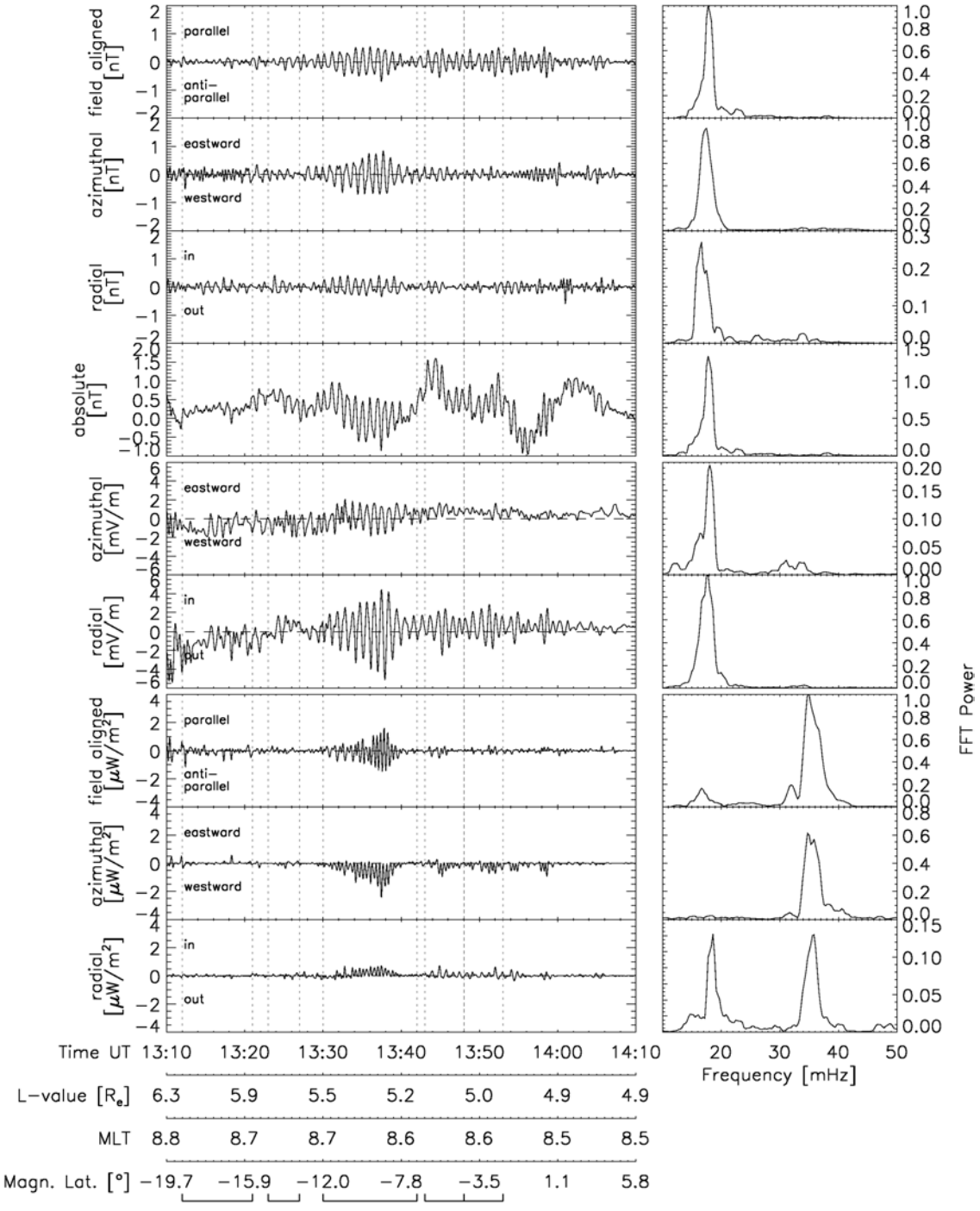

Figure 4.5: Summary of field data from Cluster 4, same format as Fig. 4.4.

Since $\vec{s}_1$ was calculated from the filtered components it represents the Poynting flux of the wave field only.

Due to the polarisation of $\vec{e}_1$ and $\vec{b}_1$ in the MFA coordinate system the Poynting vector was polarised as well, having comparable amplitudes in the field-aligned and azimuthal component (see bottom three panels of Figs. 4.4 and 4.5). The period of the oscillation was, as expected, double that of $\vec{e}_1$ and $\vec{b}_1$. The field-aligned component of $\vec{s}_1$ for Cluster 3 showed a slight asymmetry around the zero line, indicating more flux parallel to the background magnetic field than anti-parallel. Since Cluster 3 was located about 12° above the magnetic equator, this indicates that some of the wave's energy was lost in the northern polar ionosphere. The same is true for observations at Cluster 4 position, however here the energy was lost in the negative field-aligned direction into the southern hemisphere, in accordance with the satellites position below the magnetic equator at -9° magnetic latitude.

The azimuthal flux at both satellites was, considering their position in the magnetosphere, purely tailward, i.e. westward, negative azimuthally. The asymmetries in both the field-aligned/azimuthal flux is a direct and sole result of phase shift between the azimuthal/field-aligned magnetic and radial electric field components at both satellites.

The small signals in the field-aligned direction of the electric field results in some flux in a radially inward direction, more so at Cluster 4.

4.3 Discussion

4.3.1 Wave Origin and Motion

The observed pulsations were clearly a global phenomenon since they were observed by ground-based magnetometers in different hemispheres spanning 24 hours of MLT. It is thus of special interest to discuss the structure and frequency of the wave in order to assess where it was generated and what the source mechanism was. Later, Cluster's orbit configuration gives us the unique opportunity to study the structure of the wave along a bundle of field lines and thus explore the wave's harmonic mode.

As discussed earlier, the magnetic field and Poynting flux data suggest that the wave was composed of two modes, Alfvénic and compressional. While the Alfvénic flux oscillated along the background magnetic field between the two hemispheres depositing energy in the polar ionospheres, the flux of the compressional component (magnetic oscillation field-aligned) was also highly asymmetric. Virtually all flux was directed tailward. This leads to the assumption of an anti-sunward travelling compressional wave from which energy was locally converted into the Alfvénic mode. The pulsations seen by the ground-based magnetometers are then due to these Alfvénic oscillations.

Since the speed of the proposed compressional disturbance is finite, the onsets of the pulsations in the ground-based measurements are dependent on this speed and on the position of the point where the adjacent field line of each station crosses the X-Y GSM plane. For convenience, this point will be called the crosspoint in the following discussion.

The geographic position of each magnetometer belonging to the CARISMA, IMAGE and SAMNET chain has been traced along the adjacent field line into the equato-

rial plane of the GSM coordinate system (see Fig. 4.6), thus finding each station's crosspoint. The tracing utilised the T96 model with input parameters derived from measurements of the Geotail satellite (p_{dyn} = 1.5 nPa, $Dst = -15.0$, $B_y = -1.5$ nT, $B_z = -0.5$ nT). Due to the finite step size of the T96 model, the Z values of the equatorial positions were not zero, however they were less than 0.2 R_e for all stations.

To determine the onset time of each station, the filtered time series between 1330 and 1342 UT of each station of the three chains have been cross-correlated with the time series of one reference station. HAD from the SAMNET chain was chosen to be the reference station since the pulsation occurred first in its data.

The sampling interval of IMAGE stations is ten seconds as opposed to one second for SAMNET stations, therefore before cross-correlation the reference data have been downsampled by calculating the average over ten seconds. The same procedure was applied before cross-correlating the reference data with the four second sampled Cluster magnetic field measurements. Finally the onset time was then determined by extracting the lag of the maximum cross-correlation. The onset value for each station is indicated by the colour of the station's crosspoint marker in Fig. 4.6.

Tamao (1964) investigated the propagation of a MHD wave from a point source through a cold uniform plasma. He then applied his findings qualitatively to a MHD wave propagating through the magnetosphere to an observer on the ground.

The source Q emits compressional waves in all directions, as indicated by the dotted concentric lines in Fig. 4.7. These waves travel with the local Alfvén speed as the plasma is assumed to be cold (comp. Sec. 1.2.2), and they are attenuated as r^{-1}, r being the distance from the source. Along its path the fast mode constantly converts to the Alfvén mode, which then travels along the magnetic field line without

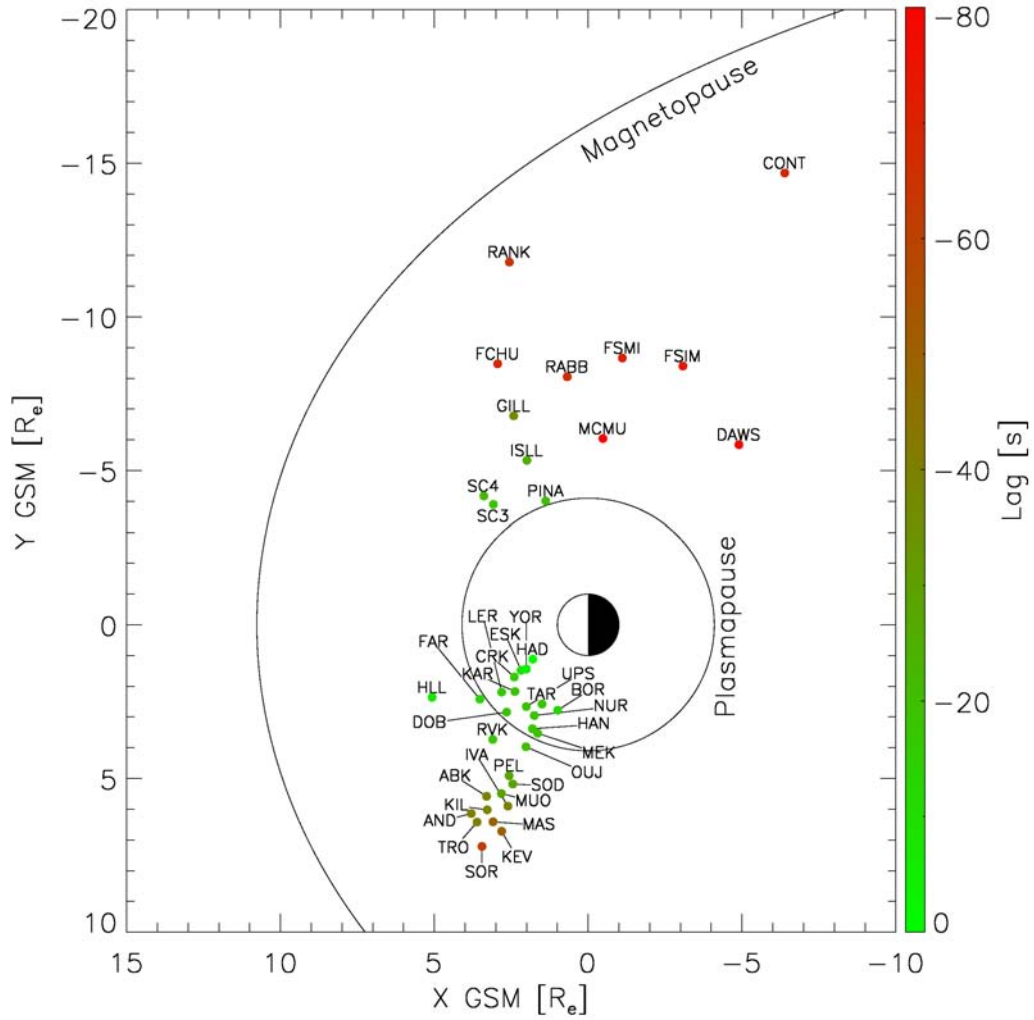

Figure 4.6: Equatorial crosspoints of field lines adjacent to ground magnetometer stations in GSM coordinates. The lag of the arrival of the pulsation is colour coded according to the scale on the right. The magnetopause position was calculated according to Shue et al. (1997). The plasmapause is shown following Larsen et al. (2007).

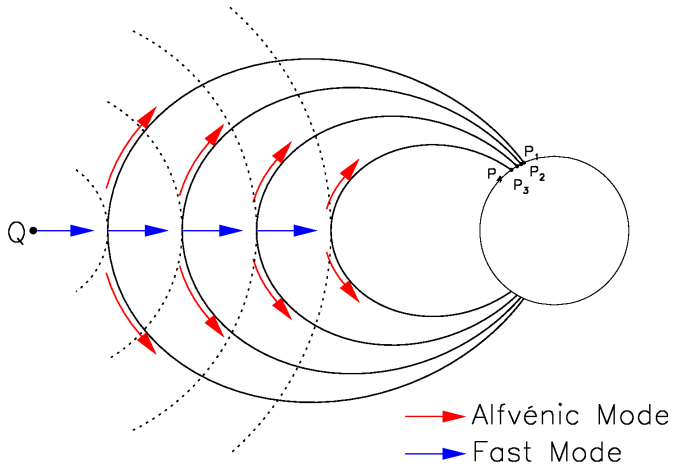

Figure 4.7: Qualitative MHD wave propagation inside the Earth's magnetosphere from a source Q to an observer P_1, P_2, P_3, P_4 on the ground. The path shown is that identified by Tamao (1964) as the least attenuated one.

further attenuation to P_1, P_2, P_3, P_4, the observer on the ground. Hence most power is transported to the ground by a path which minimises the length the wave travels as fast mode. This path is depicted in Fig. 4.7 as a straight arrow in blue from the source to the field line connected to P_1, P_2, P_3, P_4, followed by the red arrow indicating the Alfvén mode travelling along the magnetic field line. This model was successfully used by Chi et al. (2001) to explain arrival times of preliminary reverse impulses.

Additional to the lag time due to different paths of the wave to the observer on the ground, the phase shifts resulting from an internal resonance structure of the pulsation will influence the observed onset times. Whereas the wave propagation along different paths will constitute the bulk of the lag time, the internal resonance structure of the pulsation can only change the lag times by ± 30 s, i.e. ± one half period.

In order to be able to estimate the travel times of the waves along the "Tamao path", the local Alfvén speed is needed. Here the T96 model provides the mag-

netic field for the calculations, the equatorial mass density $\rho_0(r)$ can be modelled in two parts, the first applying to the plasmasphere (subscript ps), the second to the magnetosphere (subscript ms) (compare Chi et al., 2001)

$$\rho_0(r) = \begin{cases} \rho_{ps} \left(\frac{r_{pp}}{r}\right)^3, & r \leq r_{pp} \\ \rho_{ms} \left(\frac{r_{mp}}{r}\right)^3, & r > r_{pp}, \end{cases} \tag{4.2}$$

where r_{pp} is the geocentric radius of the plasmasphere.

The density profile along the field line was assumed to be

$$\rho = \rho_0(r) \left(\frac{r_0}{r}\right)^{\alpha} \tag{4.3}$$

where α is the density index and ρ_0 is the proton mass density at r_0, the crosspoint of the field line considered, r is the geocentric distance to the position of interest on the field line. Denton et al. (2002) found the density index at an L-value of 5 R_e, which is the position of the Cluster satellites, to be around $\alpha = 2$. For the following calculations this value was chosen.

For each station in Fig. 4.6 the travel time along a straight line from the source to the crosspoint was calculated using (4.2) to model the density profile. The travel time of the Alfvénic mode along the magnetic field line as predicted by the T96 model was than added. Finally, the minimum travel time of all stations was subtracted from all travel times such that these relative times can be compared to the relative times determined by the afore mentioned cross-correlation technique.

Optimal values for the mass densities were found by systematically varying ρ_{ps} and ρ_{ms} until the best agreement between observation and model was reached. The density just inside of the plasmapause ρ_{ps} was varied between 25 amu/cm^3 and 300

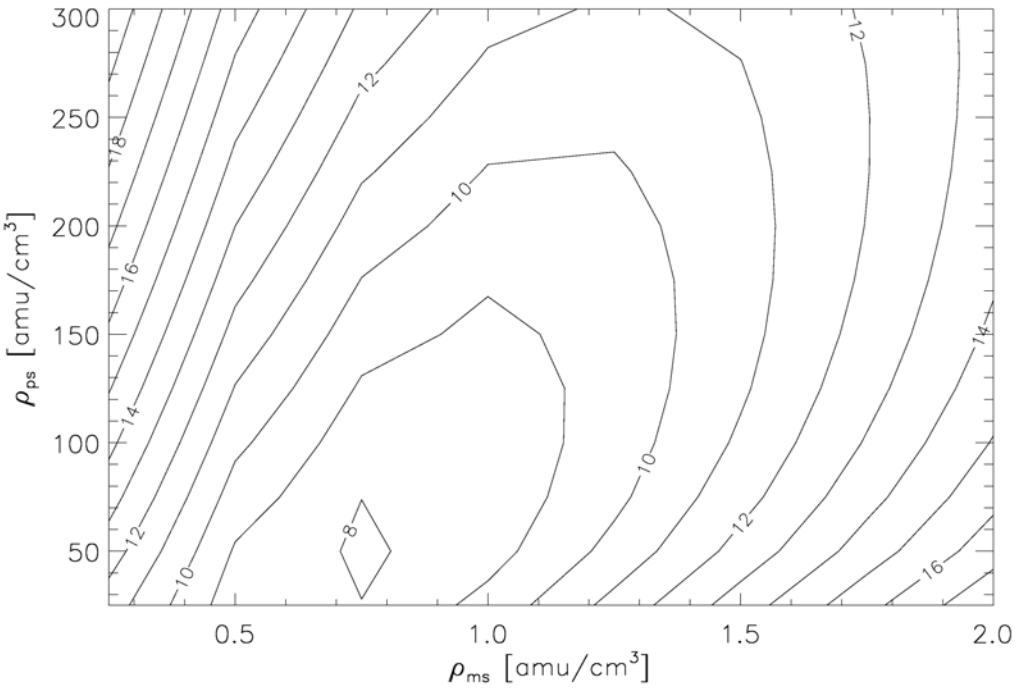

Figure 4.8: Standard deviation between observed and modelled lag times for various magnetospheric and plasmaspheric density values.

amu/cm^3 in steps of 25 amu/cm^3. The magnetospheric density just inside of the magnetopause was varied between 0.25 amu/cm^3 and 2.0 amu/cm^3 in 0.25 amu/cm^3 steps. For each pair of density values model travel times were computed. The standard deviation of the differences between model and observational time lags of all stations has been used as a quantifier for the goodness of fit of the input density values. A contour plot of the achieved standard deviations for the different input parameters is shown in Fig. 4.8.

Fig. 4.8 shows that the minimal standard deviation was located in a global minimum for the tested density parameters. The contours also reveal that the goodness of fit was more dependent on ρ_{ms} than on ρ_{ps}. The densities producing the smallest deviation of 7.8 were then chosen as the optimal input parameters for our model. These values were $\rho_{ms} = 0.75$ amu/cm^3 and $\rho_{ps} = 50$ amu/cm^3.

A plasmaspheric density of $\rho_{ps} = 50$ amu/cm^3 seems rather low, however note that changing this value to a more sensible value of 150 amu/cm^3 increases the standard deviation marginally from 7.8 to 8.4 s. On the other hand changing the magnetospheric density from 0.75 to 1.5 amu/cm^3 increases the standard deviation to over 12 s.

As mentioned earlier, the observational lag times of some stations might have been affected by additional time shifts due to local resonance effects. However the spread of the station's positions over large parts of the dayside of the magnetosphere both in MLT and L-shell (compare Fig. 4.6) means that only few of the stations will have been affected by such additional shifts. Hence this intuitive measure for the goodness of the model is suitable for this situation.

The geocentric distance of the plasmapause was derived from a recent model by Larsen et al. (2007). They found that the following parameters strongly correlate with the plasmapause position: the IMF Z-GSM component B_z, IMF clock angle $\theta = \arccos(B_z/\sqrt{B_y^2 + B_z^2})$ and a merging proxy $\phi = VB_{tot}\sin^2\theta/2$, where V is the solar wind speed and B_{tot} is the IMF magnitude. The delay in the plasmapause response to the changing parameters was found to be 180 min for B_z, 175 min for θ and 240 min for ϕ. According to Larsen et al. (2007) the plasmapause position r_{pp} can then be calculated via

$$r_{pp}[\mathrm{R_e}] = 0.050B_{z,180} + 0.108\theta_{175} - 1.110 \times 10^{-4}\phi_{240} + 4.23, \tag{4.4}$$

which for the interval discussed here yields $r_{pp} = 4.1$ R$_\mathrm{e}$. Please note that this model does not account for the MLT dependence of r_{pp}.

For our calculations the magnetopause position was assumed to lie at $r_{mp} = 10$ R$_\mathrm{e}$. To find the location of the upstream source its position was varied using the

same scheme as for the mass densities. For 80 points along a line parallel to the Y GSM axis at Z = 0 R_e and X = 10 R_e between -4 $R_e \leq Y \leq 4$ R_e the model lag times and the standard deviation of the differences between the lag times were calculated. It was found that the best agreement, i.e. the lowest standard deviation, between observation and model is achieved when assuming the source to lie at (10, 0, 0) R_e. This position is consistent with what will be inferred about the wave's origin later in this section.

The observed and the modelled lag times as a function of the L-value of each station are shown in Fig. 4.9. The general agreement between the predicted and observed travel times is good. The model predicts the minimum travel time for HAD station, a result which is also obtained by the cross-correlation technique. Generally the modelled travel times are lower than those observed. Qualitative differences like "The pulsation first reached FAR, then OUJ and then PINA" are well reproduced by the model. The time resolution for the IMAGE magnetometers is 10 s such that the observed lags can only be determined to that accuracy.

Fig. 4.10 shows a plot of the observed lag times against the predicted lag times. If the model were perfect, all points would lie on the $y = x$ line as indicated by the thick dashed line. Fig. 4.10 shows that the calculations from the model density values mostly underestimate the lag times, i.e. overestimate the Alfvén speed. This suggests on underestimation of the mass densities which seems plausible as the best agreement was calculated for $\rho_{ps} = 50$ amu/cm3.

All the above observations suggest an upstream source, hence the wave generation mechanism as discussed in Sec. 1.2.6 seems the most likely. Takahashi et al. (1984) found that the frequency of waves generated by this mechanism can be parametrised by the IMF strength B_{tot} and the cone angle θ_{xB} as given by (1.79).

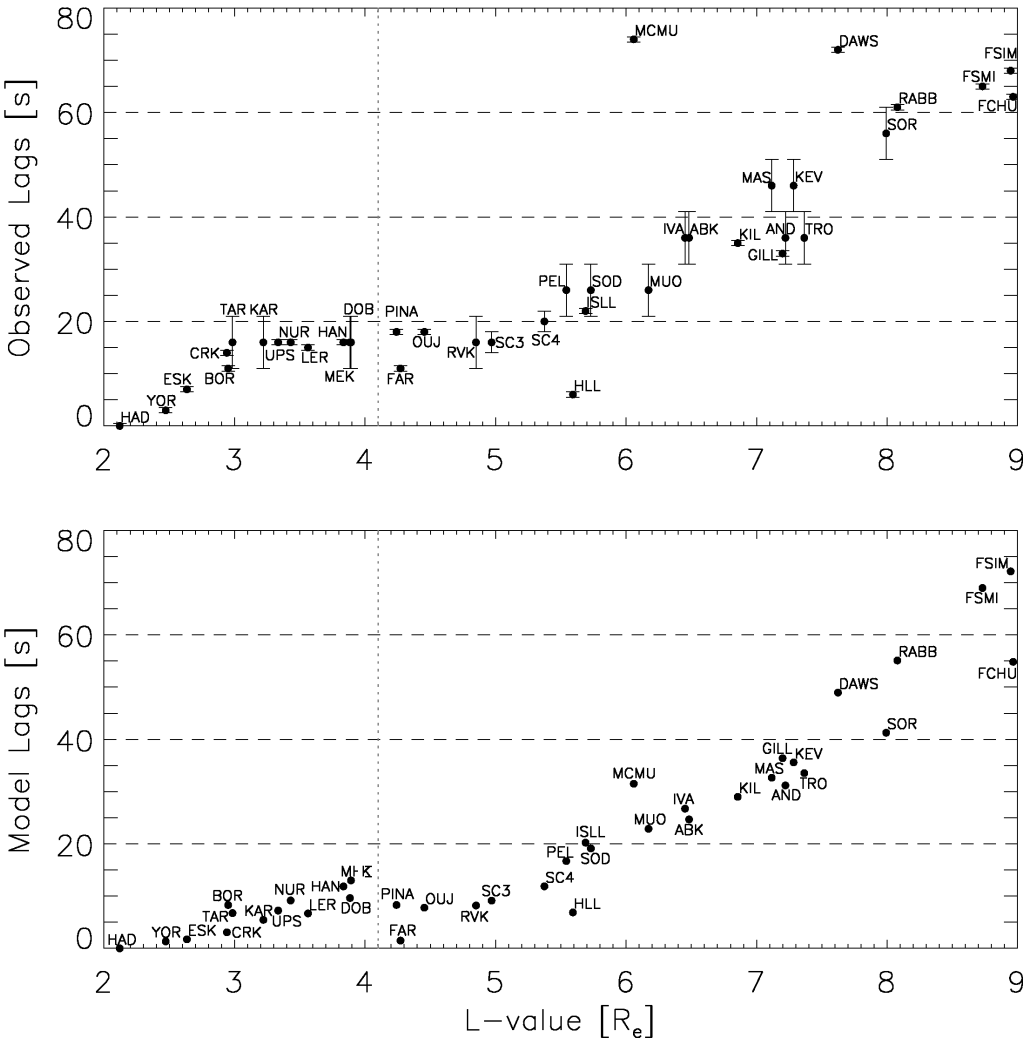

Figure 4.9: Observed lag times (top panel) and relative predicted lag times (bottom panel). The dotted vertical line indicates the modelled plasmapause stand-off distance. The error bars in the top panel are due to the different sampling frequencies of the different magnetometers.

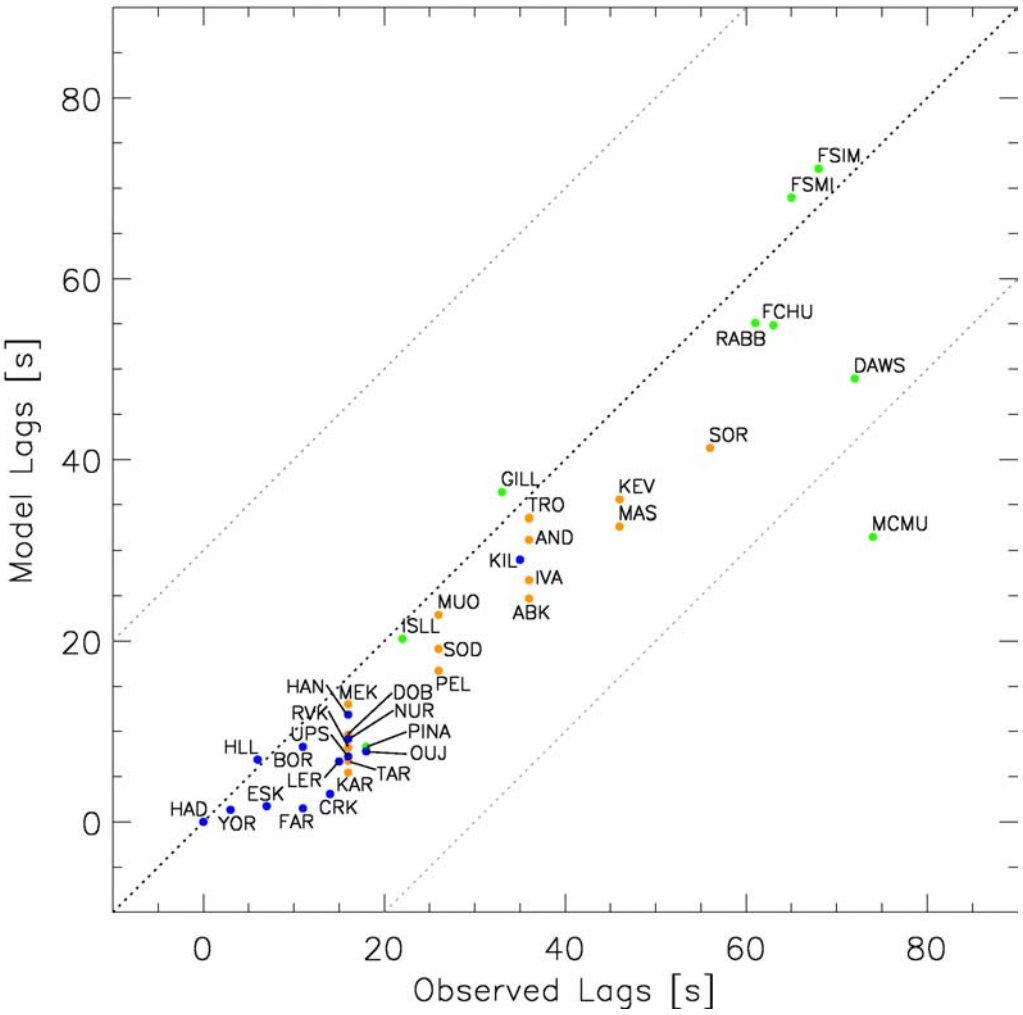

Figure 4.10: Observed lags plotted against modelled lags.

During the event, the Geotail satellite was located inside the solar wind close to the Earth's bow shock on the evening side at (12, 13, -12) R_e in GSM coordinates. From its magnetic field data θ_{xB} was calculated and the frequency of the upstream generated waves at the subsolar point has been estimated using (1.79) (see Fig. 4.11). The predicted frequency matches reasonably well with the frequency observed and we can hence assume with confidence that the waves observed by ground-based magnetometers inside the magnetosphere were caused by a resonant interaction at the Earth's bow shock.

4.3.2 Harmonic Structure

The onset times and the source of the observed pulsations has been identified in the previous section. In this section we will attempt to explain the distribution of wave amplitudes with latitude.

The cross-phase technique (see Sec. 2.2.1) was employed to estimate the fundamental eigenfrequency of field lines. We can then investigate whether and how the observed oscillation was related to a normal mode of the considered field lines.

The results for some example cross-phase calculations of data from SAMNET stations are shown in Fig. 4.12. As discussed in Sec. 2.2.1, the fundamental eigenfrequency of the field line half way between the two magnetometer station of which data is used is characterised by maximum cross-phase values. Hence the eigenfrequency is identified in a cross-phase dynamic spectrum (see Fig. 4.12) as that frequency where the colour coded cross-phase reaches maximal values. As also discussed in the introduction, the eigenfrequency of a field line is primarily dependent on its length. Since a field line's length at constant latitude changes depending on its location in magnetic local time, a variation of the fundamental eigenfrequency

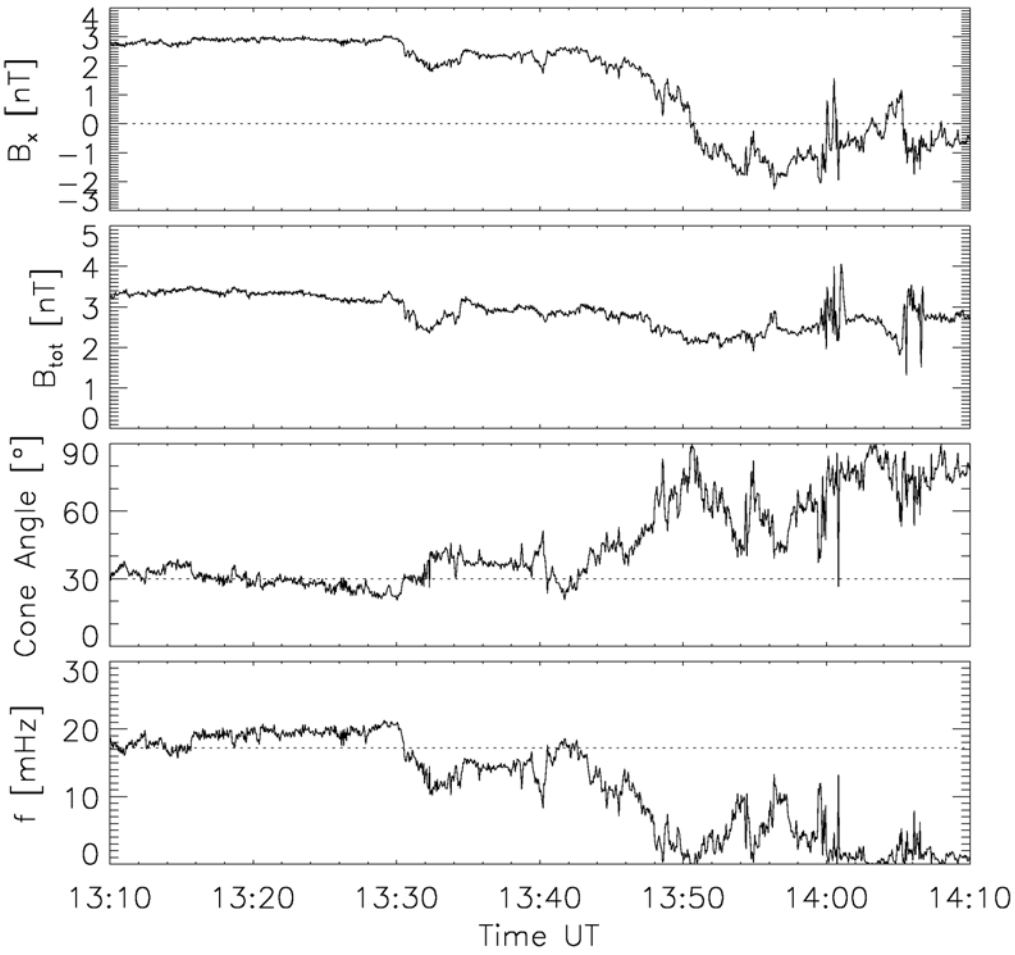

Figure 4.11: Magnetic field data from Geotail. The cone angle θ_{xB} and the predicted upstream generated frequency f are shown in the two bottom panels. The dashed line in the third panel gives the threshold (30°) for the cone angle below which the generation process of upstream waves is especially effective at the sub-solar point. The horizontal dashed line in the bottom panel indicates the observed frequency at 17.2 mHz.

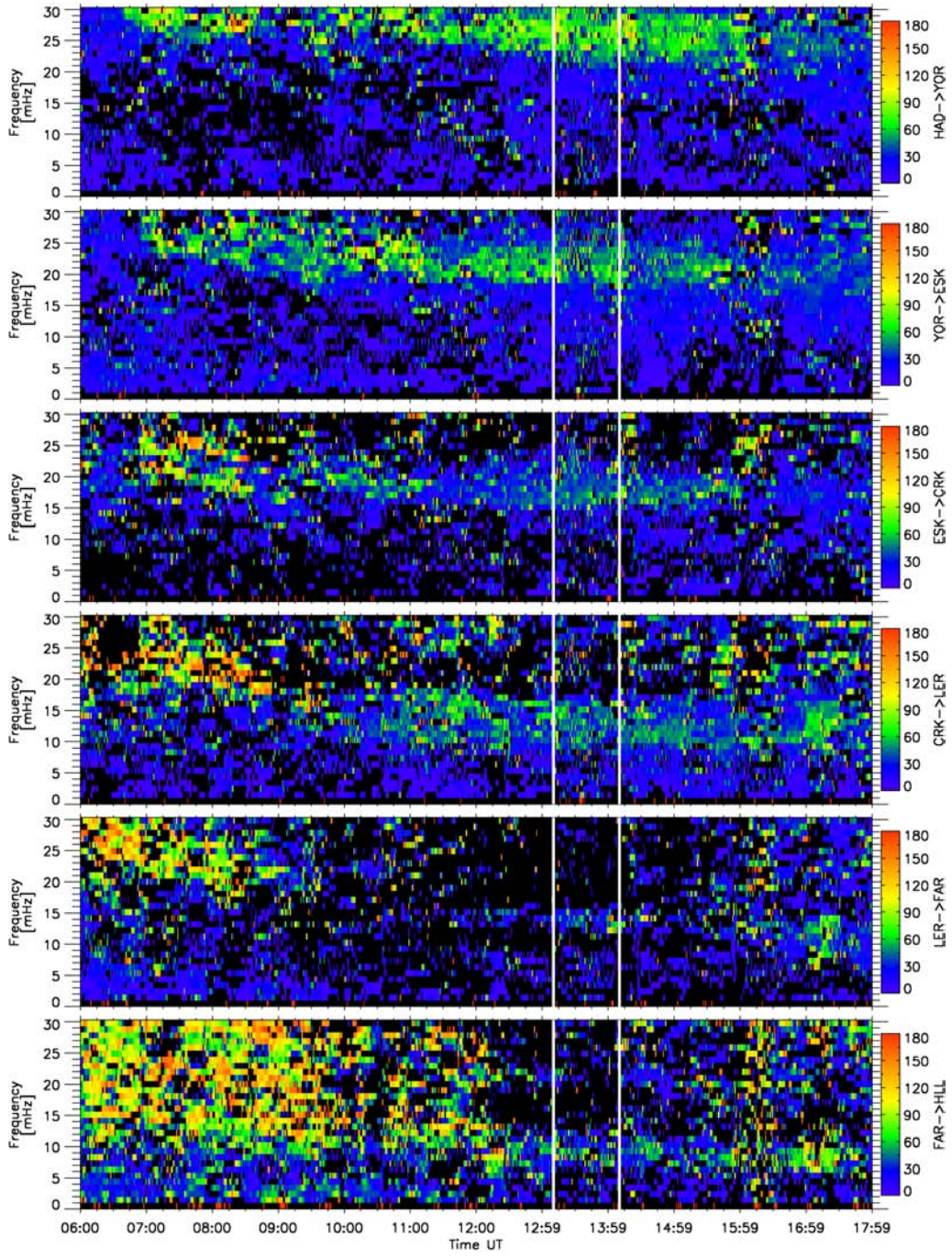

Figure 4.12: Cross-phase spectra of stations belonging to the SAMNET array. The stations from which the cross-phase was calculated are given next to the colour bars. The interval during which the pulsations occurred is marked by vertical white lines.

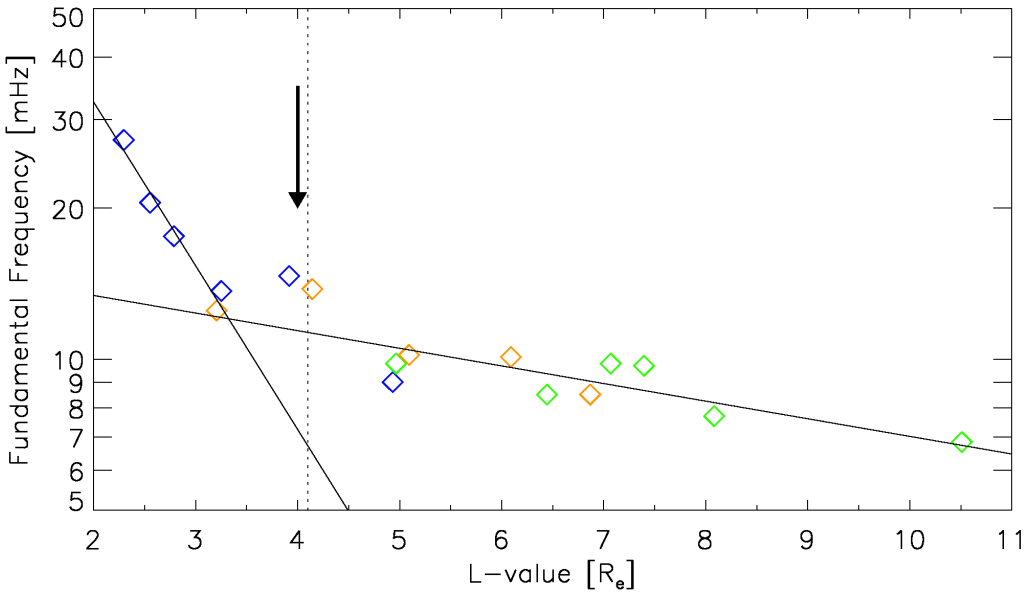

Figure 4.13: Fundamental frequency over L-value. CARISMA stations are coloured green, SAMNET stations are blue and IMAGE stations are orange. The dotted vertical line indicates the position of the plasmapause predicted by (4.4).

with time can be expected.

In Fig. 4.12 the decreasing frequency with increasing latitude is clearly visible, as well as an expected variation of the fundamental frequency with local time (Waters et al., 1995). This technique yields clearer results for data from the evening flank. However, due to the symmetry of the CARISMA station and SAMNET station locations, conclusions drawn from the latter may be applicable to the morning sector (compare Fig. 4.6).

The fundamental frequencies f_{fund} in mHz of 16 suitable pairs of stations from all three magnetometer arrays have been determined from the cross-phase spectra. After averaging all cross-phase values for each frequency bin over the time of the event (1310 - 1410 UT), the frequency at which the average was largest yielded the eigenfrequency of the field line. These frequencies are plotted over the average L-value of the station pairs in Fig. 4.13.

The natural frequency decreases with increasing L-value, with a steeper gradient inside the plasmasphere than inside the magnetosphere. The position of the plasmapause can be identified as the position of a "bump" in the curve, as indicated by an arrow in Fig. 4.13. Its location coincides with the result derived from (4.4) as marked by the dotted vertical line. The results presented here are very similar to those presented in Fig. 3 of Menk et al. (2004).

Least-squares fitting a straight line to the data points in the two regimes (plasmasphere and magnetosphere) as indicated by the solid lines in Fig. 4.13 yields two functional dependencies of the fundamental frequency f_{fund} on L-value L:

$$\log_{10} f_{fund}(L) = \begin{cases} 2.17 - 0.33L, & L \leq 4\mathrm{R_e} \\ 1.20 - 0.04L, & L > 4\mathrm{R_e} \end{cases} \tag{4.5}$$

During the fitting process the two points comprising the bump in Fig. 4.13 have been excluded. Using the above formula, an individual fundamental frequency for each station in Fig. 4.6 depending on its L-value can be calculated.

It was already remarked that ground-based magnetometer data show maximal amplitudes at two different latitudes. In an attempt to explain this amplitude distribution, the fundamental eigenfrequency of each station as determined from (4.5) was plotted against the spectral power of each station's time series at 17.2 mHz.

The idea is that the amplitude of the pulsation and thus the spectral power at 17.2 mHz of the ground-based data was higher at latitudes where the driving pulsation was harmonically related to the fundamental eigenfrequency because the driving wave could then have resonantly interacted with the local field line.

Panel a) of Fig. 4.14 shows the spectral power at 17.2 mHz over the fundamental

eigenfrequency. The colours indicate the station's chain, blue for SAMNET stations, orange for IMAGE and green for CARISMA. The station abbreviations are given above or below their respective circle. The vertical bold dashed line marks the frequency of the driving pulsation, i.e. 17.2 mHz.

The harmonic relationship for geomagnetic field line eigenfrequencies was studied for a dipole magnetic field by Schulz (1996). At $L = 6$ they found the ratio of the eigenfrequency of the fundamental f_1 to that of the second harmonic f_2 for the toroidal eigenmodes to be $f_1/f_2 = 0.39$ (compare Table 1 in Schulz, 1996). Hence at the field line with an fundamental eigenfrequency of $17.2 \cdot 0.39 = 6.7$ mHz the driving frequency matches that of the second harmonic. This frequency has been marked in Fig. 4.14 by a second vertical dashed line at 6.7 mHz. For L-values between 2 and 6.6 the ratio varies by about 25%. In Fig. 4.14 this variation has been indicated by a gray band.

The lower panels of Fig. 4.14 show latitude profiles of the phase at 17.2 mHz of selected stations determined by FFT analysis. Panel b) shows a latitude profile of CARISMA stations and panel c) of SAMNET stations. The same stations as plotted in the lower panels are connected by lines in panel a).

The reader is reminded that the fundamental eigenfrequency of a field line is inversely proportional to the latitude of its footprint if the equatorial mass density and the density distribution along the field line is assumed constant. Hence field lines with foot points at higher latitudes will have lower fundamental frequencies. Hence, the top panel of Fig. 4.14 can also be looked at as a latitude profile of spectral power. For an ideal FLR such a profile shows a peak in power at the latitude of the resonant field line, accompanied by a 180° phase shift across that latitude.

The orange circles representing the IMAGE data offer no clue as to whether

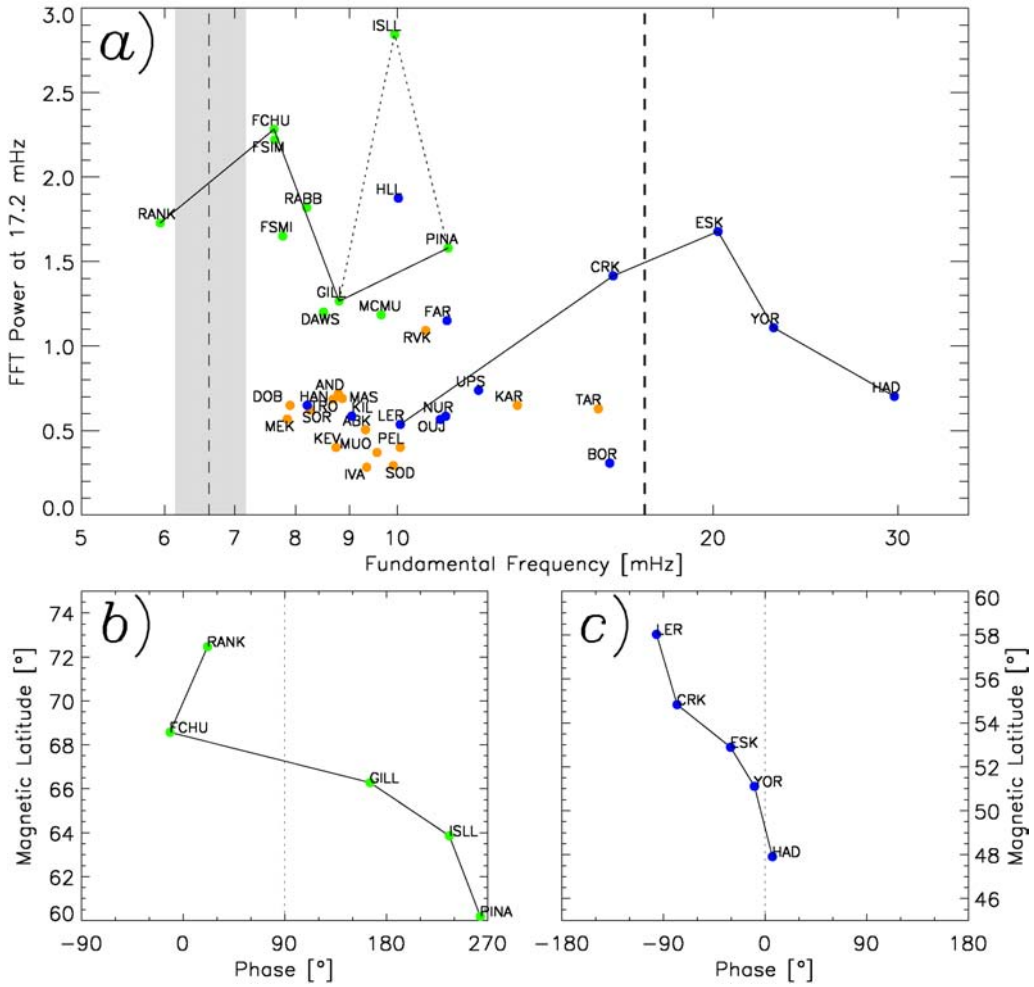

Figure 4.14: *a)* Fundamental eigenfrequency against spectral power at 17.2 mHz. CARISMA stations are coloured green, SAMNET stations are blue and IMAGE stations are orange.
b) Latitude profile of the FFT phase of selected CARISMA stations; these are connected by straight lines in panel a).
c) Latitude profile of the FFT phase of selected SAMNET stations; these are connected by straight lines in panel a).

resonant interaction between the global wave and any local field lines took place. This is due to the overall small signal strength at these stations combined with an unfortunate position of the fundamental eigenfrequencies of the field lines connected to IMAGE stations between the two frequencies marked in Fig. 4.14.

The spectral powers of a latitude profile of stations belonging to the SAMNET array (HAD, YOR, ESK, CRK and LER) have been connected by straight lines in Fig. 4.14. The accompanying Fourier phases have been plotted in panel c). Both plots provide strong evidence that across this latitude ($\sim$54° magnetic latitude), where the driving and local fundamental eigenfrequency matched, resonant interaction took place and a FLR was generated.

The fundamental eigenfrequency at BOR was, according to Fig. 4.14, also close to that of the driving wave. Hence an enhancement in power could be expected. However, the power at BOR is low due to the station's position at 17 MLT which is a long way away from the sub-solar point, where the compressional driving wave was generated, and hence it will have attenuated significantly before mode converting at the field line connected to BOR.

Conversely, power at HLL is high although its fundamental frequency is not close to any of the frequencies where resonant interaction is expected. However, the station's crosspoint is located closer to the sub-solar point on the bow shock than that of BOR. Hence the compressional wave generated upstream will have attenuated much less before mode converting at the crosspoint of HLL, resulting in a stronger signal on the ground.

Hence the amplitude distribution of the SAMNET data can only partly be explained by resonant interaction of the driving wave with a local field line.

A second latitude profile at higher latitudes on the dawn side consisting of CA-

RISMA stations has also been marked in Fig. 4.14. It consists of the stations PINA, ISLL, GILL, FCHU, RANK. The corresponding Fourier phases are shown in panel b). Ignoring the power value at ISLL for a moment, again a clear signature of a FLR emerges. This indicates that the driving wave generated a FLR on the dawn side at a latitude where the second harmonic frequency of the local fundamental matched the driving frequency.

The above discussion shows that our idea of resonant interaction can only explain parts of the amplitude distribution of the Fourier powers with latitude. The high power value at ISLL remains puzzling because the fundamental frequency at that latitude was not harmonically related to the driving frequency and its crosspoint was not significantly closer to the sub-solar point on the bow shock than that of PINA.

As can be seen in Fig. 4.3, the two Cluster satellites were located along the same bundle of field lines during the entire event. This, together with the global, simultaneous appearance of the wave in ground-based magnetic data, strongly indicates that the observed wave packets were a temporal rather than a spatial feature. The separation of the two spacecraft was 2 R_e on the same field line, therefore phase information from the magnetic and electric field data can be used to learn more about the spatial structure of the wave along the field line.

The cross-phase method was used to determine the relative phase shift of the Fourier component at 17.2 mHz and its evolution during the event for the field-aligned and azimuthal magnetic component between the two spacecraft. The phase difference of the field-aligned component was constant at about 0°, whereas the phase shift in the azimuthal component was constant at 180°.

Since the compressional parts of the magnetic field were in phase, the following

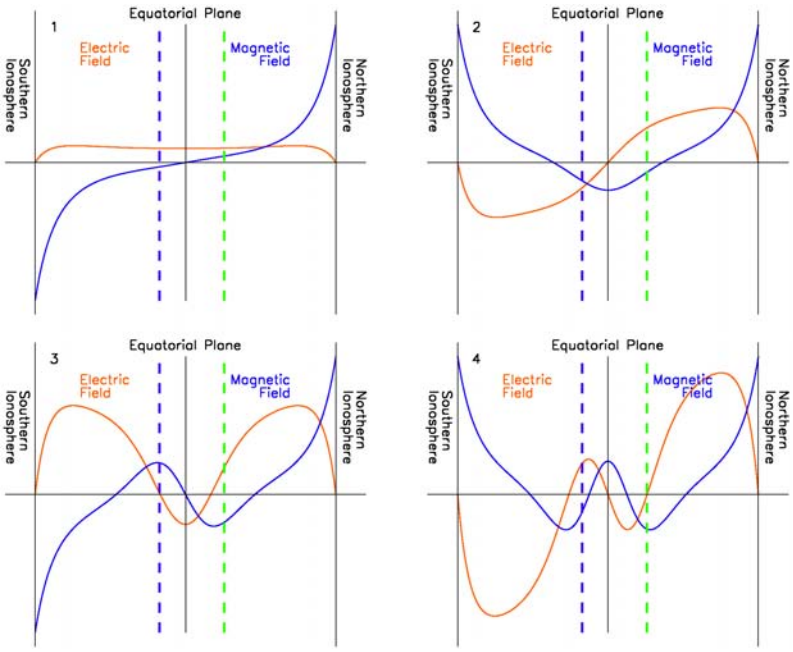

Figure 4.15: Numerical solution of the wave equation on a dipolar field line. The first four harmonics are shown. Superimposed are the scaled positions of the Cluster 3 (dashed green line) and 4 (dashed blue line) spacecraft.

considerations are only valid for the Alfvénic mode. The phase shift of the azimuthal magnetic components between the two spacecraft was 180°, whereas the radial electric components were in phase. Numerically solving the decoupled first-order wave equation along a dipole magnetic field line as described in Sec. 1.2.4 (Sinha and Rajaram, 1997) yields solutions for the magnetic and electric field. The following observations are qualitative and are only concerned with the node structure of the oscillation.

The density profile along the field line was, as before, assumed to be given by (4.3). Again, $\alpha = 2$ and it is worth noting that variations of the density index did not significantly change the positions of the nodes.

The result of a numerical integration using the standard fourth-order Runge-Kutta method is shown in Fig. 4.15. Note that the delineation shows, for the sake of clarity,

the two quantities at times of maximum amplitude. Superimposed are the positions of the Cluster spacecraft as dashed lines. Since the dipole field line in this sketch is represented by a straight line, the positions of the spacecraft have been scaled accordingly.

The numerical solution in Fig. 4.15 is based on the assumption that conductivities in both the northern and southern ionosphere are identical. This assumption does not hold for the position of the field lines adjacent to the Cluster satellites during the time of the event. The ionosphere at the southern foot point of the involved field lines was sun lit, whereas it was not at the northern end. Hence the ionospheric conductivities are expected to be lower at the northern than at the southern foot point. However, Streltsov and Lotko (1997) investigated the influence of finite ionospheric conductivity on the structure of dispersive, non-radiative FLRs for the first four odd harmonics. Their results are based on a linear, magnetically incompressible, reduced, two-fluid MHD model which includes effects of finite electron inertia (at low altitude) and finite electron pressure (at high altitude). They found that assuming different conductivities for the northern ($\Sigma_P = 2\,\mathrm{mho}$) and southern ($\Sigma_P = \infty\,\mathrm{mho}$) ionospheres do not significantly change the positions of the nodes.

The first and third harmonics seem possible solutions to explain the observed spatial phase shifts of the wave field, i.e. 0° between the two radial electric and 180° between the two azimuthal magnetic fields. Schäfer et al. (2007) found that the fundamental eigenfrequency of a toroidal standing wave on a dipole field line at $L = 5\ \mathrm{R_e}$ under similar magnetospheric conditions is about 13 mHz. Similar values around 10 mHz can be extracted by eye from the cross-phase spectra of data from the morning side ground-based magnetometers (see Fig. 4.13). Hence it is more likely that the observed wave at 17.2 mHz at the Cluster position has a node

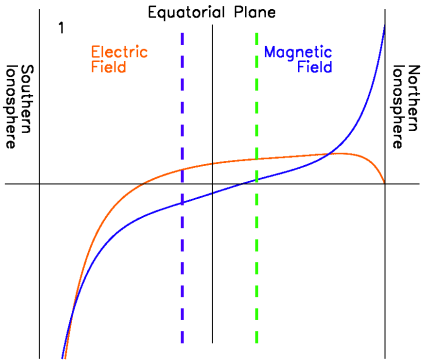

Figure 4.16: Resulting node structure when a 17.2 mHz wave is fed into the Runge-Kutta algorithm. The vertical dashed lines again show the scaled positions of the Cluster spacecraft 3 (dashed green line) and 4 (dashed blue line).

structure related to the fundamental or the second harmonic rather than one related to the third harmonic.

When feeding the Runge-Kutta algorithm with a 17.2 mHz wave and assuming that the electric field had a node only on one end of the field line, the picture as delineated in Fig. 4.16 emerges. It has the same format as Fig. 4.15. Under the assumption that the electric field had a node in the northern hemisphere, the observed phase shifts in the Cluster data can be reproduced.

The astute reader will notice that the southern end of the field line connects to the sun-lit hemisphere. There the conductivities were probably higher than at the dark northern foot point. Hence the node in the electric field is more likely to have been in the southern end as opposed to the northern as delineated in Fig. 4.15. However, the observed phase shifts in the Cluster data can only be reproduced when assuming the node in the electric field to have been at the northern foot point. It is possible that auroral precipitation changed the local ionospheric conductivities at the footprint of the field lines connected to the satellites such that the above scenario becomes plausible.

4.4 Conclusions

On 07 November 2005 five wave packets in the Pc4 frequency range have been observed in ground-based magnetometer data from stations spanning virtually all latitudes and all MLTs. The most prominent of the wave packets had a frequency of 17.2 mHz and an azimuthal wave number m of about 1. The frequency was constant at all latitudes.

The onset times of the pulsation and the Poynting flux calculated from space-based data show that the wave was propagating from the dayside into the nightside. This suggests an upstream source. Since no apparent trigger was found in solar wind data, we believe that the wave was generated by backstreaming ions at the Earth's bow shock. Estimations of the frequency of wave originating from such a process using empirical relations support this scenario. The compressional part of this wave then propagated through the bow shock and the magnetosheath into the magnetosphere. There its energy partially converted into Alfvénic modes which were observed as a global phenomenon by ground instruments.

Due to the unique spatial arrangement of two Cluster spacecraft the harmonic structure of the wave packet along the same bundle of field lines has been studied. A simple comparison between the phase shifts of the azimuthal magnetic and radial electric field between the two spacecraft and numerical solutions of the wave equation suggest that at an L-value of 5 R_e on the dawn flank the observed pulsation had a node structure similar to that of the fundamental. However uncertainties in the numerical solution exist that could effect the node structure and hence its interpretation.

Using the cross-phase technique, fundamental eigenfrequencies of field lines connected to ground-based magnetometers have been calculated and compared with

that of the observed pulsation and the Cluster observations. At latitudes comparable with that of the Cluster footprint these data suggest that the pulsation was oscillating at a frequency between the local fundamental and second harmonic frequency. This observation is supported by the observed phase shift at the Cluster satellites and numerical simulations.

On the dusk side the incident wave generated a FLR at a latitude where the local fundamental eigenfrequency matched the driving frequency. On the dawn side indications for a FLR are found across the latitude where the driving frequency matched the second harmonic of the local fundamental.

Some of the features of the discussed event remain puzzling. The high amplitudes observed on the ground at ISLL cannot be explained by resonant interaction of local field lines and the driving wave (see Fig. 4.14). The splitting of the wave packet as observed on the ground could be due to different damping rates at different latitudes (see Fig. 4.1). Lower damping at lower latitudes could be responsible for the merging of two wave packets into what appears to be one. And lastly the signal at double the main frequency in the spacecraft data (see Fig. 4.4 and 4.5) could be connected to a mechanism called "frequency doubling" as described in Takahashi and McPherron (1982), Higuchi et al. (1986) and Mann et al. (1999).

5 Upstream Waves in the Magnetosphere

published as

First simultaneous measurements of waves generated at the bow shock in the solar wind, the magnetosphere and on the ground, *Annales Geophysicae,* 27, 357-371 **2009**

5.1 Introduction

For the last event presented in this thesis we will turn to the 05 September 2002, when the Geotail satellite observed the cone angle of the IMF change to values below 30° during a 56 minute interval between 1814 and 1910 UT. This triggered the generation of upstream waves at the bow shock, 13 R_e downstream of the position of Geotail. Upstream generated waves were subsequently observed by Geotail between 1830 and 1848 UT, during times when the IMF cone angle dropped below values of 10°.

At 1824 UT all four Cluster satellites simultaneously observed a sudden increase in wave power in all three magnetic field components, independent of their position in the dayside magnetosphere. We show that the 10 minute delay between the change in IMF direction as observed by Geotail and the increase in wave power observed by Cluster is consistent with the propagation of the IMF change from the Geotail position to the bow shock and the subsequent propagation of waves generated upstream of the bow shock through the bow shock, magnetosheath and magnetosphere towards the position of the Cluster satellites.

We go on to show that the wave power recorded by the Cluster satellites in the component containing the poloidal and compressional pulsations was broadband and unstructured; the power in the component containing toroidal oscillations was structured and shows the existence of multi-harmonic Alfvénic continuum waves on field lines. Model predictions of these frequencies fit well with the observations. An increase in wave power associated with the change in IMF direction was also registered by ground-based magnetometers which were magnetically conjugate with the Cluster satellites during the event.

5.2 Observations

5.2.1 Space-Based Observations

Geotail

On 5 September 2002 between 1800 and 1930 UT the Geotail satellite was located at (29, 7, 2) R_e in GSM coordinates, about 13 R_e upstream of the Earth's bow shock. The three IMF components B_x, B_y, B_z in GSM coordinates and the magnitude B_{tot} measured by the magnetometer onboard the spacecraft are shown in the top four panels in Fig. 5.1. The bottom panel shows the IMF cone angle θ_{xB}, i.e. the angle between the Sun-Earth line and the direction of the IMF.

Before 1814 UT the cone angle of the IMF was around 90° due to small B_x values. At 1814 UT B_x abruptly changed to negative values around -5 nT causing the cone angle to drop below 40°. Between 1814 and 1824 UT the cone angle decreased further with two excursions to values above 40° at 1817 and 1822 UT.

Between 1824 and 1910 UT the cone angle was mainly below 30° with brief excursions to slightly higher values at 1851 and 1858 UT. From 1830 to 1848 UT it reached very low values averaging around 10°.

During this interval of very low cone angle pulsations in the magnetic field were observed, 13 R_e upstream the Earth's bow shock. The peak to peak amplitude was around 0.5 nT in the X, 2 nT in the Y and 4 nT in the Z component. At this time the field was essentially orientated in negative X direction and hence the pulsations were predominantly transversely polarised. However, as significant pulsation activity was also observed in the field magnitude, compressional waves were present, too.

Fig. 5.2 shows dynamic spectra of the three GSM components of the magnetic field measured by Geotail. The FFT length was about 6.5 minutes (128 points)

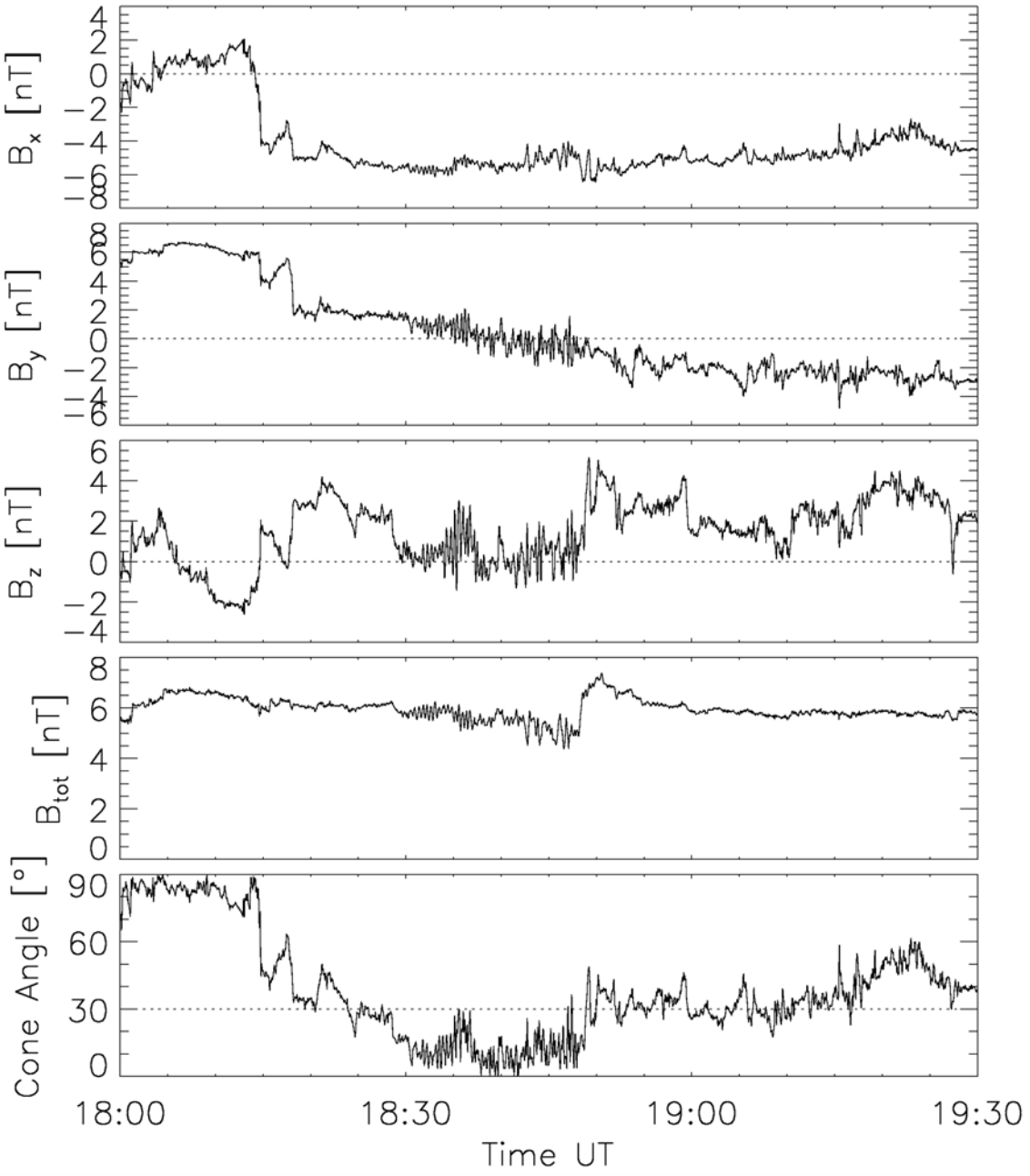

Figure 5.1: IMF measured by the MAG instrument onboard Geotail in GSM coordinates on 05 September 2002. The bottom panel shows the IMF cone angle θ_{xB}.

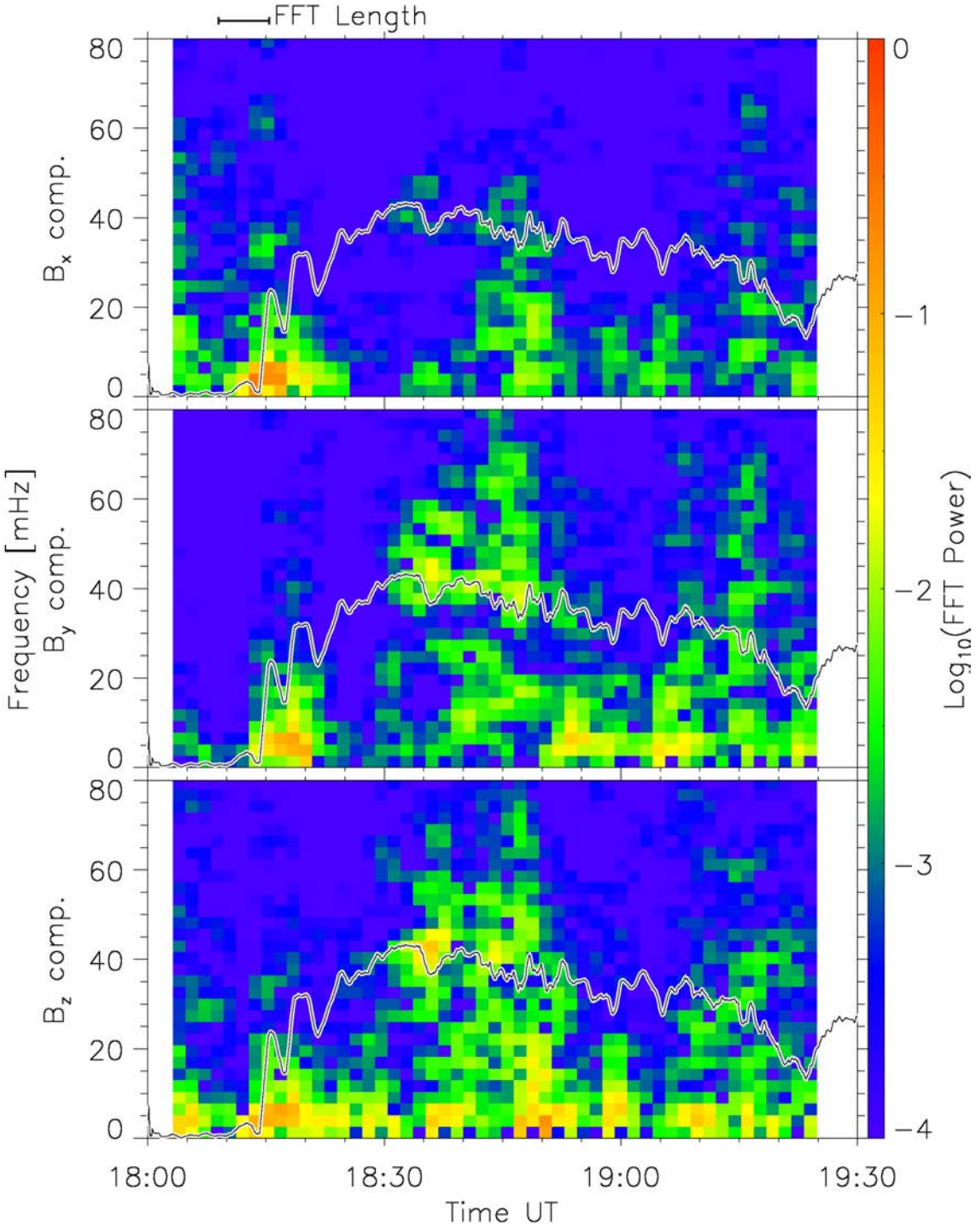

Figure 5.2: Dynamic spectra of the Geotail magnetic field data. The superimposed black line gives the frequency of upstream generated waves predicted by (1.79).

as indicated by the ruler above the top panel in Fig. 5.2. The FFT window was advanced by 32 points between successive spectra. Overplotted on the spectral powers is the frequency f of the upstream generated waves as predicted by Takahashi et al. (1984); see (1.79). A moving average of 20 points length (60 s) was applied to B_{tot} and θ_{xB} before the calculation of f to eliminate short term fluctuations.

Around 1815 UT an increase in power at low frequencies occurred, most notably in the spectrum of the X component. However, this increase was not caused by pulsation activity but due to the step-like feature observed around that time (compare Fig. 5.1).

A strong increase in FFT power between 30 and 70 mHz was observed between 1830 and 1850 UT, a smaller increase followed after 1905 UT. The main increase of wave power was observed while the cone angle was particularly low. The frequency at which most power was observed by Geotail was 40 mHz. This value is well matched by the frequency predicted by (1.79) as shown by the black solid line superimposed on the spectra. All four Cluster satellites, as will be shown in the next section, observed the most power in the compressional component at the same frequency.

Cluster

On 05 September 2002 the four Cluster spacecraft passed through the dayside magnetosphere. Their orbit and magnetic field lines as predicted by the T96 model are shown in the top two panels of Fig. 5.3 in GSM coordinates between 1630 and 2030 UT. The two panels show the projection into the X-Y and X-Z plane, respectively. Standard input parameters ($Dst = 0$ nT, $p_{dyn} = 2.0$ nPa, $B_y = 0$ nT, $B_z = 0$ nT) were used for the field line trace. Every full hour the positions of all four spacecraft are shown, s/c 1 is coloured black, s/c 2 red, s/c 3 green and s/c 4 blue. The dotted

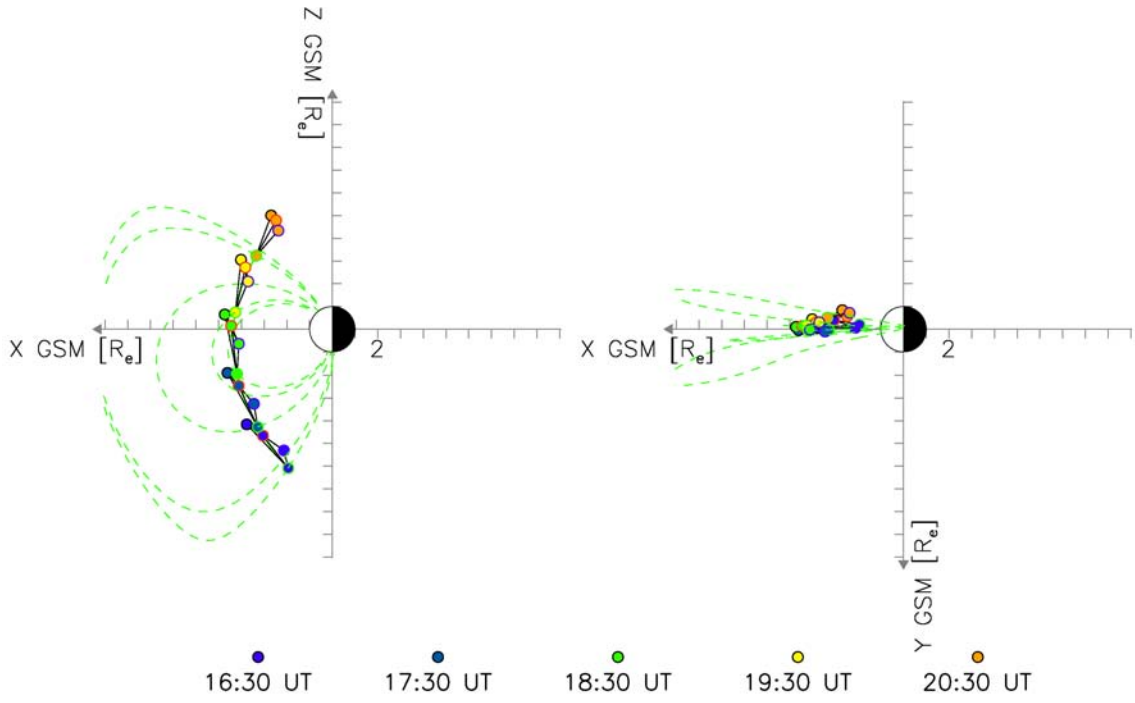

Figure 5.3: The two panels show the orbit of the Cluster satellites.

lines indicate the magnetic field predicted by the T96 model.

The orbit followed essentially the magnetic meridian at 12 MLT as the satellites passed from open field lines connected to the southern polar cap into regions of closed field lines. After having passed through perigee at a geocentric distance of ∼4.5 R_e they then exited the closed dayside magnetosphere and entered open field lines connected to the northern polar cap.

During autumn 2002 the average separation of the spacecraft was about 1 R_e. During the event discussed here it ranged from ∼0.5 R_e between s/c 1 and 2 to 2.5 R_e between s/c 1 and 3. At 1500 UT s/c 1 and 2 led the orbital motion, followed by s/c 3 and 4. As s/c 4 was on the orbit with the smallest perigee it caught up with s/c 1 and 2 by the time these satellites reached the northern cusp region. s/c 3 was lagging behind all other spacecraft throughout the entire interval.

The FGM onboard the Cluster satellites provides the full 3D magnetic field $\vec{B}$ at 4 s (spin) resolution. Additionally, the EFW instrument measured the electric field $\vec{E}$ in the spin plane of the spacecraft.

After the full electric field has been computed (see Sec. 2.1.5), both field time series have been transformed from GSM into the MFA coordinate system as described in Sec. 2.2.2. Here the magnetic field was averaged over 150 points (10 min) to find the mean field direction.

Again, the electric field in the field-aligned direction in the MFA system will be identical zero due to its calculation (see Sec. 2.1.5). Hence only the azimuthal and the radial component of the electric field are shown.

After the data were transformed into the MFA coordinate system the magnitude of the T96 magnetic field model at the spacecraft's position was subtracted from the field-aligned component. Again, standard input parameters (Dst = 0 nT, p_{dyn} = 2.0 nPa, B_y = 0 nT, B_z = 0 nT) were used for the T96 model.

Both magnetic and electric field data were then high pass filtered with a cut-off period of 4000 s. Subsequently a dynamic FFT of length 128 points ($\sim$ 8 min, denoted by the ruler above the top panel in Figs. 5.4 to 5.7) was applied to the three Hamming window tapered time series of each spacecraft. This FFT length results in a frequency resolution of about 2 mHz. Each FFT window was advanced by 32 points (about 2 minutes). The results of the two electric and three magnetic components in the MFA system are shown for the four spacecraft in Figs. 5.4, 5.5, 5.6 and 5.7.

The thick dashed white lines plotted over the dynamic FFTs of the toroidal magnetic and electric field show the frequencies of the six lowest toroidal harmonics as predicted by theory. How these were calculated will be discussed in Sec. 5.3.2.

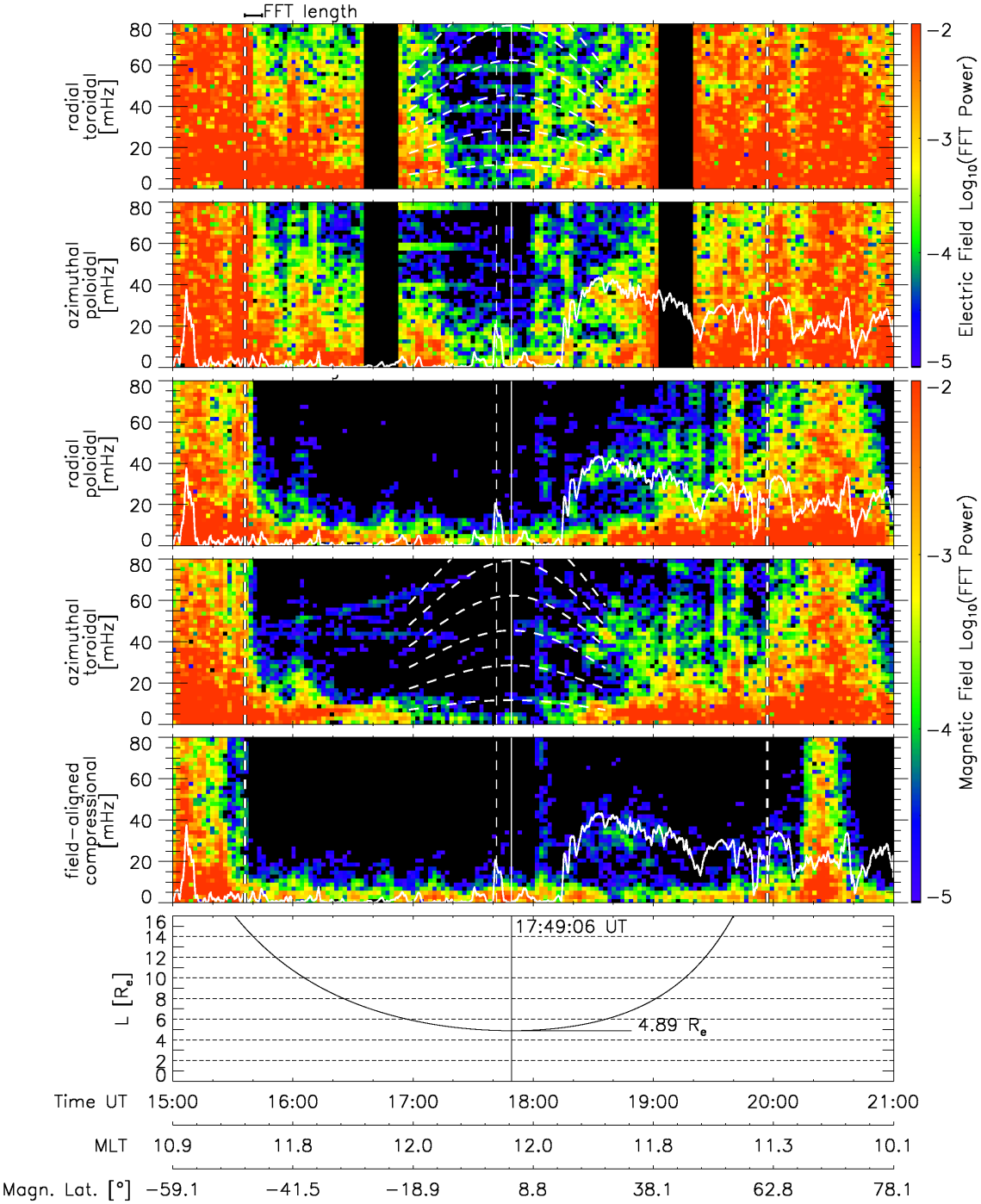

Figure 5.4: Dynamic spectra of the radial, azimuthal electric and radial, azimuthal, field-aligned magnetic field components measured by s/c 1 on 05 September 2002. See text for further explanation.

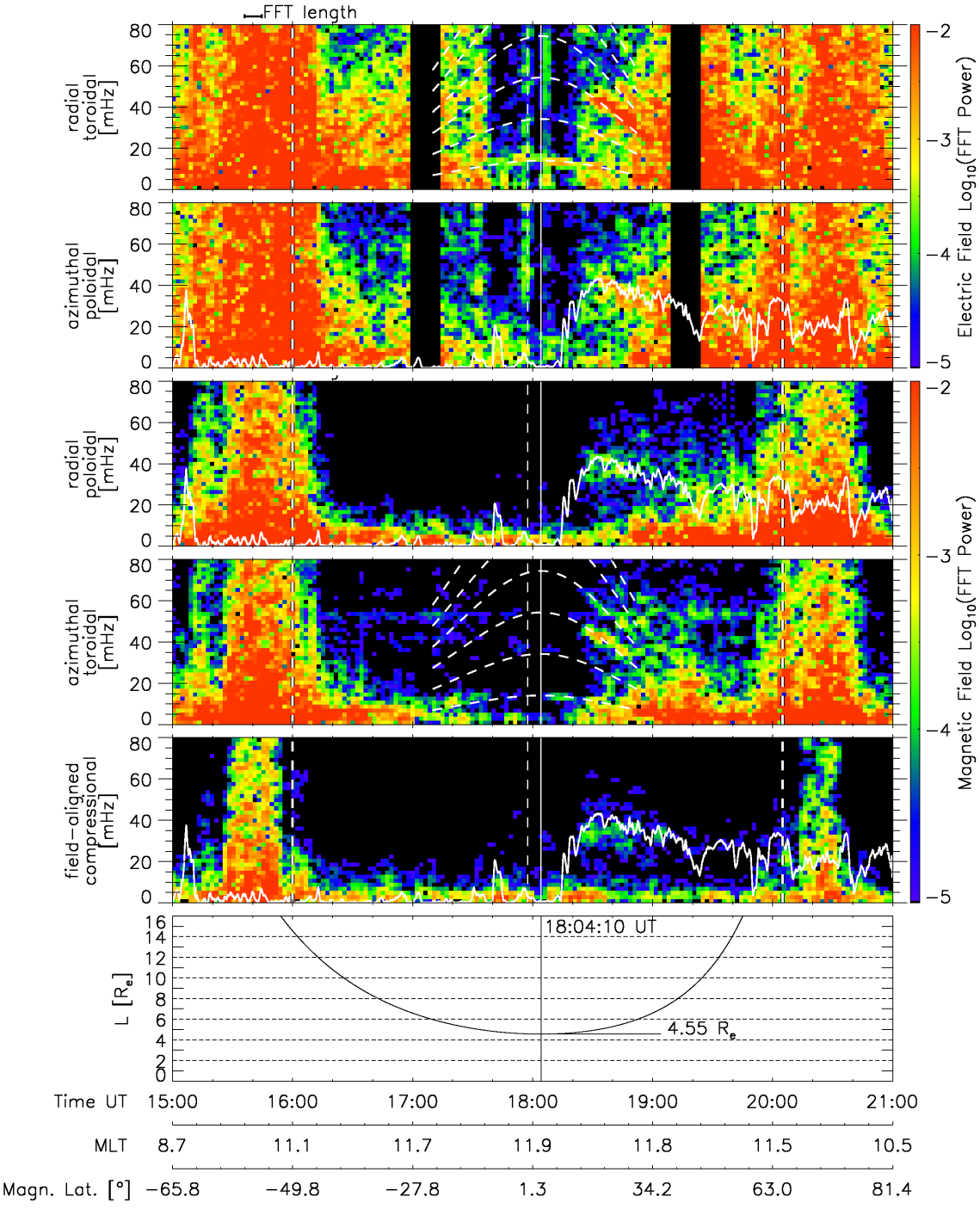

Figure 5.5: Same format as Fig. 5.4, but s/c 2 data on 05 September 2002.

Solid white lines on the spectra of the azimuthal electric, radial and field-aligned magnetic component give the frequency of upstream generated waves as predicted by (1.79).

The bottom panels in Figs. 5.4, 5.5, 5.6 and 5.7 give the spacecraft's L-value. The time of reaching the minimum L-value during the orbit is marked in all panels, the minimum L-value and the time are also given in the bottom panels.

The Open Closed Field Line Boundary (OCB) for all spacecraft was determined from electron energy distribution measurements by the PEACE instrument onboard the satellites. Closed field lines at auroral latitudes, i.e. immediately equatorward of the OCB, are characterised by a trapped population of high energy ($E > 1$keV) electrons (see also Sec. 3.2). This population was easily identified in the PEACE spectrograms during this interval.

Fig. 5.8 shows the differential energy flux (DEF) measured by the PEACE instrument onboard s/c 1 for the inbound crossing of the OCB on 05 September 2002. The three panels show the flux in anti-parallel, perpendicular and parallel direction with respect to the background magnetic field as indicated by the angles in the y-axis annotation.

Two separate electron populations are clearly visible in the data. The low energy population ($E < 1$keV) is typical for open field lines. At 1533 UT a short excursion onto closed field lines can be identified by the appearance of high energy ($E > 1$keV) electrons and the simultaneous disappearance of the low energy population. The final transition onto closed field lines takes place shortly after 1536 UT.

The criterion for an in/outbound boundary crossing was chosen such that the DEF at 10 keV rose/dropped to values above/below 10^{-5} μJ/cm^2 s sr eV. With this rather crude criterion the crossings could be determined to an accuracy of ± 1

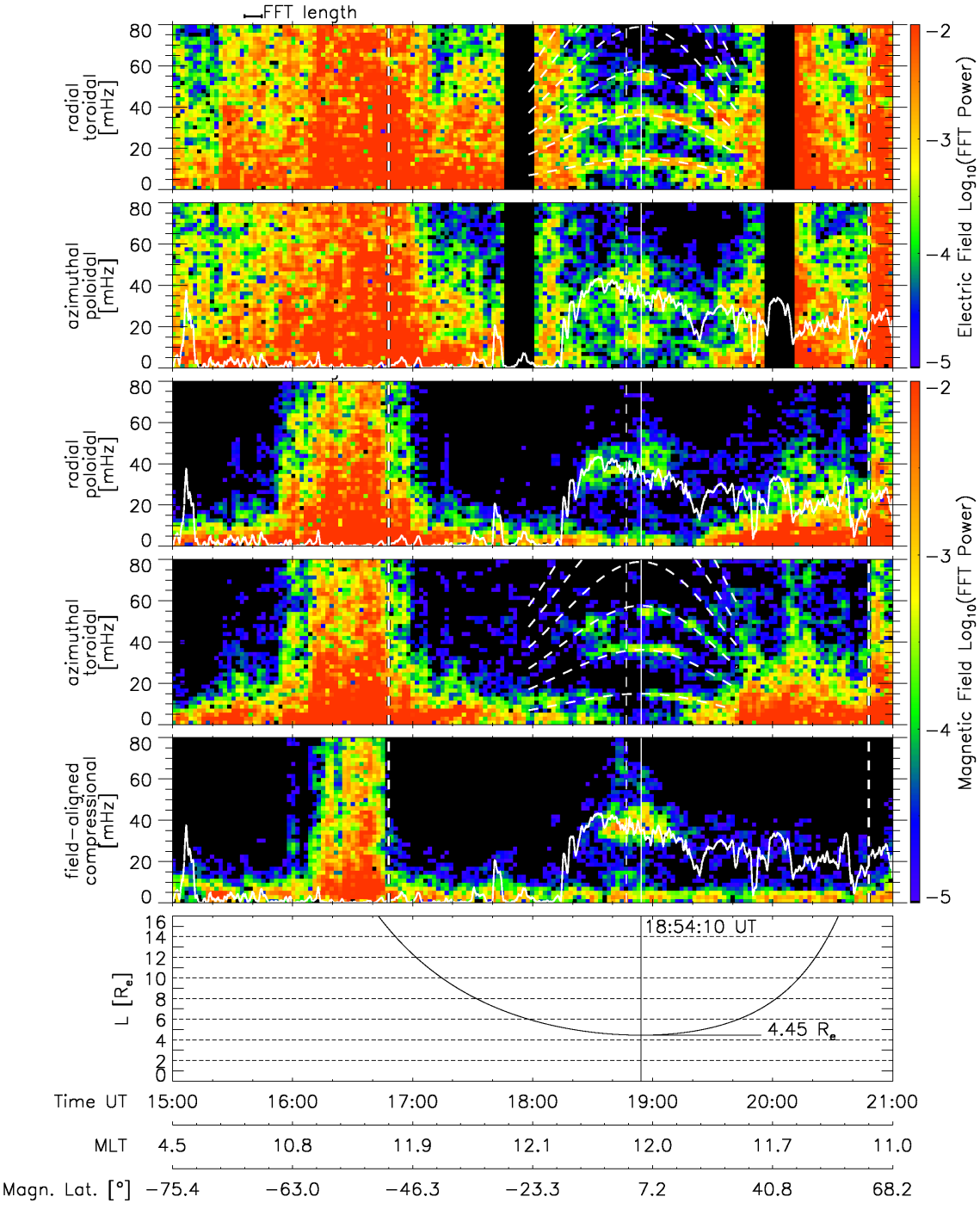

Figure 5.6: Same format as Fig. 5.4, but s/c 3 data on 05 September 2002.

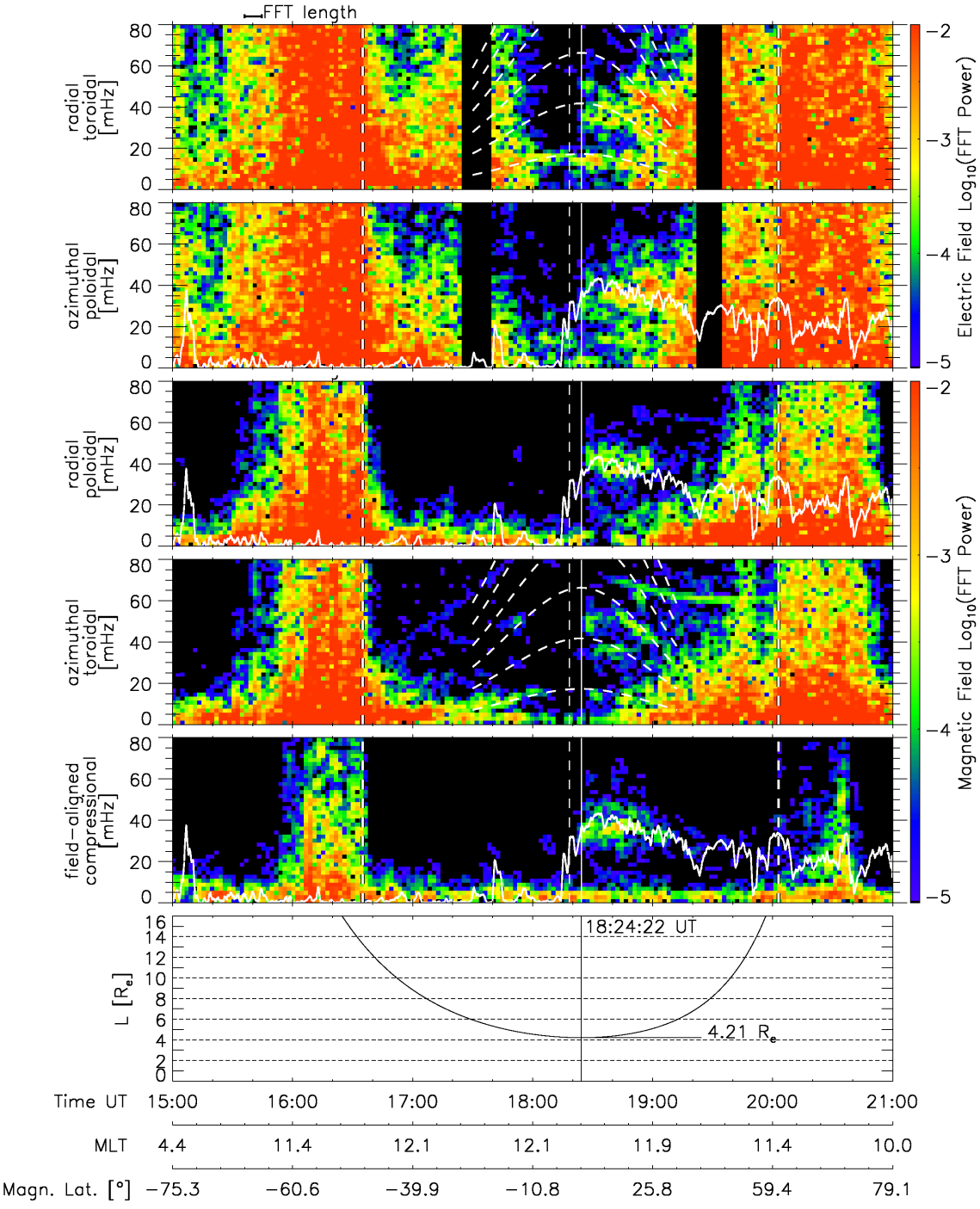

Figure 5.7: Same format as Fig. 5.4, but s/c 4 data on 05 September 2002.

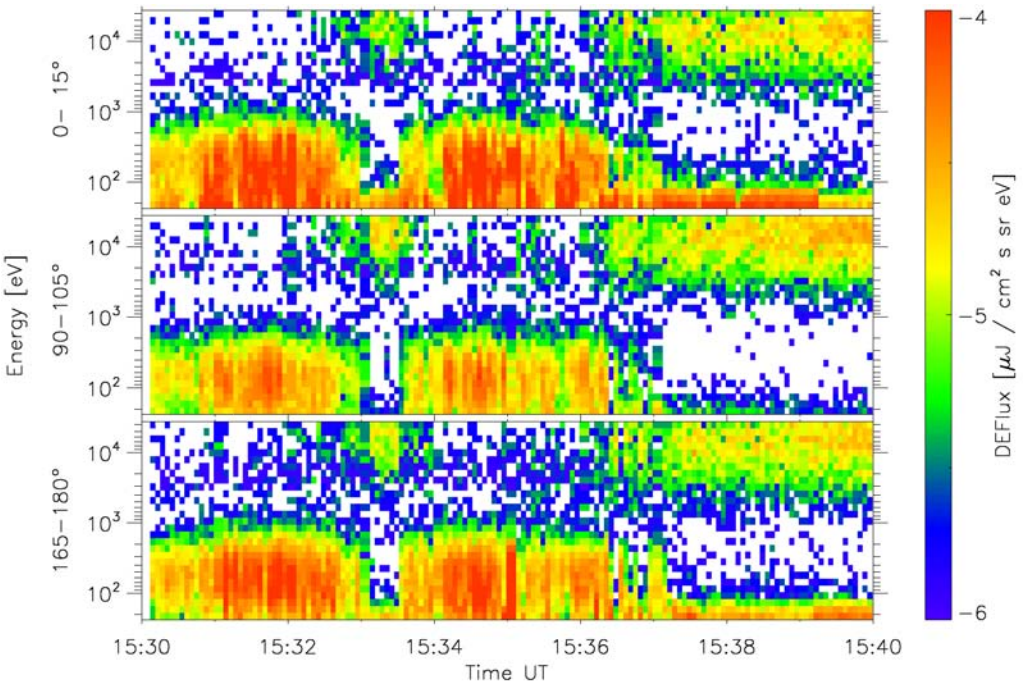

Figure 5.8: Anti-parallel, perpendicular and parallel differential energy flux of electrons measured by the PEACE instrument onboard s/c 1.

minutes which is sufficient for this study.

Before having entered closed magnetic field lines the satellites flew through the cusp region of the magnetosphere. This region is usually characterised by broad band ULF wave activity in magnetic field data (Dunlop et al., 2005). Hence a sharp decrease in wave power in the ULF band can also be used as a criterion for leaving the cusp and entering closed field lines.

s/c 1 was the first satellite to enter closed field lines according to electron DEF data at 1536 UT (compare Fig. 5.8). This time is marked by a vertical dashed line in Fig. 5.4. The crossing was accompanied by a sharp drop in the FFT power above 20 mHz in all three components of the magnetic field. The outbound OCB crossing with reversed characteristics, i.e. sudden increase of ULF broad band power and disappearance of the trapped electron population, occurred at 1957 UT.

The inbound leg of the orbit between 1536 and 1749 UT (perigee) was characterised by very low wave activity between 0 and 80 mHz. In the radial and azimuthal magnetic component two lines of increased power at a constant and a slightly increasing frequency were observed. These are instrumental artifacts and have no physical relevance in this context.

Horizontal lines of increased power at 20, 40 60, and 80 mHz were also observed in both electric field components by s/c 1. These too are instrumental artifacts.

At 1810 UT, shortly after perigee, a simultaneous increase in wave power in the two electric and three magnetic components was observed. The increase is best seen in the compressional magnetic component (last spectrum in Figs. 5.4, 5.5, 5.6 and 5.7). The power was structured in a fan-like fashion in the toroidal magnetic component and, though somewhat less obvious, in the toroidal electric component. The frequency decreased as the L-value increased.

Wave power was also observed in the poloidal and compressional components, however it was unstructured and broad band. Its frequency did not seem to be dependent on the L-value.

As can be seen from the data presented in Figs. 5.4, 5.5, 5.6 and 5.7 the sudden increase in structured and unstructured ULF power was observed by all four spacecraft simultaneously, although being located at different L-values within the dayside magnetosphere.

For all four spacecraft it is true to say that after having entered closed magnetic field lines, the FFT power was at very low values for all three components. FFT power then increased at 1810 UT between 20 and 80 mHz in all components at all spacecraft. Whereas it was broad band and L-value independent in the poloidal component, it was narrow band and L-value dependent in the toroidal component.

The compressional component showed also broad band, L-value independent power which abruptly decreased around 1910 UT.

5.2.2 Ground Magnetometer Observations

During the event stations belonging to the CARISMA and MACCS array of ground-based magnetometers were located at the footprint of the Cluster satellites on the dayside of the magnetosphere around 12 MLT. The footprint of s/c 3 and the positions of the magnetometer stations are shown in geomagnetic coordinates in Fig. 5.9 between 1630 and 2100 UT. The other spacecraft's footprints followed the trace of s/c 3 very closely and are not shown for the sake of clarity. The statistical location of the auroral oval (Feldstein and Starkov, 1967) for the prevailing geomagnetic conditions ($Kp = 1$) is superimposed in light grey for reference. Positions of magnetometer stations belonging to the CARISMA and MACCS chain are also shown.

Dynamic spectra were calculated from available data of ground-based magnetometers. Before a FFT of about five minutes length was applied, the otherwise unfiltered data were reduced by a linear trend and multiplied by a Hamming taper. Each FFT window was advanced by 32 points (two and a half minutes). The logarithm of the FFT power of the X component (geographic North-South) is shown in Fig. 5.10.

Between ∼1820 and ∼1920 UT an increase in wave power at frequencies between 20 and 80 mHz was observed at all stations except CRV. This is in the same frequency range as power was observed at the Cluster spacecraft and the Geotail satellite. The observed power varied with latitude whereas the peak frequency where most power was observed was constant around 40 mHz. The agreement between this frequency and the frequency predicted by (1.79) is, as before for Geotail and Cluster observations, very good. The onset time was more distinct than the end time. After

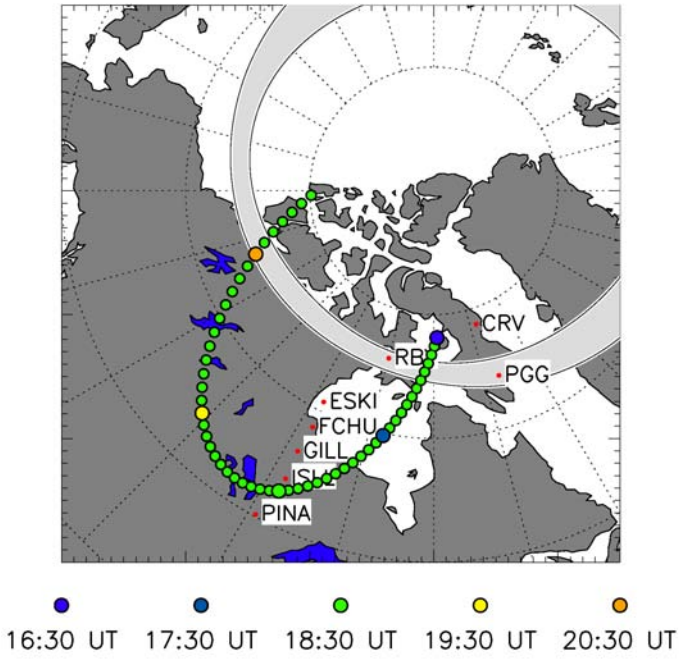

Figure 5.9: The figure shows the footprint of s/c 3 over Northern America. See text for further explanation.

∼1930 UT another increase in wave power at lower frequencies was observed.

The dynamic spectrum for data recorded at CRV shows no signatures of an increase in wave power between 20 and 80 mHz. This is most likely due to the fact that CRV was located on open field lines. The poleward boundary of the auroral oval as indicated in Fig. 5.3 can be taken as a proxy for the OCB and hence CRV was located on open field lines. Additionally, s/c 3 crossed the OCB around 1645 UT (see Fig. 5.6). According to the footprint predictions using the T96 model, this position matches well with the location of the poleward boundary of the auroral oval.

The fact that CRV did not observe any increase in wave power on open field lines strengthens our argument that upstream generated waves entered the closed dayside magnetosphere.

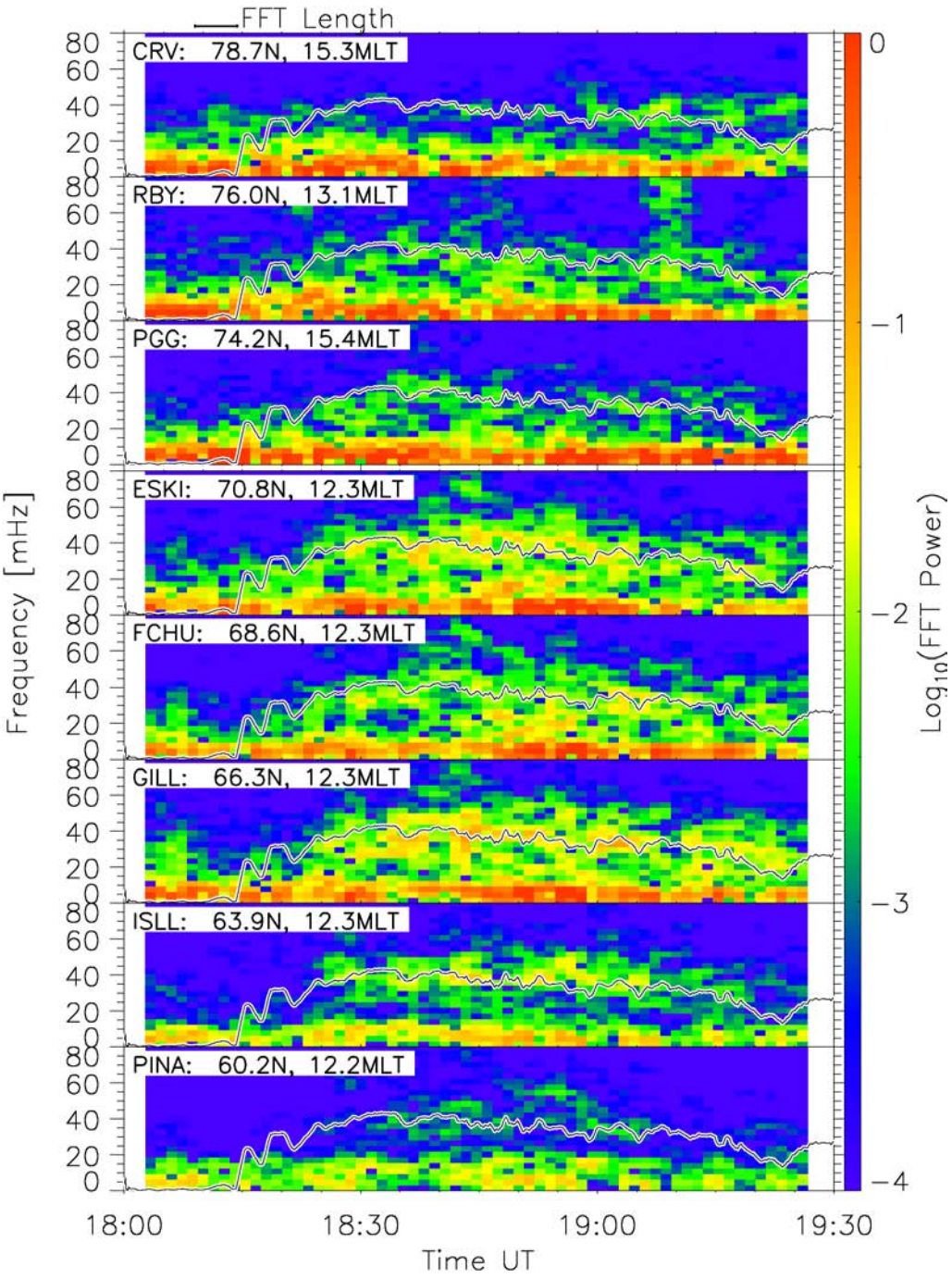

Figure 5.10: Dynamic spectra of X component data from some ground-based magnetometer stations belonging to the CARISMA and MACCS array in Canada on 05 September 2002. The station's name, magnetic latitude and MLT are given in the top left corner of each panel. Also shown as a solid black line is the predicted frequency of the upstream generated waves as given by (1.79).

5.3 Discussion

As outlined in the introduction, the connection between the IMF cone angle and pulsation power in the ULF frequency range in the dayside magnetosphere is theoretically well understood (Troitskaya et al., 1971). During times of low IMF cone angle solar wind ions are reflected at the bow shock. These backstreaming ions generate waves in the solar wind by a cyclotron resonant interaction (see Sec. 1.2.6). Since the wave propagation speed is lower than the solar wind speed they are convected with the bulk solar wind flow towards Earth, passing the bow shock and magnetopause without significant changes to their spectrum. From the dispersion relation of MHD waves it is obvious that only the compressional waves will enter the inner dayside magnetosphere.

From Figs. 5.4 to 5.7 it is clear that the power in both the poloidal and compressional components of the magnetic and electric was broad band whereas it was focused in bands in the toroidal component. The clearest observations were provided by data from s/c 3 in Fig. 5.6.

Our interpretation is that due to favourable conditions broad band compressional waves were generated by backstreaming ions upstream of the bow shock and entered the dayside magnetosphere. Here they mode convert into narrow band field-guided Alfvén waves, creating an Alfvénic continuum.

5.3.1 Field-Aligned Component

The sudden decrease in the IMF cone angle occurred at 1814 UT. Before 1824 UT two brief excursions to larger cone angles occurred; the first 1817 UT, the second at 1822 UT. To establish when compressional wave power was observed by the Cluster spacecraft, a dynamic FFT with a length of 32 points - a quarter of the length used

to create Figs. 5.4 to 5.7 - was calculated. Subsequently all power between 20 and 80 mHz was integrated to give a time series of the wave power. This time series is shown for the four satellites in Fig. 5.11.

Fig. 5.11 shows that the compressional power in the magnetic field measured by the spacecraft arrived in wave packets rather than as continuous pulsations, as has been observed before by Chi and Russell (1998) and Clausen et al. (2008). Some prominent wave packets have been marked with vertical dashed lines. These show that all packets were simultaneously observed by all spacecraft, even though their position within the dayside magnetosphere, i.e. their L-value, was significantly different (see top panel in Fig. 5.11).

The amplitude of the wave packets seems to be controlled by a convolution of two factors. As the IMF cone angle dropped to values below 10°, the amplitude of the observed wave packets was higher. Secondly, the position within the magnetosphere controlled the amplitude: the closer the satellite was to the equatorial plane the larger the observed amplitude.

Fig. 5.11 also reveals that the boundaries of the interval of enhanced power were controlled by time and not by spacecraft position. At the end of the interval after 1905 UT s/c 3 observed no compressional power at L-values between 4 and 5. However, earlier between 1830 and 1900 UT all other spacecraft had observed power at these L-values.

The first significant compressional power to be registered by the Cluster magnetometers started at 1824 UT, i.e. 10 minutes after the drop in the IMF cone angle was observed by the Geotail satellite. The delay time between the change in cone angle and the occurrence of wave power is due to two factors: (1) the propagation of the change in IMF with the solar wind from the Geotail position to the bow

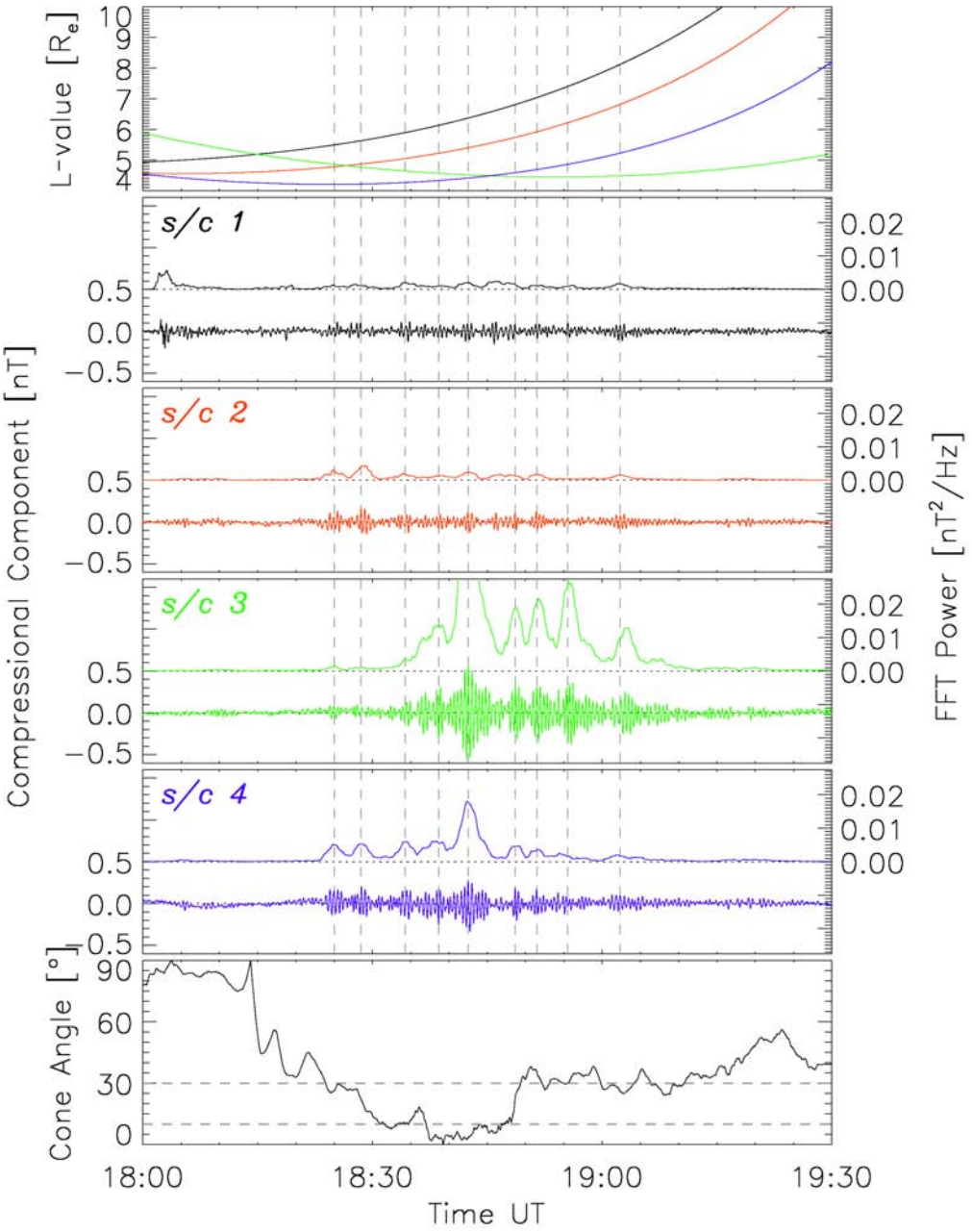

Figure 5.11: Wave power in the compressional magnetic component between 20 and 80 mHz observed by the Cluster satellites (panels labeled s/c 1 to s/c 4) on 05 September 2002. The right y axes give the magnitude of the integrated power. The filtered time series of the compressional magnetic field component is shown relative to the y axes on the left. The top panel shows the spacecraft's L-value. The bottom panel shows the IMF cone angle.

shock and (2) the traversal of the magnetosheath by the generated waves with the magnetosheath flow, since it can be assumed that the first waves to arrive at Cluster were those generated immediately upstream of the bow shock.

The convection time τ_{sw} of the IMF from the Geotail position r_{gt} to the position of the subsolar bow shock r_{bs} can simply be calculated via $\tau_{sw} = (r_{gt} - r_{bs})/v_{sw}$.

The ACE satellite measured the solar wind speed during this event. After lagging the data by an appropriate delay due to the propagation of the solar wind, v_{sw} can be estimated to be ∼430 km/s during the event discussed here. The geocentric bow shock distance r_{bs} was 15.0 R_e according to results from Peredo et al. (1995). This allows us to estimate τ_{sw} to be 3 min.

Khan and Cowley (1999) argued that the transition time of the solar wind through the magnetosheath τ_{sh} can be estimated by

$$\tau_{sh} = \frac{r_{bs} - r_{mp}}{\kappa\, v_{sw} - v_{mp}} \ln\left(\frac{\kappa\, v_{sw}}{v_{mp}}\right), \tag{5.1}$$

where v_{sw} is the solar wind bulk plasma speed and r_{mp} denote the magnetopause standoff distance. v_{mp} is the plasma bulk speed at the magnetopause which Khan and Cowley (1999) argued to be 20 km/s. κ is the ratio of the flow speed just downstream and just upstream from the shock, i.e. v_{bs}/v_{sw}. This ratio follows from the usual shock jump conditions as

$$\kappa = \frac{(\gamma - 1)M_s^2 + 2}{(\gamma + 1)M_s^2} \tag{5.2}$$

where M_s is the sonic Mach number (see Sec. 1.1.3) and $\gamma = 5/3$.

Following Shue et al. (1997) the position of the magnetopause r_{mp} was 11.0 R_e. As the solar wind speed is known to have been 430 km/s, the estimated transition time

τ_{sh} of the compressional waves from just upstream the bow shock into the dayside magnetosphere is then about 9 minutes.

Adding τ_{sw} to τ_{sh} we arrive at a total delay time of 12 minutes, which is in excellent agreement with the observed 10 minutes delay between the change in IMF cone angle and the onset of compressional wave power observed by the Cluster satellites.

5.3.2 Azimuthal Component

In the preceding section we have shown that the compressional power observed by the Cluster satellites was generated by backstreaming ions. We will now show that the compressional waves mode-converted into toroidal Alfvén waves, generating Alfvénic continuum.

As the satellites move from large to a minimum L-value on their inbound pass, the fundamental eigenfrequency of the crossed field lines increases. Once the perigee is passed, the field line length increases and hence the fundamental eigenfrequency decreases.

Schulz (1996) derived an analytic expression for the frequencies of toroidal eigenmodes from numerical solutions of the wave equation. According to Schulz (1996) the frequency ω_n of the n^{th} harmonic of the toroidal mode on a dipolar field line with a certain L-value and plasma mass density exponent, α, is given by

$$\omega_n(L,\alpha,n) = \frac{3\pi}{8}\frac{v_{A0}(L)}{L\,a}\frac{1}{\sin\Lambda(L)} + \left(n-\frac{3}{4}\right)\Delta\omega(L,\alpha) \tag{5.3}$$

where $v_{A0}(L) = B_0(L)/\sqrt{\mu_0\rho_0(L)}$ is the equatorial Alfvén velocity, a is the Earth's radius and $\Lambda(L)$ is the colatitude where the field line of interest intersects the Earth. The exponent α determines how the mass is distributed along the field line, as given

in the previous chapter by (4.3).

The increment of the frequency $\Delta\omega(L,\alpha)$ is independent of the harmonic number n and given by

$$\Delta\omega(L,\alpha) = 2\pi \left[\oint \frac{ds}{v_A(L,\alpha)}\right]^{-1} \tag{5.4}$$

. The travel time integral in (5.4) can for a dipolar magnetic field be expressed as

$$\oint \frac{ds}{v_A(L,\alpha)} = 4\,\frac{L\,a}{v_{A0}(L)}\,\int_0^{\sin\Lambda(L)} \left(1-x^2\right)^{(3-\alpha/2)}\,dx. \tag{5.5}$$

The equatorial Alfvén velocity depends on the equatorial mass density $\rho_0(L)$ and the equatorial magnetic field $B_0(L)$. $\rho_0(L)$ was taken to have the same dependency as in the previous chapter, see (4.2), only here we chose to call the dependent variable L instead of r.

The equatorial magnetic field $B_0(L)$ can be assumed to be dipolar and depending on a reference point. The perigee of s/c 3 was chosen as the reference point (L_0 = 4.45 R_e, B_{ref} = 310 nT) such that the magnetic field along the L-values can be modelled as

$$B_0(L) = B_{ref}\left(\frac{L_0}{L}\right)^3. \tag{5.6}$$

For calculations using the above model, the knowledge of the position of the plasmapause is essential. Fig. 5.12 shows electron densities deduced from spectra provided by the WHISPER instrument (see Sec. 2.1.5), where the quality flag was bigger than 33.

From Fig. 5.12 it is clear that none of the spacecraft entered the plasmasphere.

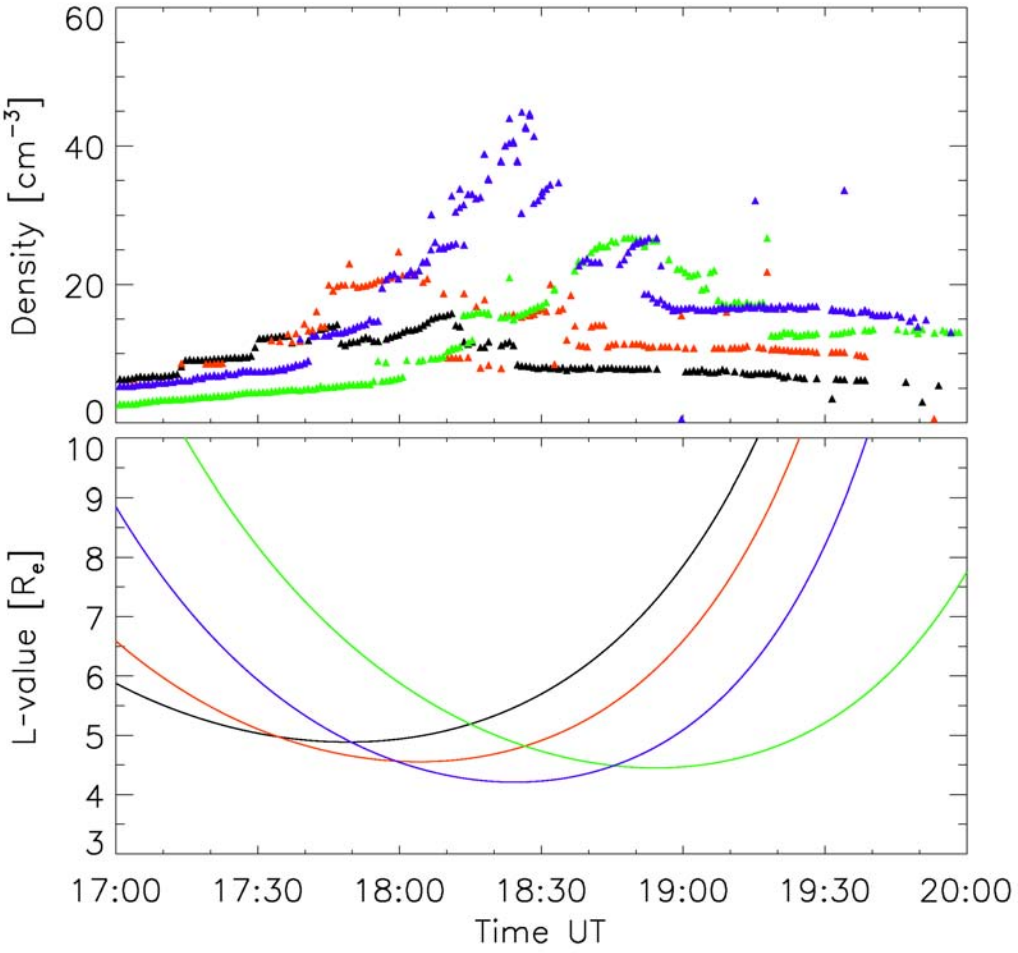

Figure 5.12: Electron densities determined from the spectra provided by the WHISPER instrument between 1700 and 2000 UT on 05 September 2002. The bottom panel shows the L-value for reference. Different spacecraft are again coded by different colours (see Fig. 5.11).

The plasmapause position was therefore set to $L = 4$ R_e as it will not further affect the model calculations. Analogous to the model magnetic field, the perigee of s/c 3 was chosen as the magnetospheric reference point for the number densities ($L_{mp} = 4.45$ R_e, $n_{ms} = 25$ cm^{-3}).

Using (5.3) the frequencies of the lowest six harmonics of the toroidal mode were determined for every L-value along the orbit of the Cluster satellites for an exponent of $\alpha = 2$ (Denton et al., 2002). The average mass per particle was chosen to be 1.15 amu. This density value produced a best match between the predicted frequencies and the frequencies at which most wave power was observed in the radial electric field at the closest approach of s/c 3.

The frequency values are overplotted on the spectra of the toroidal field components in Figs. 5.4 to 5.7 and show excellent agreement with the observations.

Note that one can even make some general remarks about the node structures of the harmonics from the spectra. The fundamental toroidal mode has a node in the magnetic field at the magnetic equator. The spectrum of s/c 3 shows this characteristic by a decrease in wave power close to the perigee of the orbit. The second harmonic has an antinode in the equatorial plane which is observed as increased wave power around perigee at s/c 3. The node structure is far less obvious in the toroidal component of the electric field.

This node structure was not observed by the other spacecraft because they had already passed the equatorial plane by the time the Alfvénic continuum started.

To further support our observations, the fundamental eigenfrequencies of the field lines half way between magnetically conjugate ground-based magnetometer stations belonging to the CARISMA chain have been calculated using the cross-phase technique as described in Sec. 2.2.1.

Station pair	Lat. [°]	Lon. [°]	L [R_e]	f [mHz]
PINA ISLL	62.0	332	4.5	13
ISLL GILL	65.1	332	5.6	7.5
MCMU RABB	65.7	313	5.9	6.5
MCMU FSMI	65.9	307	6.0	6.5
GILL FCHU	67.4	332	6.8	6.5
FCHU RANK	70.5	334	9.0	4.0

Table 5.1: Locations in magnetic coordinates and L-value of stations belonging to the CARISMA chain.

According to the prediction in Fig. 5.9 the footprint of s/c 3 during perigee was located very close to the field line half way between PINA and ISLL. Hence the frequency of the lowest harmonic measured by both instruments should be very similar.

The fundamental eigenfrequency of that field line was indeed about 13 mHz according to the cross-phase analysis based on ground-based data (see Tab. 5.1). According to measurements of s/c 3 and the predictions of our model calculations, the fundamental eigenfrequency at perigee at 1854 UT was 15 mHz (see Fig. 5.6).

The ground-based magnetometer data has been checked for signatures of FLRs which would be expected since the Cluster measurements show the existence of Alfvénic continuum on the field lines conjugate with the magnetometer stations. FLR signatures would be expected to occur with a frequency of 13 mHz and a resonance latitude around that of PINA and ISLL. However, no pulsations with FLR characteristics were found.

The pulsations belonging to the Alfvénic continuum had a rather small amplitude when observed by the Cluster satellites. Ionospheric screening probably prevented these oscillations to be observed on the ground.

5.3.3 Upstream Waves at Geotail

The observations discussed earlier raised the question why Geotail did not observe upstream waves from the moment the change in IMF direction hit the bow shock. According to earlier calculations the upstream wave generation started 3 minutes after the sudden positive turning in the IMF B_x component was measured by Geotail at 1814 UT. However upstream waves are only observed at the Geotail position from 1830 UT onwards, also ending significantly earlier (around 1848 UT) than when the compressional power stopped being detected by Cluster (around 1910 UT).

The above observations can be explained when looking at the configuration of the Geotail position, the IMF and the bow shock.

The ions reflected from the bow shock will essentially travel along the IMF field lines against the solar wind stream. Hence upstream waves will only be observed by Geotail if an IMF field line stretched from the spacecraft's position to the bow shock. Moreover, at the foot point of that field line on the bow shock boundary the condition for ion reflection must have been fulfilled. Whenever the angle between the field line from Geotail to the bow shock surface and the normal of the bow shock at the foot point was below 30° upstream waves are expected at the Geotail position.

As the IMF changed with time, the foot point of the magnetic field through the Geotail position moved over the bow shock surface or in fact may not have crossed the surface at all. Additionally the angle between the IMF and the shock normal at the foot point changed. This condition controlled whether upstream waves were observed at the Geotail satellite.

In order to test this hypothesis, the angle θ_{nB} between the IMF direction through Geotail's position $\hat{\vec{x}}_{\mathrm{IMF}}$ and the shock normal $\hat{\vec{n}}$ at the point where $\hat{\vec{x}}_{\mathrm{IMF}}$ crossed the bow shock surface was calculated.

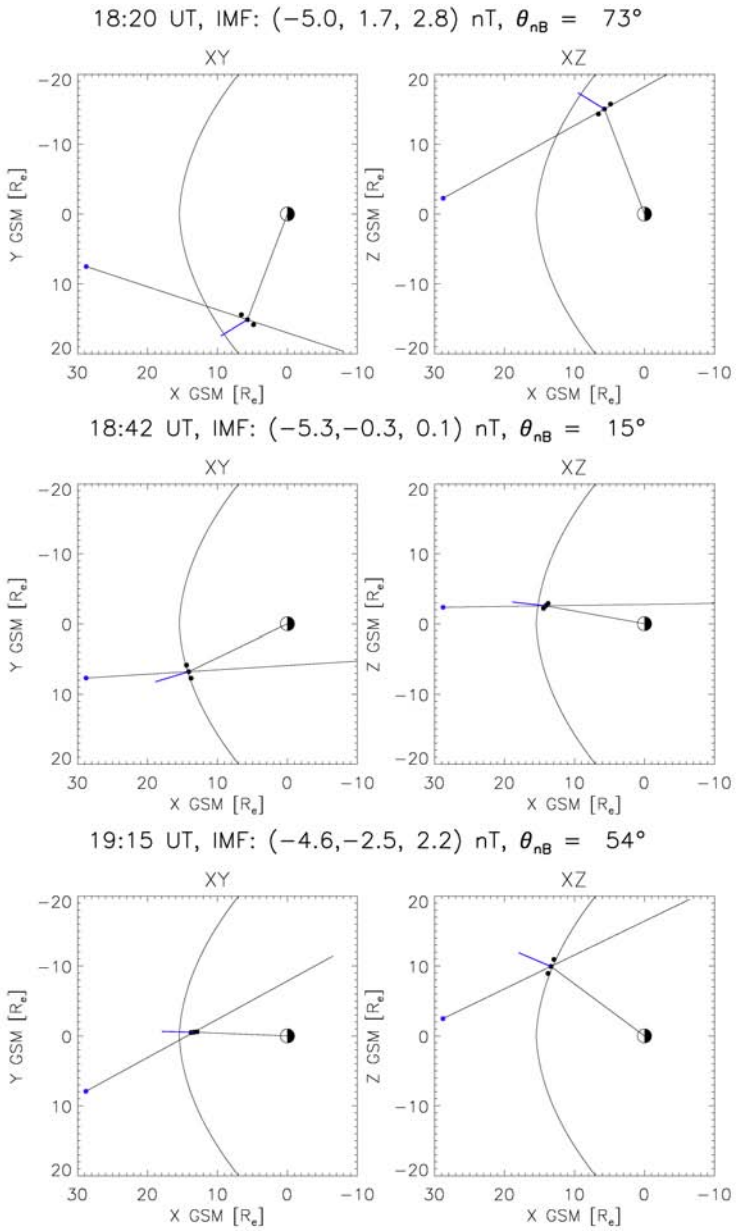

Figure 5.13: Geometry for different IMF orientations at different times on 05 September 2002. The blue dot on the left marks the position of the Geotail satellite, the black line emanating from that position is the IMF direction. The black dots represent the points on the bow shock surface from which the normal direction was calculated. The normal direction is shown in blue. Also shown is the bow shock surface in the respective plane and the position vector of the crosspoint and Earth.

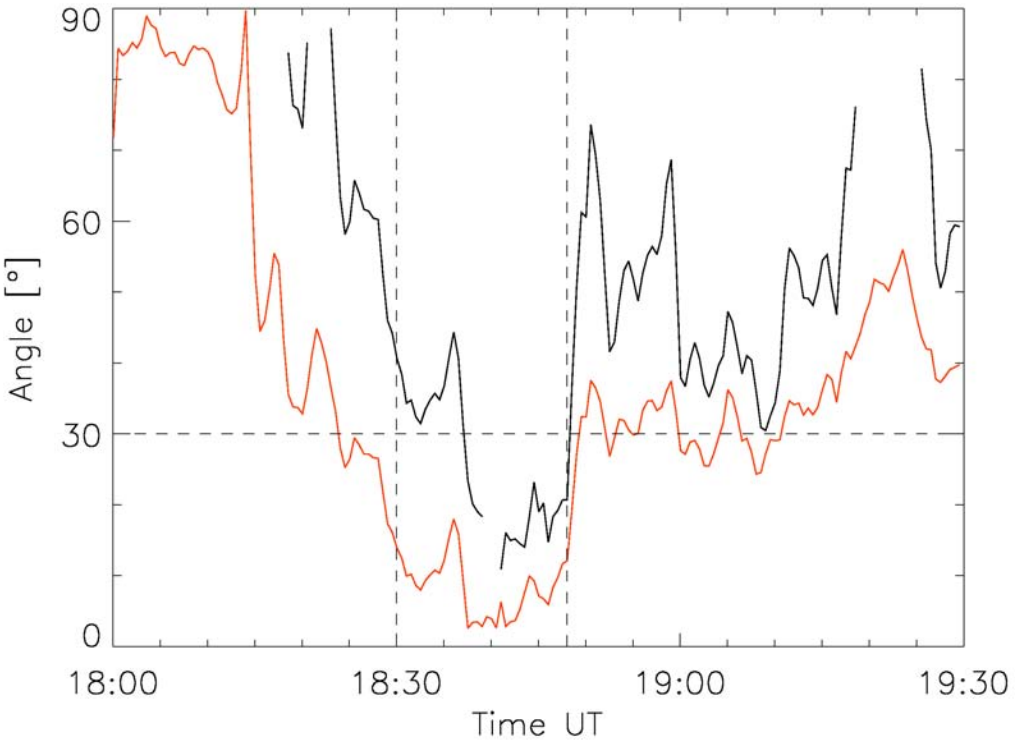

Figure 5.14: The black trace shows the angle θ_{nB} between the IMF connected to the Geotail position and the normal of the bow shock surface at the crossing point of the two. The red trace shows the IMF cone angle θ_{xB}.

Peredo et al. (1995) gives a quadratic form to describe the shape of the bow shock depending on the Alfvénic Mach number. The point at which $\hat{\vec{x}}_{\mathrm{IMF}}$ crosses the bow shock is thus easily found. From other points on the bow shock surface in the vicinity of the crosspoint the normal vector $\hat{\vec{n}}$ and hence the angle θ_{nB} can be determined. This method is schematically shown in Fig. 5.13 at different times.

In the discussion of the compressional wave power observed by the Cluster satellites it was shown that the generation of upstream waves at the subsolar point started with the sudden decrease in cone angle observed by Geotail at 1815 UT; see red trace in Fig. 5.14. However the MAG instrument did not observe significant wave power before 1830 UT, as marked by the vertical dashed line in Fig. 5.14.

As can be seen from Fig. 5.14, the observation of wave power at Geotail at 1830 UT coincides with the drop of θ_{nB} (black trace in Fig. 5.14). Also, the wave power decreases suddenly at 1848 UT when θ_{nB} changed to values above 30°. Only between these times was the IMF orientated in such a way that the backstreaming ions would travel in the direction of Geotail. Thus waves could be generated further upstream of the satellites position and subsequently observed by the MAG instrument onboard Geotail.

5.4 Conclusions

On 05 September 2002 an increase in the IMF B_x component caused a sudden decrease of the IMF cone angle below 30°. After the change in the IMF had propagated to the bow shock, the generation of waves due to reflected ions began.

10 minutes after the change in the IMF cone angle was measured by the Geotail satellite a sudden increase in compressional wave power with a peak frequency of 40 mHz in the dayside magnetosphere was registered by the Cluster satellites. We show that this delay is consistent with the propagation of the IMF from the Geotail position to the bow shock and the subsequent propagation of upstream generated waves from there through the magnetosheath into the dayside magnetosphere.

Cluster magnetic field data shows that simultaneously with the increase in compressional wave power, the dynamic spectra of the azimuthal magnetic and radial electric field components show the presence of Alfvénic continuum oscillations. Hence we provide strong evidence for the direct driving of the Alfvénic continuum in the dayside magnetosphere by upstream generated waves.

An increase in wave power at 40 mHz is also seen in data from ground-based magnetometers which were magnetically conjugate with the Cluster satellites during the event. The observed frequency of the lowest harmonic observed by s/c 3 at perigee is consistent with calculations of the fundamental eigenfrequency of the involved field line using ground-based data. However, no FLR signatures were found on the ground as would be expected from the existence of the Alfvénic continuum.

The dipole based, toroidal FLR solution of Schulz (1996) was found to accurately predict the toroidal eigenfrequencies of the field lines crossed by the Cluster satellites. This is true for both the magnetic and electric field. Due to the polar orbit of the Cluster satellites, node structures of the Alfvénic continuum were observed.

The magnetometer onboard Geotail registered wave activity significantly after the change in the IMF cone angle had reached the bow shock. We explain this observation by showing that only during this later interval was the IMF orientated in such a way that reflected ions could propagate beyond the position of Geotail.

6 Summary and Conclusions

In the previous three chapters detailed studies of ULF waves in the Earth's magnetosphere using data from a broad range of instruments were presented. As Cha. 3 is concerned with artificial ULF waves as opposed to naturally occurring waves in Chas. 4 to 5, the conclusions have been split into two parts accordingly.

6.1 Summary I

Cha. 3 presented an analysis of wave activity resulting from an ionospheric heating experiment. The SPEAR facility was operated in a 5 minutes on-off cycle, pumping electromagnetic energy into the ionosphere. Theory then predicts that, in the time span of a few seconds, the electron density increases in the heated patch which, in turn, leads to a reduced resistivity of the plasma. If a DC current is present in the ionosphere, modulated heating superimposes an AC component on the background current. The heated patch hence acts like a giant antenna, emitting waves at the modulation frequency.

During the event presented in Cha. 3, ground-based magnetometers indeed registered a pulsation at the modulation frequency. Furthermore, the observed pulsations were not only confined in space, i.e. observed only in data from magnetometers in the vicinity of the heating facility but also in time, i.e. wave power at the modulation frequency was only present during the time of the heating experiment.

As the heating facility was in the presented case operating on open field lines, the solar wind was checked for wave activity at the modulation frequency. Some wave power was found at the frequency in question which could have travelled down open field lines and resulted in signatures similar to those observed. However, the temporal and spatial confinement of the observed wave power on the ground leaves little doubt that it was a direct result from the heating activity.

Cha. 3 presented the analysis of the first successful wave injection experiment at ULF frequencies by the SPEAR system. Furthermore, it is the first report of a successful modulation experiment on open field lines.

6.2 Outlook I

Several aspects could be explored outgoing from the presented results. Given a number of successful modulation experiments on open and closed field lines, an evaluation of the differences in the responses to the two situations would be very interesting. As modulation experiments with SPEAR are always scheduled such that the footprint of the Cluster satellites is in the vicinity of Svalbard, a study highlighting observations of the injected wave in space would provide information about how such a wave behaves while propagating.

Furthermore, a comparative study of modulation results from the high-latitude SPEAR system and other, low-latitude heaters could yield interesting insights into how the ionosphere affects the results of such experiments.

6.3 Summary II

Waves generated upstream of the bow shock are the combining theme of Chas. 4 and 5. In Cha. 4 we investigate the propagation of such waves through the dayside magnetosphere into the tail. Over two dozen ground-based magnetometers located in the dusk and dawn flank as well as the dayside observed five wave packets. The onset of the pulsation activity is shown to correlate accurately with the turning of the IMF to low cone angles which makes the upstream wave generation mechanism the most likely explanation for their occurrence.

The propagation of one individual wave packet is modelled along the "Tamao-path" and the predicted onset times at the various ground-based magnetometer stations are found to be in excellent agreement with the observed delays.

Using the cross-phase technique, the fundamental eigenfrequency of the field lines connected to the magnetometer stations were determined. Where the frequency of the driving pulsation matched the local fundamental eigenfrequency, the signature of a FLR was observed on the ground, indicating that the incoming compressional wave converted locally to a resonant standing Alfvén wave on that field line. We found even some indications for this mechanism being at work at latitudes where the driving frequency matched that of the local second harmonic.

Two Cluster satellites observed the wave packets and due to their fortunate positioning above and below the magnetic equator the node structure of the pulsations could be analysed. As the Cluster satellites were however not located at the resonant L-value, the node structure seemed to lie between that of a first and second harmonic.

Instead of tracing the propagation of single wave packets through the magnetosphere, the third case study in Cha. 5 discussed the Alfvénic continuum that is generated by upstream generated waves in the dayside magnetosphere.

The Geotail satellite observed a drop in the cone angle of the IMF to values below 30° which is considered the threshold below which the generation of waves by backstreaming ions is initiated.

In good timing agreement with the drop in cone angle the Cluster satellites observed the onset of Alfvénic continuum in the dayside magnetosphere at several harmonics both in the magnetic and electric field. Concurrently ground-based magnetometers observed an onset in wave power.

Several minutes after the change in cone angle to values below 30°, the IMF direction changed again with the cone angle dropping to values below 10°. After this change waves were observed by the magnetometer onboard Geotail. We are able to show that the change in IMF geometry meant that ions were now able to propagate upstream past the position of Geotail and generate waves which were then convected with the solar wind flow downstream to the position of Geotail. This fortunate constellation of spacecraft allowed the simultaneous detection of upstream generated wave activity in solar wind, magnetosphere and on the ground for the first time.

6.4 Outlook II

Future work could investigate how common driving at harmonics of the fundamental field line eigenfrequencies is and whether that would have implications for the distribution of wave power through the magnetosphere.

The wave mode analysis also suggested odd boundary conditions between the North and South hemisphere. A future study could look into whether such asymmetry is common and whether that suggests that node structures are really more complicated than simple models imply. Additionally one could investigate whether similar observations can be seen for other ULF wave modes.

6.5 Concluding Remarks

Several aspects of ULF waves in the Earth's magnetosphere were presented in detail in this thesis. Not all observations could be explained entirely, however the general picture for each of the three presented events is clear. By explaining several features

we hope to have broadened our understanding of fundamental plasma processes occurring in the near space environment of Earth.

Bibliography

Arthur, C. W. and McPherron, R. L.: Interplanetary magnetic field conditions associated with synchronous orbit observations of Pc3 magnetic pulsations, Journal of Geophysical Research, 82, 5138–5142, 1977.

Balogh, A., Carr, C. M., Acuña, M. H., Dunlop, M. W., Beek, T. J., Brown, P., Fornaçon, K.-H., Georgescu, E., Glassmeier, K. H., Harris, J., Musmann, G., Oddy, T., and Schwingenschuh, K.: The Cluster Magnetic Field Investigation: Overview of In-Flight Performance and Initial Results, Annales Geophysicae, 19, 1207–1217, 2001.

Baransky, L. N., Borovkov, J. E., Gokhberg, M. B., Krylov, S. M., and Troitskaya, V. A.: High resolution method of direct measurement of the magnetic field lines' eigen frequencies, Planetary and Space Science, 33, 1369–1374, doi: 10.1016/0032-0633(85)90112-6, 1985.

Bilitza, D. and Reinisch, B. W.: International Reference Ionosphere 2007: Improvements and new parameters, Advances in Space Research, 42, 599–609, doi: 10.1016/j.asr.2007.07.048, 2008.

Borisov, N. and Stubbe, P.: Excitation of longitudinal (field-aligned) currents by modulated HF heating of the ionosphere, Journal of Atmospheric and Terrestrial Physics, 59, 1973–1989, 1997.

Brekke, A.: Physics of the Upper Polar Atmosphere, John Wiley & Sons Ltd, 1997.

Chen, L. and Hasegawa, A.: A theory of long-period magnetic pulsations, 1. Steady state excitation of field line resonance, Journal of Geophysical Research, 79, 1024–1032, 1974.

Chi, P. J. and Russell, C. T.: Phase skipping and Poynting flux of continuous pulsations, Journal of Geophysical Research, 103, 29 479–29 492, doi:10.1029/98JA02101, 1998.

Chi, P. J., Russell, C. T., Raeder, J., Zesta, E., Yumoto, K., Kawano, H., Kitamura, K., Petrinec, S. M., Angelopoulos, V., Le, G., and Moldwin, M. B.: Propagation of the preliminary reverse impulse of sudden commencements to low latitudes, Journal of Geophysical Research, 106, 18 857–18 864, doi:10.1029/2001JA900071, 2001.

Chisham, G., Freeman, M. P., Abel, G. A., Lam, M. M., Pinnock, M., Coleman, I. J., Milan, S. E., Lester, M., Bristow, W. A., Greenwald, R. A., Sofko, G. J., and Villain, J.-P.: Remote sensing of the spatial and temporal structure of magnetopause and magnetotail reconnection from the ionosphere, Reviews of Geophysics, 46, 1004–+, doi:10.1029/2007RG000223, 2008.

Clausen, L. B. N., Yeoman, T. K., Behlke, R., and Lucek, E. A.: Multi-instrument observations of a large scale Pc4 pulsation, Annales Geophysicae, 26, 185–199, 2008.

Cowley, S. W. H.: Magnetosphere-Ionosphere Interactions: A Tutorial Review, pp. 91–106, Magnetospheric Current Systems, 2000.

Del Zanna, L. and Velli, M.: Coronal heating through Alfven waves, Advances in Space Research, 30, 471 – 480, doi:10.1016/S0273-1177(02)00320-4, URL http://www.sciencedirect.com/science/article/B6V3S-47248MG-16/2/3c4f6d834e06798795cde1575707b9f7, 2002.

Denton, R. E., Goldstein, J., Menietti, J. D., and Young, S. L.: Magnetospheric electron density model inferred from Polar plasma wave data, Journal of Geophysical Research, 107, 25–1, doi:10.1029/2001JA009136, 2002.

Dungey, J. W.: Interplanetary Magnetic Field and the Auroral Zones, Physical Review Letters, 6, 47–48, 1961.

Dunlop, M. W., Balogh, A., Glassmeier, K.-H., and Robert, P.: Four-point Cluster application of magnetic field analysis tools: The Curlometer, Journal of Geophysical Research, 107, 1384–1397, doi:10.1029/2001JA005088, 2002.

Dunlop, M. W., Lavraud, B., Cargill, P., Taylor, M. G. G. T., Balogh, A., Réme, H., Decreau, P., Glassmeier, K.-H., Elphic, R. C., Bosqued, J.-M., Fazakerley, A. N., Dandouras, I., Escoubet, C. P., Laakso, H., and Marchaudon, A.: Cluster Observations of the CUSP: Magnetic Structure and Dynamics, Surveys in Geophysics, 26, 5–55, doi:10.1007/s10712-005-1871-7, 2005.

Engebretson, M. J., Zanetti, L. J., Potemra, T. A., and Acuna, M. H.: Harmonically structured ULF pulsations observed by the AMPTE CCE magnetic field experiment, Geophysical Research Letters, 13, 905–908, 1986.

Engebretson, M. J., Hughes, W. J., Alford, J. L., Zesta, E., Cahill, L. J., Arnoldy, R. L., and Reeves, G. D.: Magnetometer array for cusp and cleft studies observations of the spatial extent of broadband ULF magnetic pulsations at cusp/cleft latitudes, Journal of Geophysical Research, 100, 19 371–19 386, doi:10.1029/95JA00768, 1995.

Escoubet, C. P., Fehringer, M., and Goldstein, M.: The Cluster Mission, Annales Geophysicae, 19, 1197–1200, 2001.

Fejer, J. A. and Krenzien, E.: Theory of generation of ULF pulsations by ionospheric modification experiments, Journal of Atmospheric and Terrestrial Physics, 44, 1075–1087, 1982.

Feldstein, Y. I. and Starkov, G. V.: Dynamics of auroral belt and polar geomagnetic disturbances, Planetary and Space Science, 15, 209–229, 1967.

Fenrich, F. R., Samson, J. C., Sofko, G., and Greenwald, R. A.: ULF high- and low-m field line resonances observed with the Super Dual Auroral Radar Network, Journal of Geophysical Research, 100, 21 535–21 548, doi:10.1029/95JA02024, 1995.

Giraud, A. and Petit, M.: Ionospheric techniques and phenomena, Reidel, D., Dordrecht, The Netherlands, 1978.

Glassmeier, K.-H., Motschmann, U., Dunlop, M., Balogh, A., Acuña, M. H., Carr, C., Musmann, G., Fornaçon, K.-H., Schweda, K., Vogt, J., Georgescu, E., and Buchert, S.: Cluster as a wave telescope - first results from the fluxgate magnetometer, Annales Geophysicae, 19, 1439–1447, 2001.

Gosling, J. T., Asbridge, J. R., Bame, S. J., Paschmann, G., and Sckopke, N.: Observations of two distinct populations of bow shock ions in the upstream solar wind, Geophysical Research Letters, 5, 957–960, doi:10.1029/GL005i011p00957, 1978.

Greenstadt, E. W.: Quasi-perpendicular/quasi-parallel divisions of earth's bow shock, Journal of Geophysical Research, 96, 1697–1703, doi:10.1029/90JA01759, 1991.

Greenstadt, E. W., McPherron, R. L., and Takahashi, K.: Solar wind control of daytime, midperiod geomagnetic pulsations, pp. 89–110, ULF pulsations in the magnetosphere. (A82-37426 18-46) Tokyo, Center for Academic Publications Japan; Dordrecht, D. Reidel Publishing Co., 1981, p. 89-110., 1981.

Gustafsson, G., André, M., Carozzi, T., Eriksson, A. I., Fälthammar, C.-G., Grard, R., Holmgren, G., Holtet, J. A., Ivchenko, N., Karlsson, T., Khotyaintsev, Y., Klimov, S., Laakso, H., Lindqvist, P.-A., Lybekk, B., Marklund, G., Mozer, F., Mursula, K., Pedersen, A., Popielawska, B., Savin, S., Stasiewicz, K., Tanskanen, P., Vaivads, A., and Wahlund, J.-E.: First results of electric field and density observations by Cluster EFW based on initial months of operation, Annales Geophysicae, 19, 1219–1240, 2001.

Hathaway, D. H., Wilson, R. M., and Reichmann, E. J.: The shape of the sunspot cycle, Solar Physics, 151, 177–190, doi:10.1007/BF00654090, 1994.

Hedin, A. E.: Extension of the MSIS thermosphere model into the middle and lower atmosphere, Journal of Geophysical Research, 96, 1159–1172, doi:10.1029/90JA02125, 1991.

Higuchi, T., Kokubun, S., and Ohtani, S.: Harmonic structure of compressional Pc5 pulsations at synchronous orbit, Geophysical Research Letters, 13, 1101–1104, 1986.

Holzworth, R. H. and Meng, C.-I.: Mathematical representation of the auroral oval, Geophysical Research Letters, 2, 377–380, 1975.

Hoppe, M. M., Russell, C. T., Frank, L. A., Eastman, T. E., and Greenstadt, E. W.: Upstream hydromagnetic waves and their association with backstreaming ion populations - ISEE 1 and 2 observations, Journal of Geophysical Research, 86, 4471–4492, doi:10.1029/JA086iA06p04471, 1981.

Hubert, D.: Nature and origin of wave modes in the dayside earth magnetosheath, Advances in Space Research, 14, 55–64, doi:10.1016/0273-1177(94)90048-5, 1994.

Jacobs, J. A., Kato, Y., Matsushita, S., and Troitskaya, V. A.: Classification of Geomagnetic Micropulsations, Journal of Geophysical Research, 69, 180–+, doi:10.1029/JZ069i001p00180, 1964.

Khan, H. and Cowley, S. W. H.: Observations of the response time of high-latitude ionospheric convection to variations in the interplanetary magnetic field using EISCAT and IMP-8 data, Annales Geophysicae, 17, 1306–1335, 1999.

Kivelson, M. G., Cao, M., McPherron, R. L., and Walker, R. J.: A Possible Signature of Magnetic Cavity Mode Oscillations in ISEE Spacecraft Observations, Journal of Geomagnetism and Geoelectricity, 49, 1079–1098, 1997.

Kokubun, S., Yamamoto, T., Acuna, M. H., Hayashi, K., Shiokawa, K., and Kawano, H.: The Geotail Magnetic Field Experiment, J. Geomag. Geoelectr., 46, 7–21, 1994.

Kornienko, V. A., Blagoveshchenskaya, N. F., Borisova, T. D., Thid, B., and Brekke, A.: Modification of the local substorm ionospheric and field-aligned currents produced by Tromsö heating facility, International Journal of Geomagnetism and Aeronomy, 4, 37–46, 2003.

Krauss-Varban, D.: Bow Shock and Magnetosheath Simulations: Wave Transport and Kinetic Properties, in: Solar Wind Sources of Magnetospheric Ultra-Low-Frequency Waves, edited by Engebretson, M. J., Takahashi, K., and Scholer, M., pp. 121–134, 1994.

Kurchashov, I. P., Nikomarov, I. S., Pilipenko, V. A., and Best, A.: Field line resonance effects in local meridional structure of mid-latitude geomagnetic pulsations, Annales Geophysicae, 5, 147–154, 1987.

Larsen, B. A., Klumpar, D. M., and Gurgiolo, C.: Correlation between plasmapause position and solar wind parameters, Journal of Atmospheric and Terrestrial Physics, 69, 334–340, doi:10.1016/j.jastp.2006.06.017, 2007.

Le, G. and Russell, C. T.: A study of ULF wave foreshock morphology-I: ULF foreshock boundary, Planetary and Space Science, 40, 1203–1213, doi:10.1016/0032-0633(92)90077-2, 1992a.

Le, G. and Russell, C. T.: A study of ULF wave foreshock morphology-II: spatial variation of ULF waves, Planetary and Space Science, 40, 1215–1225, doi:10.1016/0032-0633(92)90078-3, 1992b.

Lean, J.: Variations in the sun's radiative output, Reviews of Geophysics, 29, 505–535, doi:10.1029/91RG01895, 1991.

Lee, D.-H. and Lysak, R. L.: Magnetospheric ULF wave coupling in the dipole model - The impulsive excitation, Journal of Geophysical Research, 94, 17 097–17 103, 1989.

Lee, D.-H. and Lysak, R. L.: Impulsive excitation of ULF waves in the three-dimensional dipole model - The initial results, Journal of Geophysical Research, 96, 3479–3486, 1991.

Lucek, E. A., Horbury, T. S., Dunlop, M. W., Cargill, P. J., Schwartz, S. J., Balogh, A., Brown, P., Carr, C., Fornacon, K.-H., and Georgescu, E.: Cluster magnetic field observations at a quasi-parallel bow shock, Annales Geophysicae, 20, 1699–1710, 2002.

Lühr, H.: The IMAGE Magnetometer Network, STEP International Newsletter, 4, 4–6, 1994.

Mann, I. R. and Wright, A. N.: Diagnosing the excitation mechanisms of Pc5 magnetospheric flank waveguide modes and FLRs, Geophysical Research Letters, 26, 2609–2612, doi:10.1029/1999GL900573, 1999.

Mann, I. R., Chisham, G., and Wanliss, J. A.: Frequency-doubled density perturbations driven by ULF pulsations, Journal of Geophysical Research, 104, 4559–4566, doi:10.1029/1998JA900136, 1999.

McComas, D. J., Bame, S. J., Barker, P., Feldman, W. C., Phillips, J. L., Riley, P., and Griffee, J. W.: Solar Wind Electron Proton Alpha Monitor (SWEPAM) for the Advanced Composition Explorer, Space Science Reviews, 86, 563–612, 1998.

Meltz, G., Holway, Jr., L. H., and Tomljanovich, N. M.: Ionospheric heating by powerful radio waves, Radio Science, 9, 1049–1063, 1974.

Menk, F. W., Mann, I. R., Smith, A. J., Waters, C. L., Clilverd, M. A., and Milling, D. K.: Monitoring the plasmapause using geomagnetic field line resonances, Journal of Geophysical Research, 109, 4216–+, doi:10.1029/2003JA010097, 2004.

Nishida, A.: The GEOTAIL mission, Geophysical Research Letters, 21, 2871–2873, doi:10.1029/94GL01223, 1994.

Odera, T. J.: Solar wind controlled pulsations: a review., Reviews of Geophysics, 24, 55–74, 1986.

Ogilvie, K. W. and Coplan, M. A.: Solar wind composition, Reviews of Geophysics Supplement, 33, 615–622, URL `http://www.agu.org/journals/rg/rg9504S/95RG00122/index.html`, 1995.

Parker, E. N.: Dynamics of the Interplanetary Gas and Magnetic Fields., Astrophysical Journal, 128, 664–+, doi:10.1086/146579, 1958.

Paschmann, G., Sckopke, N., Bame, S. J., Asbridge, J. R., Gosling, J. T., Russell, C. T., and Greenstadt, E. W.: Association of low-frequency waves with suprathermal ions in the upstream solar wind, Geophysical Research Letters, 6, 209–212, doi:10.1029/GL006i003p00209, 1979.

Peredo, M., Slavin, J. A., Mazur, E., and Curtis, S. A.: Three-dimensional position and shape of the bow shock and their variation with Alfvenic, sonic and magnetosonic Mach numbers and interplanetary magnetic field orientation, Journal of Geophysical Research, 100, 7907–7916, 1995.

Radoski, H. R.: Highly Asymmetric MHD Resonances: the Guided Poloidal Mode, Journal of Geophysical Research, 72, 4026–+, doi:10.1029/JZ072i015p04026, 1967.

Robinson, T. R., Strangeway, R., Wright, D. M., Davies, J. A., Horne, R. B., Yeoman, T. K., Stocker, A. J., Lester, M., Rietveld, M. T., Mann, I. R., Carlson, C. W., and McFadden, J. P.: FAST observations of ULF waves injected into

the magnetosphere by means of modulated RF heating of the auroral electrojet, Geophysical Research Letters, 27, 3165–3168, doi:10.1029/2000GL011882, 2000.

Robinson, T. R., Yeoman, T. K., Dhillon, R. S., Lester, M., Thomas, E. C., Thornhill, J. D., Wright, D. M., van Eyken, A. P., and McCrea, I. W.: First observations of SPEAR-induced artificial backscatter from CUTLASS and the EISCAT Svalbard radars, Annales Geophysicae, 24, 291–309, 2006.

Rostoker, G. and Sullivan, B. T.: Polarization characteristics of Pc5 magnetic pulsations in the dusk hemisphere, Planetary and Space Science, 35, 429–438, doi:10.1016/0032-0633(87)90099-7, 1987.

Samson, J. C. and Rostoker, G.: Latitude-dependent characteristics of high-latitude Pc 4 and Pc 5 micropulsations, Journal of Geophysical Research, 77, 6133–6144, 1972.

Schäfer, S., Glassmeier, K. H., Eriksson, P. T. I., Pierrard, V., Fornaçon, K. H., and Blomberg, L. G.: Spatial and temporal characteristics of poloidal waves in the terrestrial plasmasphere: a CLUSTER case study, Annales Geophysicae, 25, 1011–1024, 2007.

Schulz, M.: Eigenfrequencies of geomagnetic field lines and implications for plasma-density modeling, Journal of Geophysical Research, 101, 17 385–17 398, doi:10.1029/95JA03727, 1996.

Schunk, R. W. and Nagy, A. F.: Ionospheres: physics, plasma physics, and chemistry, Cambridge Atmospheric and Space Science Series, Cambrige University Press, 2000.

Scoffield, H. C., Yeoman, T. K., Robinson, T. R., Baddeley, L. J., Dhillon, R. S., Wright, D. M., Raita, T., and Turunen, T.: First results of artificial stimulation of the ionospheric Alfvén resonator at 78°N, Geophysical Research Letters, 33, L19 103, doi:10.1029/2006GL027384, 2006.

Sentman, D. D., Edmiston, J. P., and Frank, L. A.: Instabilities of low frequency, parallel propagating electromagnetic waves in the earth's foreshock region, Journal of Geophysical Research, 86, 7487–7497, 1981.

Shue, J.-H., Chao, J. K., Fu, H. C., Russell, C. T., Song, P., Khurana, K. K., and Singer, H. J.: A new functional form to study the solar wind control of the magnetopause size and shape, Journal of Geophysical Research, 102, 9497–9512, doi:10.1029/97JA00196, 1997.

Sinha, A. K. and Rajaram, R.: An analytic approach to toroidal eigen mode, Journal of Geophysical Research, 102, 17 649–17 657, doi:10.1029/97JA01039, 1997.

Smith, C. W., L'Heureux, J., Ness, N. F., Acuña, M. H., Burlaga, L. F., and Scheifele, J.: The ACE Magnetic Fields Experiment, Space Science Reviews, 86, 613–632, 1998.

Southwood, D. J.: Some features of field line resonances in the magnetosphere, Planetary and Space Science, 22, 483–491, 1974.

Stone, E. C., Frandsen, A. M., Mewaldt, R. A., Christian, E. R., Margolies, D., Ormes, J. F., and Snow, F.: The Advanced Composition Explorer, Space Science Reviews, 86, 1–22, doi:10.1023/A:1005082526237, 1998.

Streltsov, A. and Lotko, W.: Influence of the finite ionospheric conductivity on dispersive, nonradiative field line resonances, Annales Geophysicae, 15, 625–633, 1997.

Stubbe, P.: Review of ionospheric modification experiments at Tromsø, Journal of Atmospheric and Terrestrial Physics, 58, 349–368, 1996.

Stubbe, P. and Kopka, H.: Modulation of polar electrojet by powerful HF waves, Journal of Geophysical Research, 82, 2319–2325, 1977.

Stubbe, P. and Kopka, H.: Generation of Pc 5 pulsations by polar electrojet modulation - First experimental evidence, Journal of Geophysical Research, 86, 1606–1608, 1981.

Stubbe, P., Kopka, H., Rietveld, M. T., and Dowden, R. L.: ELF and VLF wave generation by modulated HF heating of the current carrying lower ionosphere, Journal of Atmospheric and Terrestrial Physics, 44, 1123–1131, 1982.

Takahashi, K. and McPherron, R. L.: Harmonic structure of Pc 3-4 pulsations, Journal of Geophysical Research, 87, 1504–1516, 1982.

Takahashi, K., McPherron, R. L., and Terasawa, T.: Dependence of the spectrum of Pc 3-4 pulsations on the interplanetary magnetic field, Journal of Geophysical Research, 89, 2770–2780, 1984.

Tamao, T.: The Structure of Three-dimensional Hydromagnetic Waves in a Uniform Cold Plasma, Journal of Geomagnetism and Geoelectricity, 16, 89–114, 1964.

Troitskaya, V. A., Plyasova-Bakunina, T. A., and Gul'elmi, A. V.: Relationship between Pc 2-4 pulsations and the interplanetary field, Dokl. Akad. Nauk. SSSR, 197, 1312, 1971.

Trotignon, J. G., Décréau, P. M. E., Rauch, J. L., Randriamboarison, O., Krasnoselskikh, V., Canu, P., Alleyne, H., Yearby, K., Le Guirriec, E., Séran, H. C.,

Sené, F. X., Martin, P., Lévêque, M., and Fergeau, P.: How to determine the thermal electron density and the magnetic field strength from the Cluster/Whisper observations around the Earth, Annales Geophysicae, 19, 1711–1720, 2001.

Tsurutani, B. T. and Stone, R. G.: Collisionless shocks in the heliosphere: Reviews of current research, vol. 35, American Geophysical Union, 1985.

Tsyganenko, N. A.: Modeling the Earth's magnetospheric magnetic field confined within a realistic magnetopause, Journal of Geophysical Research, 100, 5599–5612, 1995.

Walker, A. D. M., Greenwald, R. A., Stuart, W. F., and Green, C. A.: STARE auroral radar observations of Pc 5 geomagnetic pulsations, Journal of Geophysical Research, 84, 3373–3388, 1979.

Waters, C. L., Menk, F. W., and Fraser, B. J.: The resonance structure of low latitude Pc3 geomagnetic pulsations, Geophysical Research Letters, 18, 2293–2296, 1991.

Waters, C. L., Samson, J. C., and Donovan, E. F.: The temporal variation of the frequency of high latitude field line resonances, Journal of Geophysical Research, 100, 7987–7996, 1995.

Watts, J. M. and Davies, K.: Rapid Frequency Analysis of Fading Radio Signals, Journal of Geophysical Research, 65, 2295–+, doi:10.1029/JZ065i008p02295, 1960.

Webb, D. and Orr, D.: Geomagnetic pulsations (5-50 mHz) and the interplanetary magnetic field, Journal of Geophysical Research, 81, 5941–5947, 1976.

Wright, D. M.: HF Doppler Observations of ULF Waves: System Development & High Latitude Results, Ph.D. thesis, University of Leicester, 1996.

Wright, D. M., Davies, J. A., Robinson, T. R., Chapman, P. J., Yeoman, T. K., Thomas, E. C., Lester, M., Cowley, S. W. H., Stocker, A. J., Horne, R. B., and Honary, F.: Space Plasma Exploration by Active Radar (SPEAR): an overview of a future radar facility, Annales Geophysicae, 18, 1248–1255, 2000.

Yordanova, E., Vaivads, A., André, M., Buchert, S. C., and Vörös, Z.: Magnetosheath Plasma Turbulence and Its Spatiotemporal Evolution as Observed by the Cluster Spacecraft, Physical Review Letters, 100, 205 003–+, doi:10.1103/PhysRevLett.100.205003, 2008.